



|                  |  |
|------------------|--|
| Title            | Preparation of Nitrogen-doped Hierarchically Porous Carbon for Electrochemical Energy Storage and Conversion |
| Author(s)        | 金, 清   |
| Citation         | 北海道大学. 博士(工学) 甲第13811号   |
| Issue Date       | 2019-09-25   |
| DOI              | 10.14943/doctoral.k13811   |
| Doc URL          | <a href="http://hdl.handle.net/2115/75879">http://hdl.handle.net/2115/75879</a>                              |
| Type             | theses (doctoral)  |
| File Information | Cheong_Kim.pdf   |



[Instructions for use](#)

**Preparation of Nitrogen-doped Hierarchically  
Porous Carbon for Electrochemical Energy  
Storage and Conversion**

**Cheong KIM**

**Graduate School of Chemical Sciences and Engineering  
Hokkaido University**

**2019**



# Contents

## Chapter 1

### General Introduction

|  |    |
|--|----|
| 1-1. Introduction .....  | 1  |
| 1-2. The use of porous carbon in electrochemical energy conversion/storage devices ..... | 2  |
| 1-3. How to prepare the high-performance carbon materials? .....                         | 7  |
| 1-4. Approaches and objectives of this thesis .....                                      | 11 |
| 1-5. References .....  | 13 |

## Chapter 2

### Preparation of the nitrogen-doped hierarchically porous carbons (NHPCs) by exothermic pyrolysis of biomass-cellulose

|   |    |
|---|----|
| 2-1. Introduction.....  | 17 |
| 2-2. Experimental.....  | 18 |
| 2-2-1. Synthesis of the NHPCs   |    |
| 2-2-2. Material characterizations   |    |
| 2-3. Results and discussion.....  | 20 |
| 2-3-1. Observation of the precursor   |    |
| 2-3-2. Exothermic pre-pyrolysis   |    |
| 2-3-3. Structure characterization of MgO@C precursors & the NHPCs by XRD patterns                               |    |
| 2-3-4. Morphology characterization of MgO@C precursors & the NHPCs by SEM and TEM                               |    |
| 2-3-5. Pore structure characterization of MgO@C composites by N <sub>2</sub> adsorption/desorption measurements |    |

|   |    |
|---|----|
| 2-3-6. Pore structure characterization of the NHPCs by N <sub>2</sub> adsorption/<br>desorption measurement |    |
| 2-3-7. TG air combustion analysis to determine the yield  |    |
| 2-3-8. XPS analysis   |    |
| 2-4. Conclusion.....  | 38 |
| 2-5. References .....   | 39 |

## **Chapter 3**

### **Oxygen reduction reaction (ORR) properties of the NHPCs**

|  |    |
|--|----|
| 3-1. Introduction.....   | 40 |
| 3-2. Experimental.....   | 40 |
| 3-2-1. ORR electrochemical measurements  |    |
| 3-2-2. Zn-air battery test   |    |
| 3-3. Results and discussion.....   | 43 |
| 3-3-1. CV measurements   |    |
| 3-3-2. ORR activity measurement by RDE at various rotating speeds and K-L<br>plots                     |    |
| 3-3-3. ORR activity comparison   |    |
| 3-3-4. Chronoamperometric measurement  |    |
| 3-3-5. Summary about the influence of the four preparation parameters to<br>electrochemical properties |    |
| 3-3-6. Zn-air battery test   |    |
| 3-4. Conclusions.....  | 53 |
| 3-5. References .....  | 54 |

## Chapter 4

### Preparation of the NHPCs with a tunable pore structure and high specific surface area

|   |    |
|---|----|
| 4-1. Introduction.....  | 55 |
| 4-2. Experimental.....  | 55 |
| 4-2-1. General synthesis process of the NHPCs with a tunable pore structure                                   |    |
| 4-2-2. Preparation of the NHPCs with a tunable pore structure   |    |
| 4-2-3. Material characterizations   |    |
| 4-3. Results and discussion.....  | 58 |
| 4-3-1. TG-DTA analysis for pyrolysis behavior of the precursors   |    |
| 4-3-2. Structure characterization of the precursors & the NHPCs with a tunable pore structure by XRD patterns |    |
| 4-3-3. Morphological characterization   |    |
| 4-3-4. Characterization by N <sub>2</sub> adsorption/desorption measurements                                  |    |
| 4-3-5. Discussion on the pore formation mechanism   |    |
| 4-3-6. XPS analysis   |    |
| 4-4. Conclusions.....   | 72 |
| 4-5. References.....  | 73 |

## Chapter 5

### Supercapacitor properties of the NHPCs with a tunable pore structure

|   |    |
|---|----|
| 5-1. Introduction.....                        | 74 |
| 5-2. Experimental.....                        | 74 |
| 5-2-1. Electrochemical measurements           |    |
| 5-3. Results and discussion.....              | 76 |
| 5-3-1. CV measurement by two-electrode system |    |

|  |    |
|--|----|
| 5-3-2. Galvanostatic charge and discharge curves by two-electrode system                                   |    |
| 5-3-3. Specific capacitance at various current density and long cycle stability<br>by two-electrode system |    |
| 5-3-4. Three-electrode system test   |    |
| 5-3-5. EIS measurements by three-electrode system  |    |
| 5-3-6. Ragone plots  |    |
| 5-4. Conclusion.....   | 87 |
| 5-5. References .....  | 88 |

## **Chapter 6**

|                                 |    |
|---------------------------------|----|
| <b>General Conclusion</b> ..... | 91 |
|---------------------------------|----|

## **List of Publications**

## **Acknowledgment**



# Chapter 1.

## General introduction

### 1-1. Introduction

Recently, the development of eco-friendly energy conversion and storage devices has attracted much attention, due to the gradual change in the climate, the increase in pollution of the world and the decreasing availability of fossil fuels. The electrochemical energy conversion and storage devices, such as metal-air batteries, fuel cells, supercapacitors, and other related batteries, have been considered to improve the energy conversion efficiency from fossil fuels or for the efficient use of sustainable energies such as solar and wind energy due to their high energy density, high power density, chemical stability, eco-friendly and low cost. The materials, which are used as the electrodes or catalysts of energy conversion and storage devices, are the most important components to obtain the superior electrochemical performance.<sup>1,2</sup>

Among the electrode materials, carbon materials have been used in various applications in batteries, fuel cell, and supercapacitors mainly based on their many advantages, such as their excellent electrical conductivity, adjustable porosity, many varieties of forms, and ease of processability.<sup>3,4</sup> For examples, carbon materials are used as electrocatalysts in metal-air batteries/fuel cells and active electrode materials in electric double layer capacitors (EDLCs). Therefore, the performance of these energy conversion and storage devices can be improved by exploring new and modified carbon materials.

**Figure 1-1** shows the various applications of the carbon materials. Various carbon materials, including carbon nanotubes, graphene, graphite, porous amorphous carbon, and their hybrids have been used in various applications, not only energy conversion and storage devices but also biotechnology, electronics, and nanotechnology for supporting our modern industries and life.<sup>5</sup> Porous carbon materials with high specific surface areas have been especially widely used in many electrochemical devices. In this thesis, the author will focus on the development and application of porous carbon materials for electrocatalysts and EDLC.

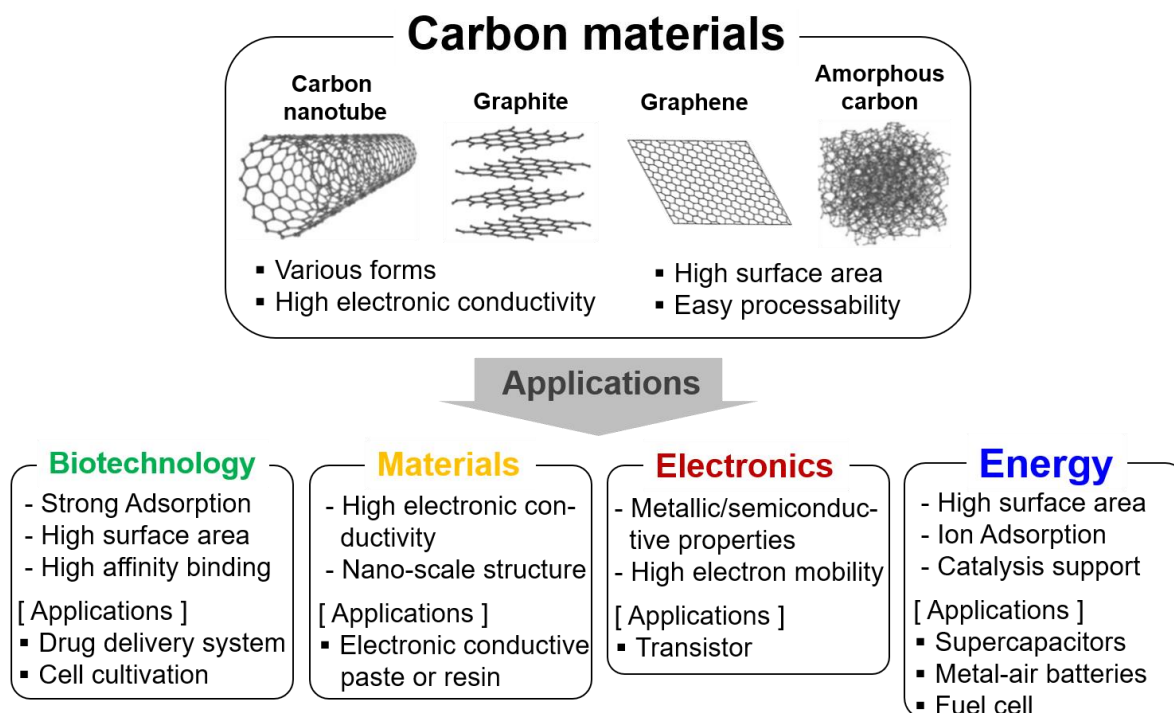


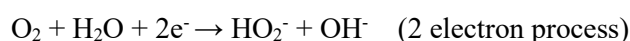
**Figure 1-1. Various application of the carbon materials.**

## 1-2. The use of porous carbon in electrochemical energy conversion/storage devices

### 1-2-1. Metal-air batteries

Metal-air batteries are considered as the most promising candidate for the next-generation energy storage system due to their high energy density and power density. **Figure 1-2** illustrates the schematic diagram of the basic structure of a metal-air battery.<sup>1,9</sup> Metal-air batteries consist of a metal (magnesium, lithium, aluminum, and zinc, etc.) electrode as the negative electrode, an air electrode as the positive electrode, a separator (only allow the transportation of ions), and electrolyte.

In the discharge process of metal air batteries, oxygen reduction reaction (ORR) is occurred in the air electrode as shown in below by the equations.<sup>2</sup>



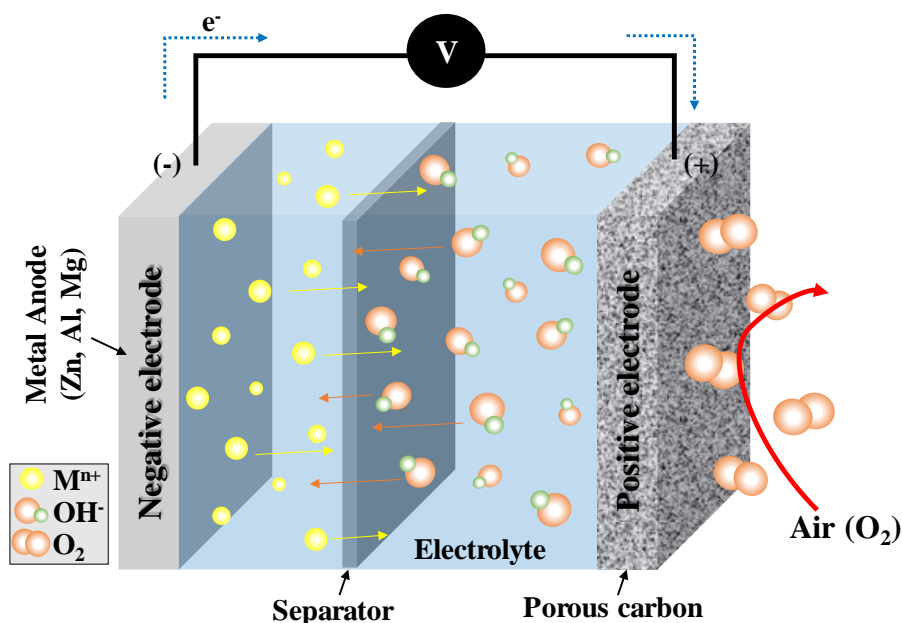


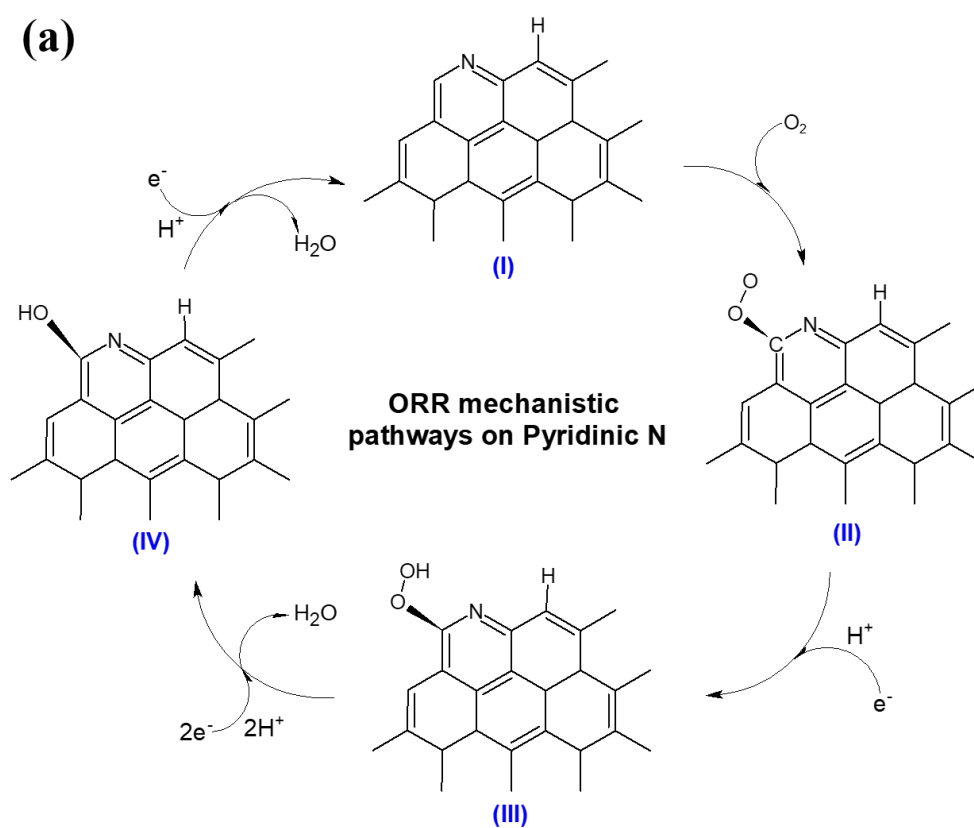
**Figure 1-2. Schematic diagram of the basic structure of a primary metal-air battery.**

In a metal-air battery system, the important issue to achieve high electrochemical performance is the low oxygen reduction kinetics for electrical energy production. Due to the sluggish nature of oxygen reduction reaction (ORR), catalyst materials are inevitably employed in air cathode. Platinum (Pt) and other precious metal-based compounds are the most effective for the ORR catalysts. However, the scarcity and high cost have hampered their widespread commercialization. Therefore, it is necessary to explore alternative materials that are inexpensive and have high electrocatalytic activity and long-term stability. So far, much effort has been made to explore inexpensive precious-metal-free catalysts, such as oxides and heteroatom-doped carbonaceous nanomaterials.<sup>7, 10, 11</sup>

Recent studies have indicated that nitrogen-doped porous carbon materials are the most promising candidate as metal-free electrocatalysts for ORR owing to their low-cost and desirable catalytic activity. The N-doping strategy is effective because of the unique electronic and structural properties. Charge delocalization in the  $sp^2$ -hybridized carbon frameworks may be induced due to the doping of electronegative N atoms, which can promote the adsorption of the oxygen ( $O_2$ ) molecule and enrich the densities of free charge carriers that act as active sites for the ORR.<sup>12-15</sup>

**Figure 1-3** shows the schematic diagram for the oxygen reduction reaction on nitrogen-doped carbon materials. **Figure 1-3 (a)** shows the ORR mechanism pathways on pyridinic N, suggesting from D. Guo et al.<sup>7</sup> According to D. Guo et. al., the Lewis base site is created by pyridinic N. The oxygen molecule is first adsorbed at the carbon atom next to the pyridinic N followed by protonation of the

adsorbed  $O_2$ . The other two protons attach to the two oxygen atoms, leading to breakage of the O-OH bond and formation of OH species. The additional proton then reacts with the absorbed OH to form  $H_2O$ . **Figure 1-3 (b)** shows the ORR mechanism pathways on graphitic N, suggesting from L. Huo et al.<sup>16</sup> According to L. Huo et al., on graphitic N active sites, the  $O_2$  molecules are firstly absorbed on adjacent C, and form a C-O-O intermediate. Then, the  $O_2$  is step-by-step reduced through the four-electron transfer pathway. In the process of the reaction, the graphitic N atoms are converted into pyridinic-like N atoms in a subsequent coupled electron-proton transfer step through the breaking of a C-N bond.



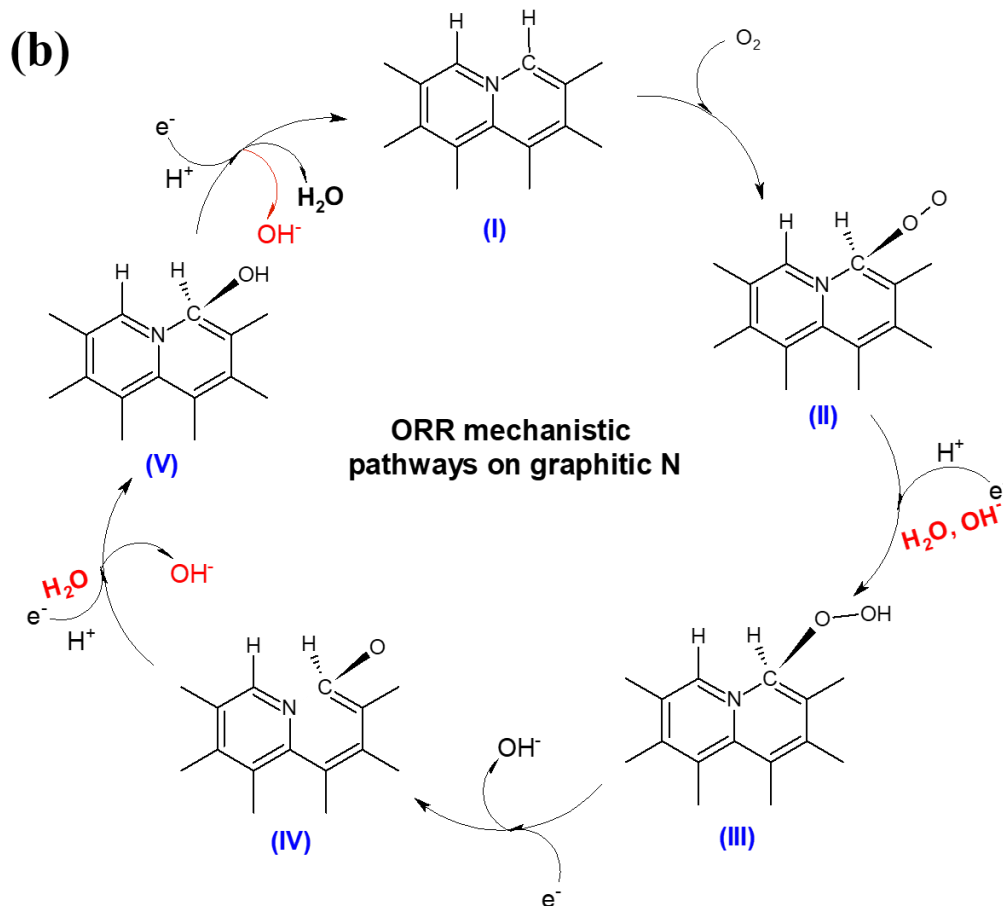


**Figure 1-3. Schematic diagram for oxygen reduction reaction on nitrogen-doped carbon materials. ORR mechanistic pathways on (a) pyridinic N; and (b) graphitic N.<sup>7, 16</sup>**

In addition, the ORR performance of carbon materials is also influenced by factors such as the specific surface area and porosity. Those factors can strongly impact the number of accessible active catalytic sites and efficient mass transfer. Generally, a 3D hierarchically porous carbon, which has a large specific surface area and an open multiporous structure (containing micro/meso/macropores), is considered to be efficient. These characteristics can enhance the mass transport of ORR-relevant species ( $\text{H}^+$ ,  $\text{O}_2$ ,  $\text{H}_2\text{O}$ ,  $\text{OH}^-$ , etc.) and improve their easy accessibility to the active sites.<sup>17-20</sup> A large number of micro/mesopores and the high specific surface area can increase the number of active sites. In addition, the macropore promotes the mass transport of ORR-relevant species to the active sites.

### 1-2-2. Electrical double-layer capacitors (EDLCs)

Supercapacitors (SCs), also known as electrical double layer capacitors (EDLCs), are considered as one of the most promising high-power electrochemical energy devices due to their long cycling

stability, high power density, rapid charging/discharging rates, and environmental friendliness.

**Figure 1-4** illustrates the basic structure of the EDLCs.<sup>1</sup> The EDLCs consists of positive and negative electrodes, which are separated by the separator in an electrolyte solution. The separator is generally ion-permeable, but also electrically insulating, soaked with electrolytes to allow ionic charge transfer between the electrodes. The electrostatic charge storage of the EDLCs occurs at electrolyte-electrode interfaces. The EDLCs generates electrical energy by physical absorption-desorption of ions during charge-discharge.

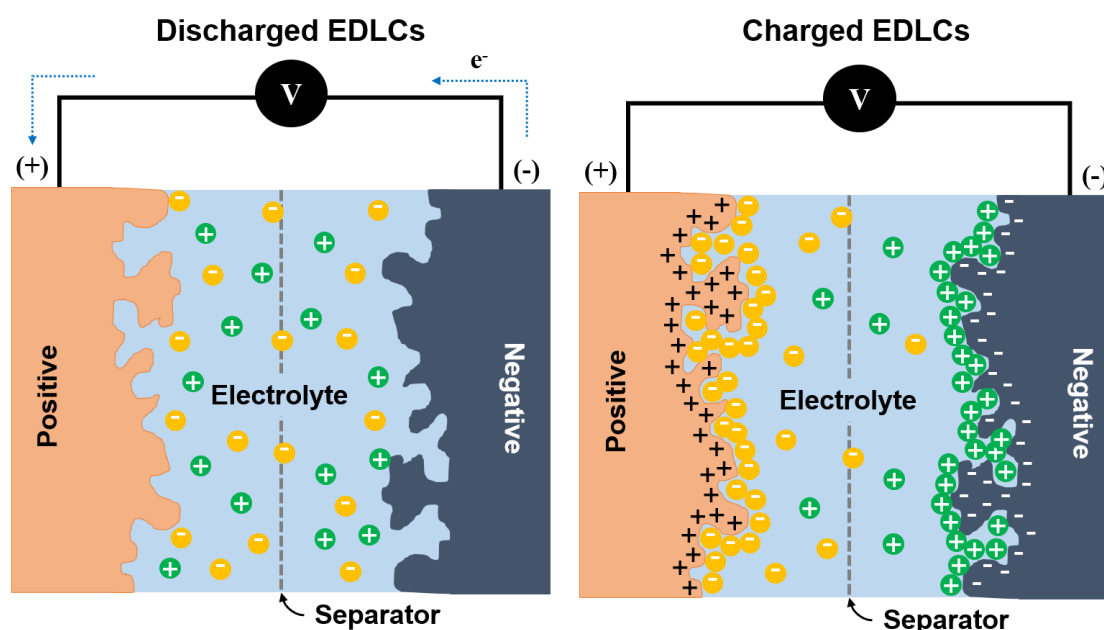


**Figure 1-4.** Schematic diagram of the basic structure of the EDLCs.

Currently, carbon nanomaterials are the most promising electrode materials for SCs owing to their high specific surface area and structural diversity.<sup>21, 22</sup> So far, many researchers have devoted their efforts to synthesizing diverse novel carbon nanostructures for SCs applications, for example, carbon nanotubes,<sup>23-25</sup> graphene and their derivatives,<sup>26, 27</sup> porous activated carbons.<sup>28-32</sup> To date, the porous activated carbons have been commercially used in SCs due to their advantages such as high specific surface area, the relatively facile production and low cost.

The performance of carbon nanomaterials as SCs electrodes can be enhanced by several strategies, for example, by increasing the number of active charge sites with enlarged surface area and porosity, and by adding active heteroatoms such as N and S. The first strategy contributes to the enhancement of the electrical double-layer capacitance, while the doping of heteroatoms introduces the additional

pseudo-capacitance.<sup>32-34</sup> It is normally recognized that the electrochemical capacitive reactions proceed at the electrode and electrolyte interfaces.

A hierarchical pore structure containing a multi-porous architecture of interconnected micro (< 2 nm), meso (2 nm ~50 nm), and macropores (> 50 nm) are considered to enhance the capacitive performance, especially the rate capability. The abundant micro- and mesopores offer abundant active sites and large accessible surface areas for the charge accommodation, while the interconnected meso- and macropores can facilitate the fast ion transport by supplying electrolyte-buffering reservoirs and shortened ion-transport pathways.<sup>35-40</sup>

### **1-3. How to prepare the high-performance carbon materials?**

#### **1-3-1. Commercial carbon materials**

Carbon materials, such as CNTs, graphene, graphite and amorphous carbon with various structure have been activated using various methods, such as chemical activation and template method for creating the additional pores and enlarging the specific surface area and pore volume.<sup>6, 8, 11, 14, 17, 21</sup> Moreover, heteroatom doping such as nitrogen, oxygen, and sulfur in carbon structure have been interested in enhancement of electrochemical properties for energy conversion and storage devices. The following shows the activation and heteroatom doping methods of commercial carbon materials;

##### (1) Chemical activation

Chemical activation has been widely used for various carbon materials to greatly improve the electrochemical performances of carbon materials. Among the chemical activation process, KOH activation process has been used to introduce the additional micro-pores and small mesopores into the carbon frame-structure under the maintenance of the intrinsic structure and properties of the original carbon materials, thus significantly enhancing the specific surface area and pore volume.<sup>41</sup> Generally, the KOH activation mechanism with carbon materials is suggested that the hydroxide reduction leads to H<sub>2</sub> and K metals, and carbon is oxidized to carbonates according to the general reaction as shown in the equation below.<sup>42</sup>



##### (2) Template method

Many kinds of inorganic templates, such as metal, silica, and zeolite, have been adopted to

synthesize porous carbon materials with uniform pore sizes. The general template synthetic procedure for porous carbon materials is as follows;<sup>6</sup> (i) preparation of the carbon precursor/inorganic template composite, (ii) carbonization, (iii) removal of the inorganic template. **Table 1-1** shows the specific surface area of porous carbon materials obtained by chemical and template activation method.

**Table 1-1. Specific surface area of porous carbon materials obtained by chemical and template activation method.**

| Starting materials                       | Activation method                               | SSA <sub>BET</sub> (m <sup>2</sup> g <sup>-1</sup> ) | Ref. |
|--|---|--|------|
| CNFs                                     | KOH activation                                  | 143  | 41   |
| CNTs                                     | KOH activation                                  | 1670   | 42   |
|  | NaOH activation                                 | 562  |      |
| CNTs                                     | KOH activation                                  | 644  | 43   |
| Graphene                                 | KOH activation                                  | 3100   | 44   |
| Poly(acrylic acid)                       | KOH activation                                  | 2674   | 45   |
| Lignosulfonate                           | KOH activation                                  | 1867   | 46   |
| CNFs                                     | KOH activation                                  | 212  | 47   |
| Ethylenediamine and carbon tetrachloride | KOH activation                                  | 1463   | 48   |
| Polysiloxane                             | NaOH activation + Silica domains template       | 2896   | 49   |
| Acrylonitrile and propylene              | Zeolite template                                | 1680   | 50   |
| Phenolic resin                           | Silicate oligomer template                      | 1760   | 51   |
| Acetylene                                | Iron template                                   | 880  | 52   |
| Glucose                                  | Continuous filament glass fiber arrays template | 1880   | 53   |

### (3) Nitrogen-doped porous carbon

Nitrogen-doped porous carbon materials have been interested in an effective method to modify carbon materials, such as graphene, carbon nanotube, activated carbon, and porous carbon because they can change the electronic properties or the surface chemistry of carbon materials. Recent studies have indicated that nitrogen doping can effectively enhance the surface activity and electrochemical performance of carbon materials because nitrogen-doped carbon has electron donor tendency and the conjugation between the  $\pi$ -system and the nitrogen lone-pair electrons of the carbon framework.<sup>54, 55</sup> These properties can enhance the electrochemical properties of carbon materials.

Nitrogen-doped porous carbons with good electrochemical properties have been obtained by thermal annealing of carbon materials with ammonia ( $\text{NH}_3$ ) and the direct pyrolysis and calcination of N-containing precursors such as melamine, dopamine, porphyrin, cyanamide, and aniline. **Table 1-2** shows the nitrogen-doped porous carbon materials with various synthesis methods and nitrogen sources.

**Table 1-2. Nitrogen-doped porous carbon materials**

| Carbon source                         | Synthesis method   | Nitrogen source          | SSA <sub>BET</sub> (m <sup>2</sup> g <sup>-1</sup> ) | Ref. |
|---------------------------------------|--|--------------------------|--|------|
| Coal tar pitch                        | FeCl <sub>3</sub> activation                                       | N <sub>2</sub> treatment | 1985   | 14   |
| Poly(acrylic acid)                    | KOH activation   | Melamine                 | 2674   | 45   |
| CNFs                                  | decomposition of<br>C <sub>2</sub> H <sub>4</sub> /NH <sub>3</sub> | Ammonia                  | 290  | 55   |
| Ethylene diamine<br>tetra acetic acid | Direct pyrolysis   | Melamine                 | 308.5  | 56   |
| Gelatin                               | NaOH activation  | Gelatin                  | 3012   | 57   |
| Resorcinol                            | NH <sub>3</sub> activation   | Ammonium<br>carbonate    | 2600   | 58   |

### 1-3-2. Biomass carbon

The requirement for the depletion of fossil-based carbon materials resources for producing porous carbon has motivated researchers to use sustainable biomass which are abundant, renewable and non-expensive raw materials for carbon. Biomass, as a renewable source, has received tremendous attention in the preparation of carbon materials because of its low cost, abundance, and environmental

friendliness. **Table 1-3** shows the synthesis methods and specific surface areas of the active carbon materials obtained by biomass precursor. Carbon materials using biomass has been synthesized by direct pyrolysis, hydrothermal carbonization followed by chemical activation (by KOH, NaOH, ZnCl<sub>2</sub>, etc.), physical activation (treated with O<sub>2</sub>, CO<sub>2</sub>, or steam), and a combination of the physical and chemical activation processes.

**Table 1-3. Synthesis methods and properties of biomass precursors.**

| Starting materials<br>(Biomass precursor)  | Synthesis method  | SSA <sub>BET</sub> (m <sup>2</sup> g <sup>-1</sup> ) | Reference |
|--|---|--|-----------|
| Pomelo peel                                | KOH activation  | 2725   | 59        |
| Lotus seedpod                              | KOH activation  | 1813   | 60        |
| Tobacco rod                                | Hydrothermal carbonization &<br>KOH activation  | 2097   | 61        |
| Corn husk                                  | KOH activation  | 867  | 62        |
| Pumpkin                                    | KOH activation  | 2968   | 63        |
| Natural flake graphite                     | Hummer's method (addition of<br>KM <sub>n</sub> O <sub>4</sub> , NaNO <sub>3</sub> , H <sub>2</sub> SO <sub>4</sub> )<br>+ KOH activation | 2252   | 64        |
| Gelatin                                    | Boric acid template   | 416  | 65        |
| Biomass waste, batata<br>leaves and stalks | Thermal treatment<br>+ KOH activation   | 3115   | 66        |
| Bagasse                                    | Hydrothermal carbonization<br>+ KOH activation  | 2296   | 67        |
| Bamboo                                     | K <sub>2</sub> FeO <sub>4</sub> activation  | 1732   | 68        |
| Moringa oleifera stems                     | Direct pyrolysis  | 2250   | 69        |
| Disposable cashmere                        | Thermal treatment<br>+ KOH activation   | 1358   | 70        |

Although many biomass carbon materials have been developed using the above-mentioned methods, the facile and efficient synthesis of heteroatom-doped porous carbon materials with well-design pore structure is very challenging.

## 1-4. Approaches and objectives of this thesis

In this study, a facile and efficient strategy to prepare value-added nitrogen-doped hierarchically porous carbons (NHPCs) was introduced, which involves a redox combustion reaction of metal nitrate-carbohydrates using biomass cellulose as raw material. Biomass-derived porous carbons with very high specific surface area (SSA) and heteroatom-doping are important for obtaining high performance in electrochemical energy conversion and storage devices, such as metal-air batteries and supercapacitors. Among various biomass resources, cellulose is an important structural component of the primary cell wall of green plants such as cotton and wood and one of the most sustainable and abundant biomass materials in nature.

In this new process, the pyrolysis of cellulose is accelerated by an exothermic reaction of using magnesium nitrate-carbohydrates (urea and cellulose) which are absorbed in the cellulose fibers. The incorporation of magnesium nitrate-urea-cotton or magnesium/potassium nitrate-urea-cotton endows the doping with nitrogen, exfoliates the fibers to fine 3D porous powders, and creates a large number of pores at various scales simultaneously.

This thesis consists of 6 chapters and organized as follows.

In Chapter 1, the general introduction and purpose of this study are described.

In Chapter 2, preparation techniques and characterizations of the NHPCs using biomass cellulose as the raw material are described. The NHPCs were synthesized by magnesium nitrate-carbohydrates (urea and cellulose) that induced an exothermic reaction during heating in an inert atmosphere. This is a facile and efficient synthesis method of hierarchically porous carbon.

In Chapter 3, the influence of four preparation parameters on the electrochemical performance for ORR was comprehensively investigated including species of magnesium salt, carbonization temperature, urea amount, and magnesium salt amount by rotating disk electrode measurement in O<sub>2</sub>-saturated 0.1M KOH solution. Furthermore, to confirm the practical use of the NHPCs in a real battery, primary Zn-air batteries with the catalysts on carbon paper as the air cathode was constructed, which were investigated in 6 M KOH electrolyte with Zn foil anode.

In Chapter 4, preparation techniques and characterizations of the NHPCs with a tunable pore structure were explained. The NHPCs are also of great interest as electrode materials for supercapacitors because the NHPCs have high specific surface areas that contribute to the capacitance increase and the nitrogen doping is known to enhance further the capacitance. However, for the capacitor applications, the specific surface area of the NHPCs (synthesized in chapter 2) has still limited; The specific capacitance must be increased to  $> 2000 \text{ m}^2 \text{ g}^{-1}$  and tunable pore structure with micro-, meso- and macropores.

In Chapter 5, the applications of the NHPCs with a tunable pore structure for supercapacitors were investigated by two and three electrode system supercapacitors in 6M KOH solution.

Finally, all the results and achievements in this study are summarized in Chapter 6.

## 1-5. Reference

- [1] C. Zhong, Y. Deng, W. Hu, J. Qiao, L. Zhang, J. Zhang, A review of electrolyte materials and compositions for electrochemical supercapacitors, *Chem. Soc. Rev.* 44 (2015) 7484–7539.
- [2] Y. Li, H. Dai, Recent advances in Zinc-air batteries, *Chem. Soc. Rev.* 43 (2014) 5257–5275.
- [3] X. Chen, R. Paul, L. Dai, Carbon-based supercapacitors for efficient energy storage, *Natl. Sci. Rev.* 4 (2017) 453–489.
- [4] J. Wang, S. Kaskel, KOH activation of carbon-based materials for energy storage, *J. Mater. Chem.* 22 (2012) 23710–23725.
- [5] M. Inagaki, M. Toyoda, Y. Soneda, T. Morishita, Nitrogen-doped carbon materials, *Carbon* N. Y. 132 (2018) 104–140.
- [6] J. Lee, J. Kim, T. Hyeon, Recent progress in the synthesis of porous carbon materials, *Adv. Mater.* 18 (2006) 2073–2094.
- [7] D. Guo, R. Shibuya, C. Akiba, S. Saji, T. Kondo, J. Nakamura, Active sites of nitrogen-doped carbon materials for oxygen reduction reaction clarified using model catalysts, *Science* 351 (2016) 361–365.
- [8] M. Demir, S.K. Saraswat, R.B. Gupta, Hierarchical nitrogen-doped porous carbon derived from lecithin for high-performance supercapacitors, *RSC Adv.* 7 (2017) 42430–42442.
- [9] J.S. Lee, S.T. Kim, R. Cao, N.S. Choi, M. Liu, K.T. Lee, J. Cho, Metal-air batteries with high energy density: Li-air versus Zn-air, *Adv. Energy Mater.* 1 (2011) 34–50.
- [10] C. Hu, L. Dai, Multifunctional carbon-based metal-free electrocatalysts for Simultaneous oxygen reduction, oxygen evolution, and hydrogen evolution, *Adv. Mater.* 29 (2017) 1604942.
- [11] D.Y. Chung, K.J. Lee, S.H. Yu, M. Kim, S.Y. Lee, O.H. Kim, H.J. Park, Y.E. Sung, Alveoli-Inspired Facile Transport Structure of N-Doped Porous Carbon for Electrochemical Energy Applications, *Adv. Energy Mater.* 5 (2015) 1401309.
- [12] X. Wu, X. Yu, Z. Lin, J. Huang, L. Cao, B. Zhang, Y. Zhan, H. Meng, Y. Zhu, Y. Zhang, Nitrogen doped graphitic carbon ribbons from cellulose as non noble metal catalyst for oxygen reduction reaction, *Int. J. Hydrogen Energy* 41 (2016) 14111–14122.
- [13] H. Zhang, J. Chen, Y. Li, P. Liu, Y. Wang, T. An, H. Zhao, Nitrogen-Doped Carbon Nanodots@Nanospheres as An Efficient Electrocatalyst for Oxygen Reduction Reaction, *Electrochim. Acta* 165 (2015) 7–13.
- [14] D. Yu, L. Zhou, J. Tang, J. Li, J. Hu, C. Peng, H. Liu, Nitrogen-Doped Porous Carbon Nanosheets Derived from Coal Tar Pitch as an Efficient Oxygen-Reduction Catalyst, *Ind. Eng. Chem. Res.* 56 (2017) 8880–8887.
- [15] Q. Wang, Y. Lei, Z. Chen, N. Wu, Y. Wang, B. Wang, Y. Wang, Fe/Fe<sub>3</sub>C@C nanoparticles encapsulated in N-doped graphene–CNTs framework as an efficient bifunctional oxygen electrocatalyst for robust rechargeable Zn–air batteries, *J. Mater. Chem. A* 6 (2018) 516–526.
- [16] L. Huo, B. Liu, G. Zhang, R. Si, J. Liu, J. Zhang, 2D Layered non-precious metal mesoporous electrocatalysts for enhanced oxygen reduction reaction, *J. Mater. Chem. A* 5 (2017) 4868–4878.
- [17] K. Wan, A.D. Tan, Z.P. Yu, Z.X. Liang, J.H. Piao, P. Tsiakaras, 2D nitrogen-doped hierarchically porous carbon: Key role of low dimensional structure in favoring electrocatalysis and mass transfer for oxygen reduction reaction, *Appl. Catal. B* 209 (2017) 447–454.
- [18] H.T. Chung, D.A. Cullen, D. Higgins, B.T. Sneed, E.F. Holby, K.L. More, P. Zelenay, Direct atomic-level insight into the active sites of a high-performance PGM-free ORR catalyst, *Science* 257 (2017) 479–484.
- [19] Y. Wang, H. Liu, K. Wang, S. Song, P. Tsiakaras, 3D interconnected hierarchically porous N-doped carbon with NH<sub>3</sub> activation for efficient oxygen reduction reaction, *Appl. Catal. B* 210 (2017) 57–66.
- [20] H. Fan, W. Shen, Gelatin-Based Microporous Carbon Nanosheets as High Performance Supercapacitor Electrodes, *ACS*

Sustainable Chem. Eng. 4 (2016) 1328-1337.

[21] M.R. Benzigar, S.N. Talapaneni, S. Joseph, K. Ramadass, G. Singh, J. Scaranto, U. Ravon, K. Al-Bahily, A. Vinu, Recent advances in functionalized micro and mesoporous carbon materials: synthesis and applications, *Chem. Soc. Rev.* 47 (2018) 2680-2721.

[22] T.Y. Liu, F. Zhang, Y. Song, Y. Li, Revitalizing carbon supercapacitor electrodes with hierarchical porous structures, *J. Mater. Chem. A* 5 (2017) 17705-17733.

[23] D. Z. Chen, J. Yu, W. Lu, Y. Zhao, Y. Yan, T.-W. Chou, Temperature effects on electrochemical performance of carbon nanotube film based flexible all-solid-state supercapacitors, *Electrochim. Acta* 233 (2017) 181-189.

[24] Y. Zhang, T. Mao, H. Wu, L. Cheng, L. Zheng, Carbon Nanotubes Grown on Flax Fabric as Hierarchical All-Carbon Flexible Electrodes for Supercapacitors, *Adv. Mater. Interfaces* 4 (2017) 1601123.

[25] E.A. Nagelli, L. Huang, A.Q.Z. Dai, F. Du, L. Dai, 3D Vertically Aligned CNT/Graphene Hybrids from Layer-by-Layer Transfer for Supercapacitors, *Particle & Particle Systems Characterization* 34 (2017) 1700131.

[26] I.L. Tsai, J. Cao, L. Le Fevre, B. Wang, R. Todd, R.A.W. Dryfe, A.J. Forsyth, Graphene-enhanced electrodes for scalable supercapacitors, *Electrochim. Acta* 257 (2017) 372-379.

[27] J. Li, J. Tang, J. Yuan, K. Zhang, Y. Sun, H. Zhang, L.C. Qin, Enlarging energy density of supercapacitors using unequal graphene electrodes and ionic liquid electrolyte, *Electrochim. Acta* 258 (2017) 1053-1058.

[28] Y.Y. Smolin, K.L. Van Aken, M. Boota, M. Soroush, Y. Gogotsi, K.K.S. Lau, Engineering Ultrathin Polyaniline in Micro/Mesoporous Carbon Supercapacitor Electrodes Using Oxidative Chemical Vapor Deposition, *Adv. Mater. Interfaces* 4 (2017) 1601201.

[29] J.W. Jeon, J.H. Han, S.K. Kim, D.G. Kim, Y.S. Kim, D.H. Suh, Y.T. Hong, T.H. Kim, B.G. Kim, Intrinsically microporous polymer-based hierarchical nanostructuring of electrodes via nonsolvent-induced phase separation for high-performance supercapacitors, *J. Mater. Chem. A* 6 (2018) 8909-8915.

[30] Y. Wang, L. Jiang, Roles of Graphene Oxide in Hydrothermal Carbonization and Microwave Irradiation of Distiller's Dried Grains with Solubles To Produce Supercapacitor Electrodes, *ACS Sustainable Chemistry & Engineering* 5 (2017) 5588-5597.

[31] W. Gao, D. Chen, H. Quan, R. Zou, W. Wang, X. Luo, L. Guo, Fabrication of Hierarchical Porous Metal–Organic Framework Electrode for Aqueous Asymmetric Supercapacitor, *ACS Sustainable Chemistry & Engineering* 5 (2017) 4144-4153.

[32] L. Miao, H. Duan, M. Liu, W. Lu, D. Zhu, T. Chen, L. Li, L. Gan, Poly(ionic liquid)-derived, N, S-codoped ultramicroporous carbon nanoparticles for supercapacitors, *Chem. Eng. Journal* 317(2017) 651-659.

[33] A. Sanchez-Sanchez, M.T. Izquierdo, S. Mathieu, J. González-Álvarez, A. Celzard, V. Fierro, Outstanding electrochemical performance of highly N- and O-doped carbons derived from pine tannin, *Green Chem.* 19 (2017) 2653-2665.

[34] Z. Song, L. Li, D. Zhu, L. Miao, H. Duan, Z. Wang, W. Xiong, Y. Lv, M. Liu, L. Gan, Synergistic design of a N, O co-doped honeycomb carbon electrode and an ionogel electrolyte enabling all-solid-state supercapacitors with an ultrahigh energy density, *J. Mater. Chem. A*, 7 (2019) 816-826.

[35] J. Wang, J. Tang, B. Ding, V. Malgras, Z. Chang, X. Hao, Y. Wang, H. Dou, X. Zhang, Y. Yamauchi, Hierarchical porous carbons with layer-by-layer motif architectures from confined soft-template self-assembly in layered materials, *Nature Communications* 8 (2017) 15717.

[36] D. Jia, X. Yu, H. Tan, X. Li, F. Han, L. Li, H. Liu, Hierarchical porous carbon with ordered straight micro-channels templated by continuous filament glass fiber arrays for high performance supercapacitors, *J. Mater. Chem. A* 5 (2017) 1516-1525.

[37] Y. Cai, Y. Luo, H. Dong, X. Zhao, Y. Xiao, Y. Liang, H. Hu, Y. Liu, M. Zheng, Hierarchically porous carbon nanosheets derived from *Moringa oleifera* stems as electrode material for high-performance electric double-layer capacitors, *J. Power Sources* 353 (2017) 260-269.

[38] L.N. Han, X. Wei, Q.C. Zhu, S.-M. Xu, K.X. Wang, J.S. Chen, Nitrogen-doped carbon nets

- with micro/mesoporous structures as electrodes for high-performance supercapacitors, *J. Mater. Chem. A* 4 (2016) 16698-16705.
- [39] L. Zhou, H. Cao, S. Zhu, L. Hou, C. Yuan, Hierarchical micro-/mesoporous N- and O-enriched carbon derived from disposable cashmere: a competitive cost-effective material for high-performance electrochemical capacitors, *Green Chem.* 17 (2015) 2373-2382.
- [40] H. Su, H. Zhang, F. Liu, F. Chun, B. Zhang, X. Chu, H. Huang, W. Deng, B. Gu, H. Zhang, X. Zheng, M. Zhu, W. Yang, High power supercapacitors based on hierarchically porous sheet-like nanocarbons with ionic liquid electrolytes, *Chemical Engineering Journal* 322 (2017) 73-81.
- [41] S.H. Yoon, S. Lim, Y. Song, Y. Ota, W. Qiao, A. Tanaka, and I. Mochida, KOH activation of carbon nanofibers, *Carbon N. Y.* 42 (2004) 1723-1729
- [42] E. Raymundo-Piñero, P. Azaïs, T. Cacciaguerra, D. Cazorla-Amorós, A. Linares-Solano, F. Béguin, KOH and NaOH activation mechanisms of multiwalled carbon nanotubes with different structural organisation, *Carbon N. Y.* 43 (2005) 786-795.
- [43] B. Xu, F. Wu, Y. Su, G. Cao, S. Chen, Z. Zhou, Y. Yang, Competitive effect of KOH activation on the electrochemical performances of carbon nanotubes for EDLC: Balance between porosity and conductivity, *Electrochim. Acta.* 53 (2008) 7730-7735.
- [44] Y. Zhu, S. Murali, M.D. Stoller, K.J. Ganesh, W. Cai, P.J. Ferreira, A. Pirkle, R.M. Wallace, K.A. Cychosz, M. Thommes, D. Su, E.A. Stach, R.S. Ruoff, Carbon-based supercapacitors produced by activation of graphene, *Science* 332 (2011) 1537-1542.
- [45] J. Jiang, L. Bao, Y. Qiang, Y. Xiong, J. Chen, S. Guan, J. Chen, Sol-gel process-derived rich nitrogen-doped porous carbon through KOH activation for supercapacitors, *Electrochim. Acta.* 158 (2015) 229-236.
- [46] W. Zhang, C. Yu, L. Chang, W. Zhong, W. Yang, Three-dimensional nitrogen-doped hierarchical porous carbon derived from cross-linked lignin derivatives for high performance supercapacitors, *Electrochim. Acta.* 282 (2018) 642-652.
- [47] C. Merino, P. Soto, E. Vilaplana-Ortego, J.M. De Gomez Salazar, F. Pico, J.M. Rojo, Carbon nanofibres and activated carbon nanofibres as electrodes in supercapacitors, *Carbon N. Y.* 43 (2005) 551-557.
- [48] M. Zhou, F. Pu, Z. Wang, S. Guan, Nitrogen-doped porous carbons through KOH activation with superior performance in supercapacitors, *Carbon N. Y.* 68 (2014) 185-194.
- [49] J. Yang, J. Hu, M. Zhu, Y. Zhao, H. Chen, F. Pan, Ultrahigh surface area meso/microporous carbon formed with self-template for high-voltage aqueous supercapacitors, *J. Power Sources.* 365 (2017) 362-371.
- [50] C.O. Ania, V. Khomenko, E. Raymundo-Piñero, J.B. Parra, F. Béguin, The large electrochemical capacitance of microporous doped carbon obtained by using a zeolite template, *Adv. Funct. Mater.* 17 (2007) 1828-1836.
- [51] H. Chen, Q. Li, N. Teng, D. Long, C. Ma, Y. Wei, J. Wang, L. Ling, Simultaneous micropore development and nitrogen doping of ordered mesoporous carbons for enhanced supercapacitor and Li-S cathode performance, *Electrochim. Acta.* 214 (2016) 231-240.
- [52] Z.M. Sheng, J.N. Wang, J.C. Ye, Synthesis of nanoporous carbon with controlled pore size distribution and examination of its accessibility for electric double layer formation, *Microporous Mesoporous Mater.* 111 (2008) 307-313.
- [53] D. Jia, X. Yu, H. Tan, X. Li, F. Han, L. Li, H. Liu, Hierarchical porous carbon with ordered straight micro-channels templated by continuous filament glass fiber arrays for high performance supercapacitors, *J. Mater. Chem. A.* 5 (2017) 1516-1525.
- [54] P. Ayala, R. Arenal, M. Rummeli, A. Rubio, and T. Pichler, The doping of carbon nanotubes with nitrogen and their potential applications, *Carbon N. Y.* 49 (2010) 575-586.
- [55] Z. R. Ismagilov, A. E. Shalagina, O. Yu. Podyacheva, A. V. Ischenko, L. S. Kibis, A. I. Boronin, Y. A. Chesalov, D. I. Kochubey, A. I. Romanenko, Olga B. Anikeeva, T. I. Buryakov, and E. N. Tkachev, Structure and electrical conductivity of nitrogen-doped carbon nanofibers, *Carbon N. Y.* 47 (2009) 1922-1929.

- [56] W. Yang, W. Yang, L. Kong, A. Song, X. Qin, Facile synthesis of nitrogen-doped porous carbon for high-performance supercapacitors, *RSC Adv.* 7 (2017) 55257–55263.
- [57] B. Xu, S. Hou, G. Cao, F. Wu, Y. Yang, Sustainable nitrogen-doped porous carbon with high surface areas prepared from gelatin for supercapacitors, *J. Mater. Chem.* 22 (2012) 19088–19093.
- [58] Y. Wang, H. Liu, K. Wang, S. Song, P. Tsiakaras, 3D interconnected hierarchically porous N-doped carbon with NH<sub>3</sub> activation for efficient oxygen reduction reaction, *Appl. Catal. B Environ.* 210 (2017) 57–66.
- [59] Q. Liang, L. Ye, Z.H. Huang, Q. Xu, Y. Bai, F. Kang, Q.H. Yang, A honeycomb-like porous carbon derived from pomelo peel for use in high-performance supercapacitors, *Nanoscale.* 6 (2014) 13831–13837.
- [60] B. Liu, X. Zhou, H. Chen, Y. Liu, H. Li, Promising porous carbons derived from lotus seedpods with outstanding supercapacitance performance, *Electrochim. Acta.* 208 (2016) 55–63.
- [61] Y.Q. Zhao, M. Lu, P.Y. Tao, Y.J. Zhang, X.T. Gong, Z. Yang, G.Q. Zhang, H.L. Li, Hierarchically porous and heteroatom doped carbon derived from tobacco rods for supercapacitors, *J. Power Sources.* 307 (2016) 391–400.
- [62] S. Song, F. Ma, G. Wu, D. Ma, W. Geng, J. Wan, Facile self-templating large scale preparation of biomass-derived 3D hierarchical porous carbon for advanced supercapacitors, *J. Mater. Chem. A.* 3 (2015) 18154–18162.
- [63] S. Bai, G. Tan, X. Li, Q. Zhao, Y. Meng, Y. Wang, Y. Zhang, D. Xiao, Pumpkin-Derived Porous Carbon for Supercapacitors with High Performance, *Chem. An Asian J.* 11 (2016) 1828–1836.
- [64] H. Fan, W. Shen, Gelatin-Based Microporous Carbon Nanosheets as High Performance Supercapacitor Electrodes, *ACS Sustain. Chem. Eng.* 4 (2016) 1328–1337.
- [65] Z. Ling, Z. Wang, M. Zhang, C. Yu, G. Wang, Y. Dong, S. Liu, Y. Wang, J. Qiu, Sustainable Synthesis and Assembly of Biomass-Derived B/N Co-Doped Carbon Nanosheets with Ultrahigh Aspect Ratio for High-Performance Supercapacitors, *Adv. Funct. Mater.* 26 (2016) 111–119.
- [66] X. Wei, Y. Li, S. Gao, Biomass-derived interconnected carbon nanoring electrochemical capacitors with high performance in both strongly acidic and alkaline electrolytes, *J. Mater. Chem. A.* 5 (2017) 181–188.
- [67] H. Feng, H. Hu, H. Dong, Y. Xiao, Y. Cai, B. Lei, Y. Liu, M. Zheng, Hierarchical structured carbon derived from bagasse wastes: A simple and efficient synthesis route and its improved electrochemical properties for high-performance supercapacitors, *J. Power Sources.* 302 (2016) 164–173.
- [68] Y. Gong, D. Li, C. Luo, Q. Fu, C. Pan, Highly porous graphitic biomass carbon as advanced electrode materials for supercapacitors, *Green Chem.* 19 (2017) 4132–4140.
- [69] Y. Cai, Y. Luo, H. Dong, X. Zhao, Y. Xiao, Y. Liang, H. Hu, Y. Liu, M. Zheng, Hierarchically porous carbon nanosheets derived from *Moringa oleifera* stems as electrode material for high-performance electric double-layer capacitors, *J. Power Sources.* 353 (2017) 260–269.
- [70] L. Zhou, H. Cao, S. Zhu, L. Hou, C. Yuan, Hierarchical micro-/mesoporous N- and O-enriched carbon derived from disposable cashmere: A competitive cost-effective material for high-performance electrochemical capacitors, *Green Chem.* 17 (2015) 2373–2382.

## Chapter 2.

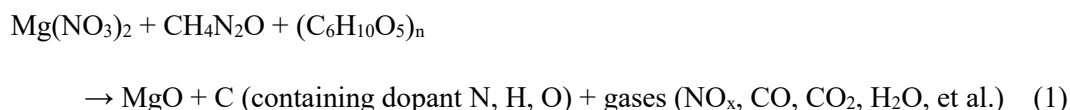
# Preparation of the nitrogen-doped hierarchically porous carbon by exothermic pyrolysis of biomass-cellulose

### 2-1. Introduction

In this chapter, the nitrogen-doped hierarchically porous carbons (NHPCs) for oxygen reduction reaction (ORR) electrocatalyst are prepared using biomass cellulose as the raw material. The pyrolysis of cellulose is accelerated by a redox combustion reaction of magnesium nitrate-carbohydrates (urea and cellulose), which endows the doping with nitrogen, exfoliates the cellulose to highly porous particles and creates numerous pores simultaneously. After being further carbonized at high temperature and washed with acid, the NHPCs are produced which have a hierarchical porous structure and large specific surface area. The influence of four preparation parameters, including species of magnesium salt, carbonization temperature, urea amount and magnesium salt amount, on the porous characteristics are comprehensively investigated.

**Figure 2-1** shows the schematic diagram for the preparation of the NHPCs from cotton cellulose raw material, which is innovated by an exothermic reaction-accelerated pyrolysis process to exfoliate the micron-sized bulky cellulose fibers to highly porous carbon. The raw materials of cotton fibers are firstly impregnated with magnesium nitrate-urea aqueous solution and subsequently dried. The dried fiber precursors are further heated to 500°C at 10 K min<sup>-1</sup> for their pre-pyrolysis, where the intensive exothermic reactions occur at around 200°C.

In general, the formation of MgO@C composite precursor by the exothermic pyrolysis of magnesium nitrate-urea-cellulose can be represented by the following reaction formula:



The pre-pyrolyzed precursors are further pulverized and heat-treated at high temperatures ranging from 700 to 1000 °C to increase the carbonization of the final products. Finally, after acid washing, the porous carbon products are obtained.

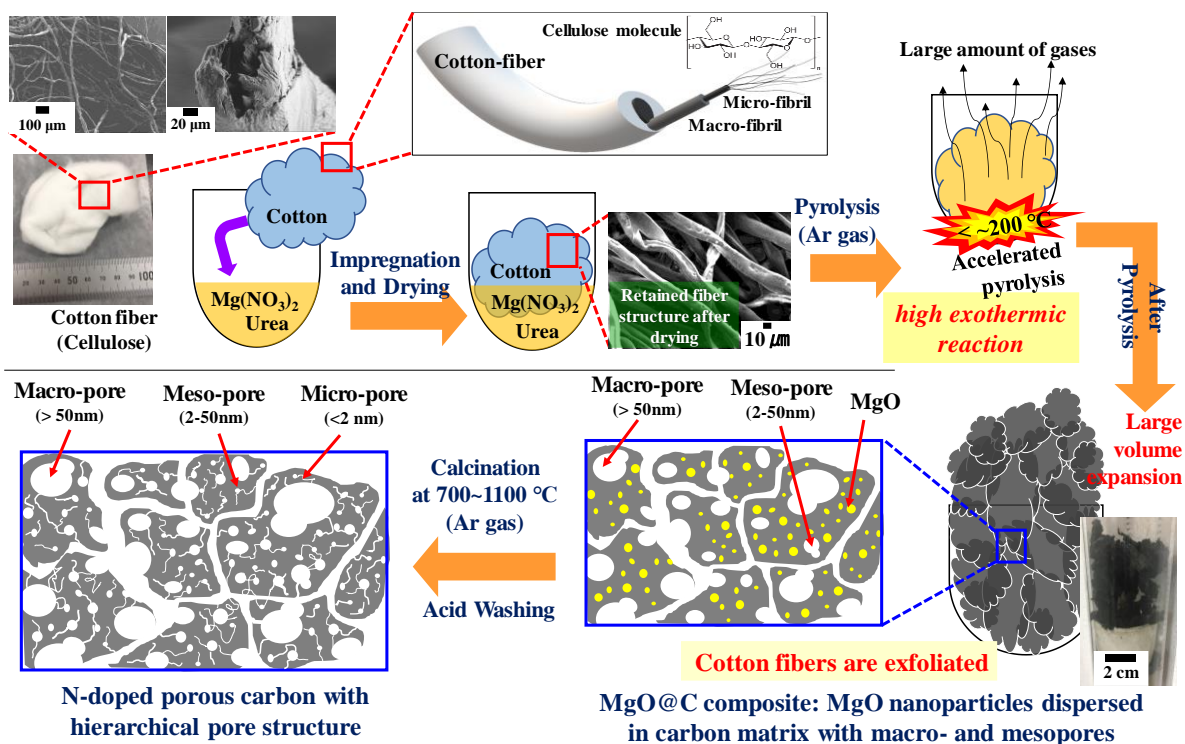


Figure 2-1. Schematic diagram for the preparation of the NHPCs.

## 2-2. Experimental

### 2-2-1. Synthesis of the NHPCs

Four experimental parameters are evaluated in detail for the preparation of the NHPCs. The parameters are (I) species of magnesium salts, (II) carbonization temperature, (III) ratio of urea to cellulose, and (IV) magnesium salt amount.

*I. Species of magnesium salts effect;* In this part, the NHPCs were prepared by different kind of magnesium salts. 10 mmol magnesium salt ( $\text{Mg}(\text{NO}_3)_2 \cdot 6\text{H}_2\text{O}$ , Kanto chemical Co., 99.0 % or  $\text{Mg}(\text{CH}_3\text{COO})_2 \cdot 4\text{H}_2\text{O}$ , Wako pure chemical Co., 99.9 %) and urea ( $\text{CO}(\text{NH}_2)_2$ , Kishida chemical Co., 99.0 %) with a molar ratio of 1 to 0 or 1 to 2 were dissolved in 5 mL ultrapure distilled water to form the homogeneous precursor, which was impregnated with 1 g cotton cellulose, which was obtained Suzuran sanitary goods corporation ( $(\text{C}_6\text{H}_{10}\text{O}_5)_n$ , 100 %). The wet cotton soaked with the homogenous precursor solutions was dried at  $60^\circ\text{C}$  for 12 h in air atmosphere. The dried precursors were heated to  $500^\circ\text{C}$  for pre-pyrolysis at a heating rate of  $10 \text{ K min}^{-1}$  in Ar flow ( $0.5 \text{ L min}^{-1}$ ) in a vertical tubular reactor. After naturally cooled down to room temperature, the precursor powders were collected and roughly pulverized using a mortar and pestle. Subsequently, the precursor powders were calcined at  $1000^\circ\text{C}$  with a heating rate of  $10 \text{ K min}^{-1}$  for 3 h under Ar flow ( $0.2 \text{ L min}^{-1}$ ) in a tubular furnace. Finally, the calcined samples were leached with  $0.5 \text{ mol dm}^{-3}$  (M) HCl aqueous solution and then washed with

ultrapure distilled water and ethanol for several times, and dried at 60°C for 24 hours in air atmosphere.

*II. Carbonization temperature effect;* In this part, the NHPCs were prepared at different carbonization temperatures. 10 mmol  $\text{Mg}(\text{NO}_3)_2 \cdot 6\text{H}_2\text{O}$  and 20 mmol urea were dissolved in ultrapure distilled and impregnated with 1 g cotton cellulose. After pre-pyrolysis, the precursor powders were calcined from 700 to 1100°C and finally washed with HCl to get the final products.

*III. Urea amount effect;* In this part, to evaluate the effect of urea amount on the preparation of NHPCs, 10 mmol  $\text{Mg}(\text{NO}_3)_2 \cdot 6\text{H}_2\text{O}$ , 1 g cotton, and different amounts of urea (0, 20, 30, and 40 mmol) were used as the raw materials. The samples were obtained in the same procedures and carbonization temperature of 1000°C was used and finally washed with HCl to get the final products.

*IV. Magnesium salt amount effect;* In this part, the NHPCs were prepared by different magnesium salt amounts. Different amounts of  $\text{Mg}(\text{NO}_3)_2 \cdot 6\text{H}_2\text{O}$  (10 and 20 mmol) and urea (20 and 40 mmol) were used as the raw materials. The samples were obtained in the same procedures and carbonization temperature of 1000°C was used and finally washed with HCl to get the final products.

The NHPCs were denoted by  $\text{Mg}_x\text{Ur}_y\text{Cot}_1\text{g-temperature}$ , based on the magnesium salt amount, urea amount and carbonization temperature, for example,  $\text{Mg}_{10}\text{Ur}_0\text{Cot}_1\text{g-1000}$ ,  $\text{Mg}_{10}\text{Ur}_{20}\text{Cot}_1\text{g-1000}$  and so on. When magnesium acetate tetrahydrate was used, the samples were referred to as  $\text{MgAc}_{10}\text{Ur}_0\text{Cot}_1\text{g-1000}$  and  $\text{MgAc}_{10}\text{Ur}_{20}\text{Cot}_1\text{g-1000}$ .

## 2-2-2. Material characterizations

The samples were characterized by X-ray diffraction (XRD, Rigaku Miniflex with Cu K $\alpha$  radiation), transmission electron microscopy (TEM, 200 kV, JEOL, JEM-2010F) and scanning electron microscopy (SEM, JEOL, JSM-7400F) for their crystalline structure and morphology analysis. Surface functional groups and bonding characterization of the samples were performed on X-ray photoelectron spectroscopy (XPS, JEOL, JPS-9200) system using Mg-K $\alpha$  X-ray source ( $h\nu=1253.6$  eV) under high vacuum condition of around  $5.0 \times 10^{-6}$  Pa.

The pyrolysis behavior for the nitrate, urea, cotton, and their mixtures were evaluated by a thermogravimetric (TG) analyzer combined with a differential scanning calorimetric (DSC) analyzer (Mettler Toledo). TG was also used to determine the carbon contents of the calcined  $\text{MgO}@C$  composites by their air-combustion in TG.

The specific surface area (SSA), pore volume and pore size distribution of the samples were characterized by  $\text{N}_2$  adsorption/desorption at -196°C using a Microtrac-BEL (BELSORP-mini) surface area analyzer.

The total pore volumes ( $V_{0.95}$ ) were determined from the amount of  $N_2$  adsorbed at the relative pressure  $P/P_0$  of 0.95, corresponding to pores with diameters up to around 40 nm. The SSA was calculated by both Brunauer-Emmett-Teller (BET) and t-plot methods. The t-plot analysis deduced the total surface area ( $a_{total}$ ), external surface area ( $a_{ex}$ ) and micropore volume ( $V_{micro}$ ). Base on this, the micropore surface area ( $a_{micro}$ ) was determined by  $a_{total}-a_{ex}$ , and the mesopore volume ( $V_{meso}$ ) was calculated by  $V_{0.95}-V_{micro}$ . Here  $V_{0.95}$  was used as the sum of meso- and micropore to avoid the over estimation of mesopore volume. The pore size distributions were estimated by a non localized density functional theory (NLDFT) method.

## 2-3. Results and discussion

### 2-3-1. Observation of the precursor

As shown in **Figure 2-2**, it is confirmed that the raw cotton fibers have diameters of several tens of micrometers and are hollow. These fibers can retain their morphology after the direct pyrolysis at 500 and 1000°C under Ar atmosphere, although the fibers became shorter. **Figure 2-3** shows the SEM images of the cotton fibers after the absorption and drying of magnesium nitrate and magnesium nitrate-urea aqueous solutions. The cellulose fibers can retain their fiber shape after the absorption of nitrate or nitrate-urea, indicating the impregnation of nitrate or nitrate-urea into the fibers.

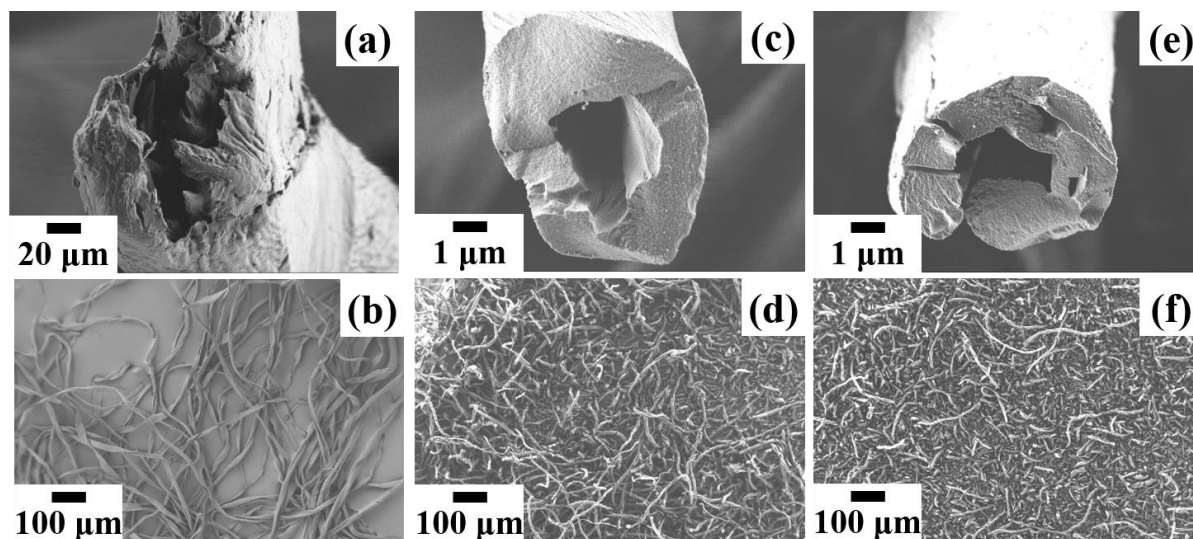


**Figure 2-2.** SEM images of the original cotton fibers (a, b); fibers calcined at 500 °C (c, d); and fibers calcined at 1000 °C (e, f) under Ar atmosphere.

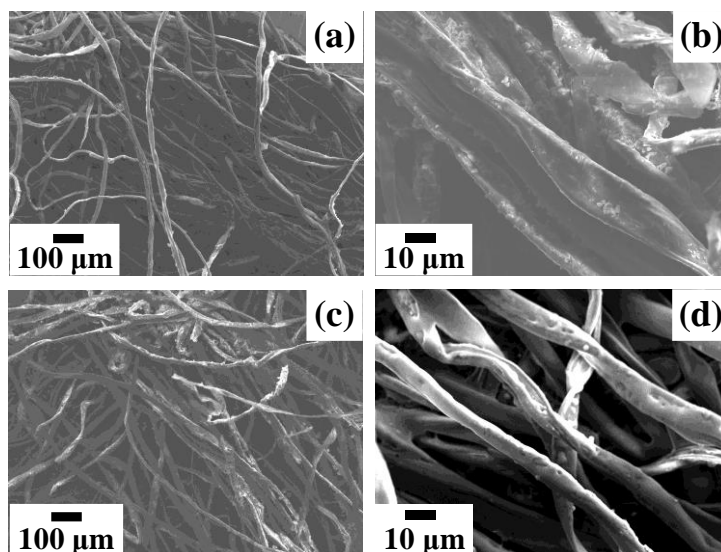


**Figure 2-3.** SEM images for the cotton fiber after the absorption of magnesium nitrate (a,b; Mg10Ur0Cot1g) and magnesium nitrate-urea (c, d; Mg10Ur20Cot1g).

### 2-3-2. Exothermic pre-pyrolysis

The pyrolysis of metal nitrate and urea is a well-known solution combustion synthesis (SCS) process to produce metal oxides.<sup>1, 2</sup> SCS is an exothermic and self-sustaining redox reaction process, which occurs at around 150–300°C with the emission of a large amount of gases in a short period. The key for the SCS process is the employment of nitrates as an oxidizer and organic compounds as the reductant fuels, such as urea, glycine, and citric acid etc, to form an intensive exothermic redox reaction. The simultaneous absorption of magnesium nitrate and urea in cotton fibers can accelerate the pyrolysis of cellulose. It is noted that cellulose itself can also be a reductant fuel when mixing with nitrates to form an exothermic reaction like SCS, although the fibers are in a solid form.

To evaluate the pyrolysis behaviors, different raw materials including magnesium nitrate, urea, cotton, and their mixtures were heated in a TG-DSC measurement setup under Ar flow, as shown in **Figure 2-4**. The decomposition of magnesium nitrate, urea and cotton are all endothermic reactions. The complete decomposition of magnesium nitrate needs a temperature of higher than around 500°C, while the decomposition of urea finishes at around 450°C. The pyrolysis of cotton cellulose starts at around 310°C and finishes at around 390°C. The pyrolysis of magnesium nitrate-urea shows a weak exothermic reaction at around 320°C under the Ar atmospheres. It is very interesting that when cotton cellulose is mixed with magnesium nitrate or magnesium nitrate-urea, a high exothermic reaction occurs at 150 and 200°C, respectively. Here, magnesium nitrate acts the oxidizer, while urea and/or cotton cellulose are employed as the reductant fuel to form the redox exothermic reaction. It is observed in the experiment that the addition of urea can make a homogeneous distribution of magnesium nitrate and

urea as-adsorbed in cotton fibers as compared to that of only magnesium nitrate, which is due to the chelating of urea molecule with nitrate. As shown in **Figure 2-3**, some particles referring to magnesium nitrate are dispersed on the fibers for the nitrate-cotton precursor, while the surface of the fibers are smooth when magnesium nitrate and urea are absorbed. Furthermore, the addition of urea together with magnesium nitrate can make a good exfoliation of cotton fibers to highly porous architecture and also offer nitrogen-doping to the final carbon product. It is observed that, during the pyrolysis process under Ar flow in a vertical tubular reactor, magnesium nitrate and nitrate-urea absorbed cotton fibers emitted a large amount of gases and the pyrolysis process finished in several minutes; however, the pyrolysis for cotton required much longer time and higher temperature. In order to demonstrate the importance of using nitrate as the oxidizer in the redox exothermic reaction, magnesium acetate was also used to substitute its nitrate. As shown in

**Figure 2-4**, an obvious exothermic reaction is not observed for the pyrolysis of the magnesium acetate-added cotton fibers (samples MgAc10Ur0Cot1g and MgAc10Ur20Cot1g).

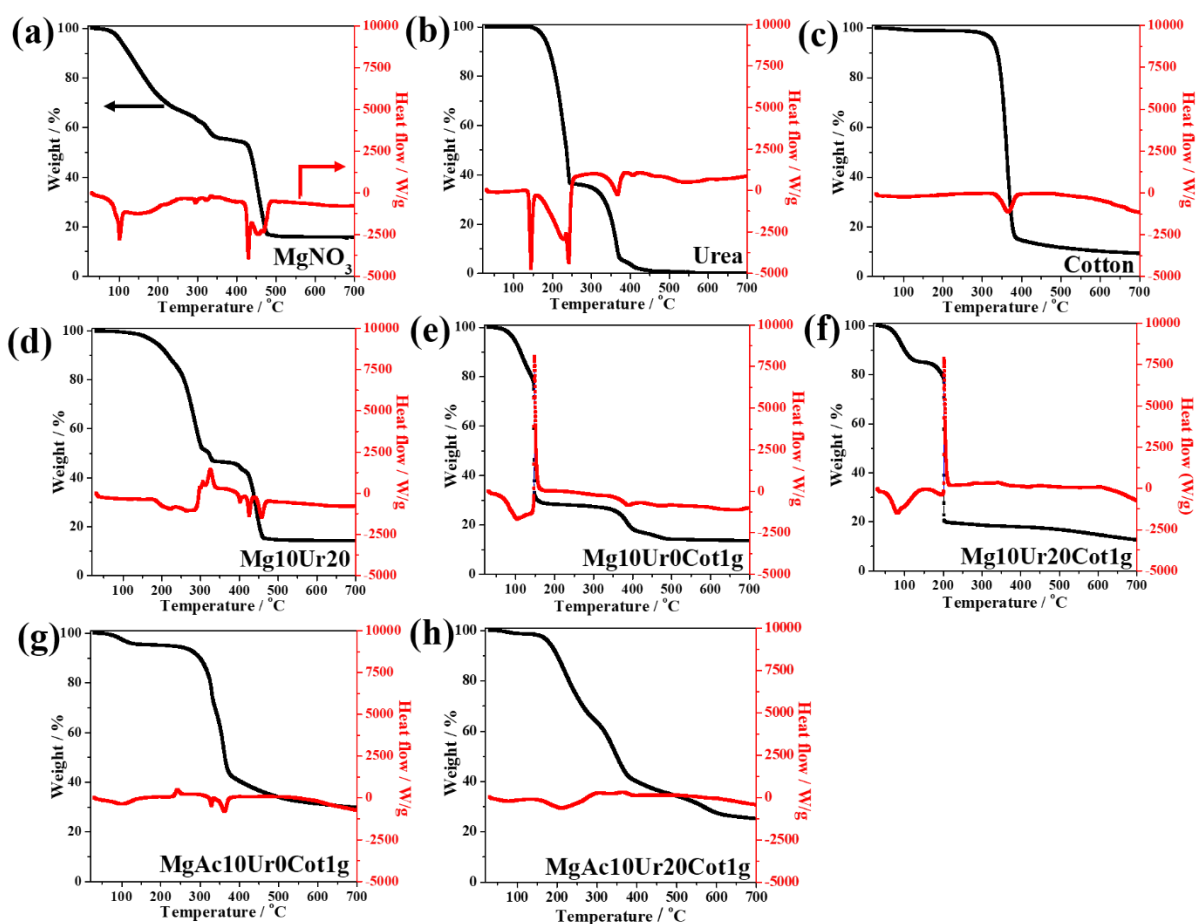


**Figure 2-4.** TG-DSC curves of pyrolysis behavior of different precursors: (a) magnesium nitrate hexahydrate, (b) urea, (c) cotton, (d) Mg10Ur20, (e) Mg10Ur0Cot1g, (f) Mg10Ur20Cot1g, (g) MgAc10Ur0Cot1g, and (h) MgAc10Ur20Cot1g.

The nitrate-induced exothermic reaction can accelerate the pyrolysis of cotton fibers and exfoliated the fibers to 3D highly porous architecture, while the acetate-induced samples retain almost the original fiber shape, as shown by the comparison of SEM images of the pre-pyrolyzed samples in **Figure 2-5**. Further comparison of these differences at various production conditions will be shown later by their calcined samples and acid washed samples.

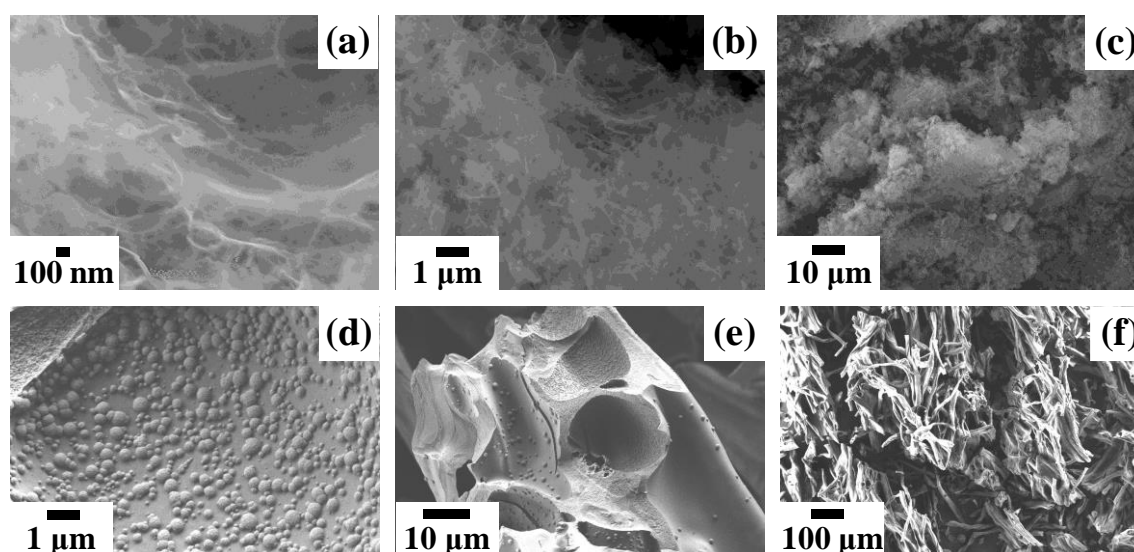


**Figure 2-5.** SEM images of the pre-pyrolyzed samples Mg10Ur20Cot1g-500 (a, b, c) and MgAc10Ur20Cot1g-500 (d, e, f).

### 2-3-3. Structure characterization of MgO@C precursors & the NHPCs by XRD

**Figure 2-6** shows the XRD patterns for the samples after carbonization and after acid washing, respectively. The samples are classified in terms of four experimental parameters, including magnesium salt species, carbonization temperature, urea amount and magnesium nitrate amount.

After carbonization, all samples present XRD peaks that can be indexed to MgO phase (JCPDS No: 00-004-0829). The peaks for carbon are not detected due to the low crystallinity of the annealed carbon. After acid washing, from the XRD patterns, it is confirmed that the peaks belonging to MgO phase disappear for all samples and broadened peaks corresponding to carbon 002 and 10 peaks are observed, indicating the successful removing of MgO by acid leaching.

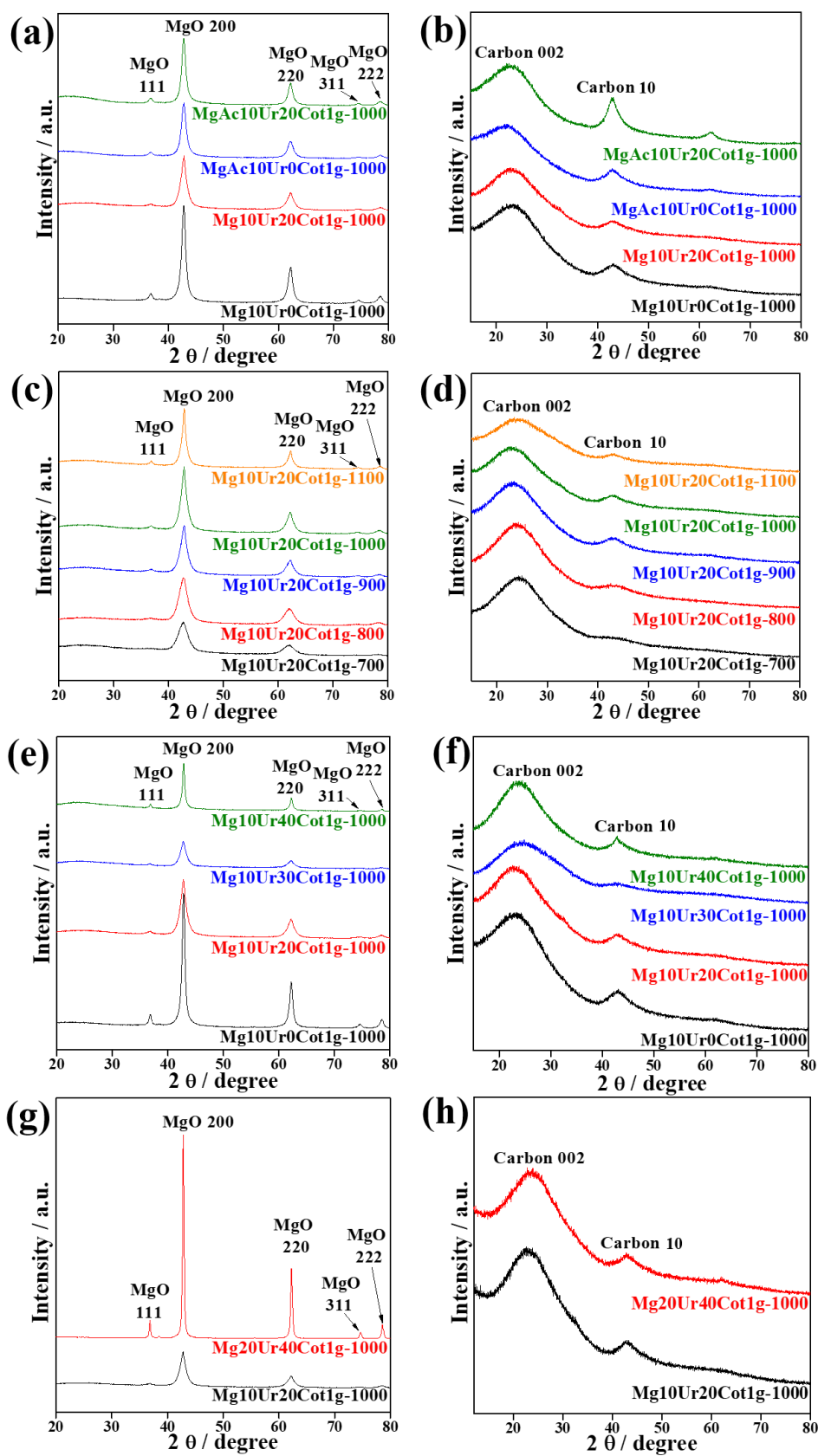
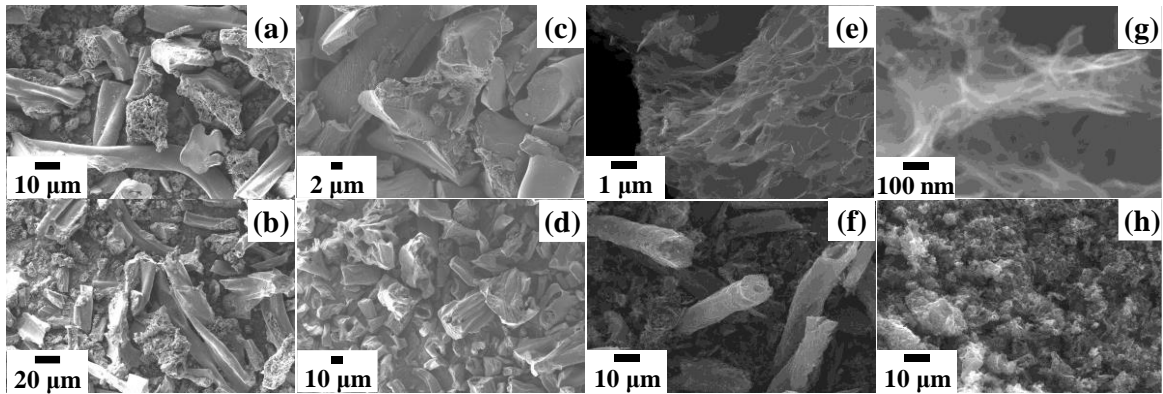


Figure 2-6. XRD patterns of the samples obtained after carbonization (a, c, e, g) and acid washing (b, d, f, h), respectively. (a, b) species of magnesium salt effect, (c, d) carbonization temperature effect, (e, f) urea amount effect, and (g, h) magnesium salt amount effect.

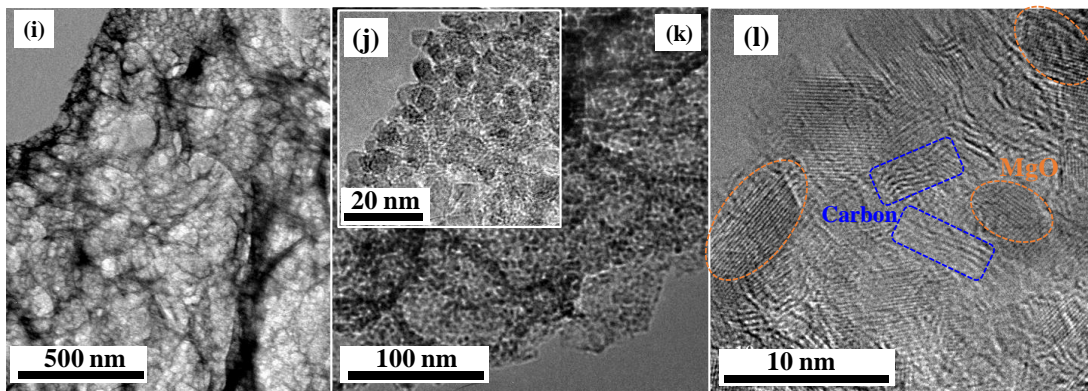
#### 2-3-4. Morphology characterization of MgO@C precursors & the NHPCs by SEM and TEM

The micromorphology of the calcined MgO@C composites and acid washed samples were observed by SEM. **Figure 2-7(a-h)** shows the typical SEM images for the samples after acid washing to compare the effect of the addition of magnesium nitrate and magnesium acetate in the raw materials. The acetate-induced samples (MgAc10Ur0Cot1g-1000 and MgAc10Ur20Cot1g-1000) present the bulky pulverized micron fibers, which are not porous. However, the nitrate-induced samples (Mg10Ur0Cot1g-1000 and Mg10Ur20Cot1g-1000) show greatly 3D porous architectures, which contains pores in a wide range from several tens of nanometers to several hundreds of nanometers. Sample Mg10Ur0Cot1g-1000 contains some porous fibers as a clue of its raw material of cotton fibers, while sample Mg10Ur20Cot1g-1000 consists of highly porous powders indicating the complete exfoliation of cotton fibers by a nitrate-urea-induced exothermic reaction as-absorbed in the fibers.

**Figure 2-7 (i-p)** shows the typical TEM observation results for the highly porous samples of Mg10Ur0Cot1g-1000 obtained at the stages of after carbonization and after acid washing. For the MgO@C precursor obtained after carbonization, the TEM image at a low magnification (**Figure 2-7(i)**) indicates that the calcined sample is highly porous, containing a large number of interconnected mesopores in the range of several tens of nanometers (< 50 nm) and macropores in the range of several tens of nanometers (> 50 nm) to several hundreds of nanometers. The TEM observation at larger magnifications (**Figure 2-7(j, k, l)**) illustrates that the porous carbon matrix is incorporated with plenty of MgO nanoparticles with size ranging from several nanometers to dozens of nanometers. After acid washing to remove the MgO nanoparticles, it is confirmed that a highly porous carbon with numerous interconnected meso- and macropores is produced (**Figure 2-7(m)**). The porous carbon is constructed of very thin layers of porous nanosheets. The high-resolution images in **Figure 2-7 (o, p)** indicate that the sample is highly defective although some distorted lattice fringes corresponding to the carbon 002 plane can be seen. More importantly, the sample contains abundant micropores and mesopores of several nanometers. The selected area electron diffraction (SAED) pattern is shown in **Figure 2-7-(n)**, representing a typical amorphous carbon structure.



*Mg10Ur20Cot1g-1000, after calcination*



*Mg10Ur20Cot1g-1000, after acid washing*

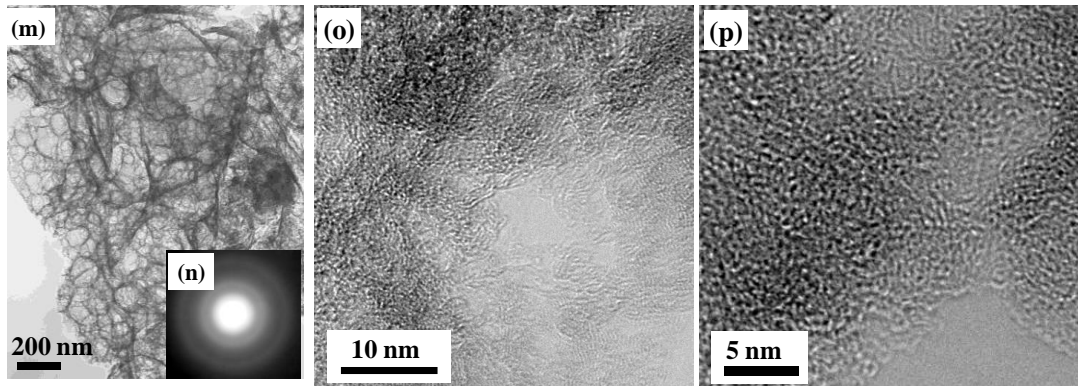


**Figure 2-7. Morphology observation results. Typical SEM images of the samples after acid washing: (a-b) MgAc10Ur0Cot1g-1000, (c-d) MgAc10Ur20Cot1g-1000, (e-f) Mg10Ur0Cot1g-1000, and (g-h) Mg10Ur20Cot1g-1000. TEM observation results for the highly porous MgO@C precursor (i, j, k, l) and the corresponding carbon sample (m, n, o, p) for sample Mg10Ur20Cot1g-1000. (i, m) Typical TEM images at low magnifications; (j, k) typical TEM images at high magnifications; (l, o, p) the high-resolution TEM images at high magnifications; (n) a typical SAED pattern.**

SEM images for the calcined MgO@C samples and NHPCs, including another three experimental parameters, are shown in **Figure 2-8** to **Figure 2-10** and **Figure 2-11** to **Figure 2-13**, respectively. All of the calcined MgO@C samples, as shown in **Figure 2-8** and **Figure 2-9**, show the

3D porous architectures, which contains MgO particles and pores in a wide range from several tens of nanometers to several hundreds of nanometers.

As shown in **Figure 2-10**, Mg<sub>20</sub>Ur<sub>40</sub>Cot<sub>1g</sub>-1000 has too much magnesium precursor, that will make an excess ratio of MgO template in MgO@C composites, and in this case, the original porous structure may collapse. As shown in **Figure 2-11** to **Figure 2-13**, NHPCs, after acid washing to remove the MgO nanoparticles, it is confirmed that a highly porous carbon with numerous interconnected meso- and macropores is produced. However, it is difficult to discuss about SSA and pore size distribution by morphology observation. So, the details of SSA and pore size distribution will be discussed by N<sub>2</sub> absorption measurement in the next part.

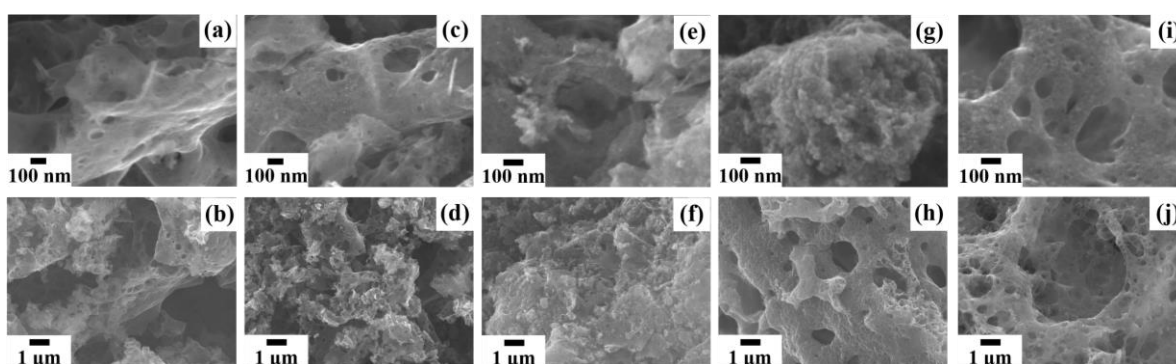


**Figure 2-8.** SEM images of the calcined samples obtained with different temperatures: (a-b) Mg<sub>10</sub>Ur<sub>20</sub>Cot<sub>1g</sub>-700; (c-d) Mg<sub>10</sub>Ur<sub>20</sub>Cot<sub>1g</sub>-800; (e-f) Mg<sub>10</sub>Ur<sub>20</sub>Cot<sub>1g</sub>-900; (g-h) Mg<sub>10</sub>Ur<sub>20</sub>Cot<sub>1g</sub>-1000; and (i-j) Mg<sub>10</sub>Ur<sub>20</sub>Cot<sub>1g</sub>-1100

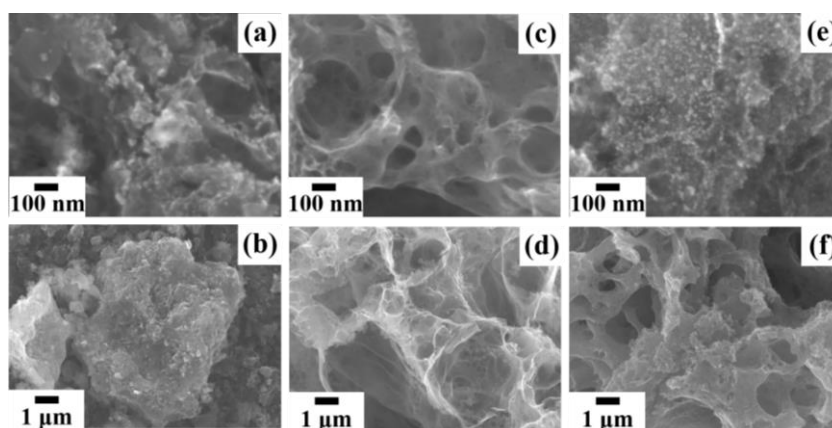


**Figure 2-9.** SEM images of the calcined samples obtained with different urea amount: (a-b) Mg<sub>10</sub>Ur<sub>0</sub>Cot<sub>1g</sub>-1000; (c-d) Mg<sub>10</sub>Ur<sub>30</sub>Cot<sub>1g</sub>-1000; and (e-f) Mg<sub>10</sub>Ur<sub>40</sub>Cot<sub>1g</sub>-1000.

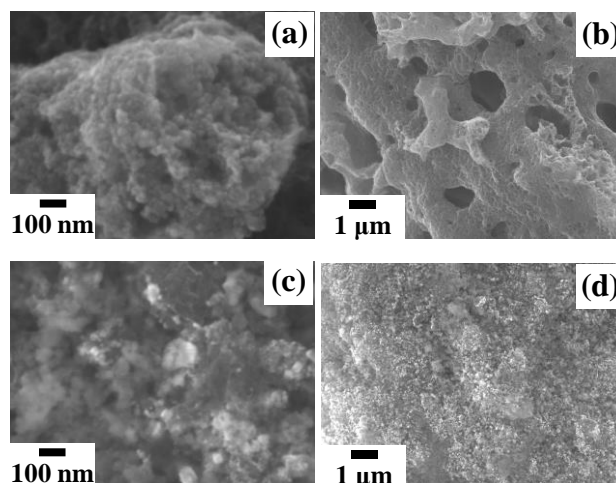


Figure 2-10. SEM images of the calcined samples obtained with different magnesium salt amount: (a-b) Mg10Ur20Cot1g-1000 and (c-d) Mg20Ur40Cot1g-1000.

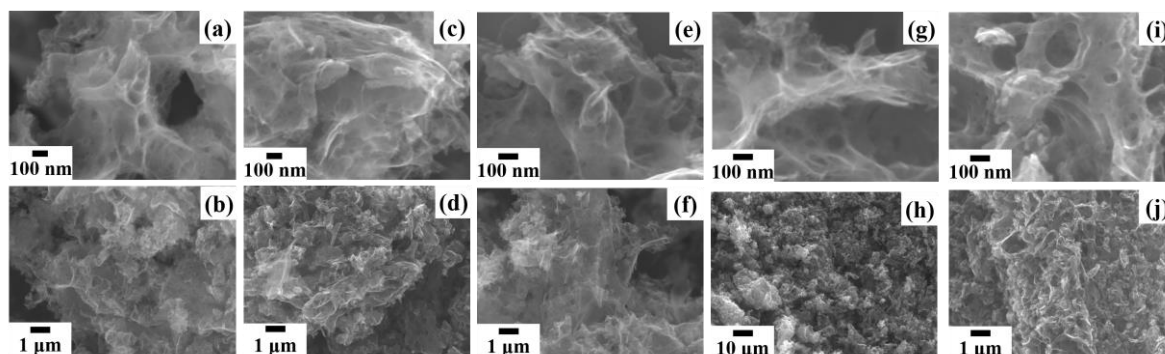


Figure 2-11. SEM images of the final samples obtained after acid washing which were calcined at different temperatures: (a-b) Mg10Ur20Cot1g-700; (c-d) Mg10Ur20Cot1g-800; (e-f) Mg10Ur20Cot1g-900; (g-h) Mg10Ur20Cot1g-1000 and (i-j) Mg10Ur20Cot1g-1100.

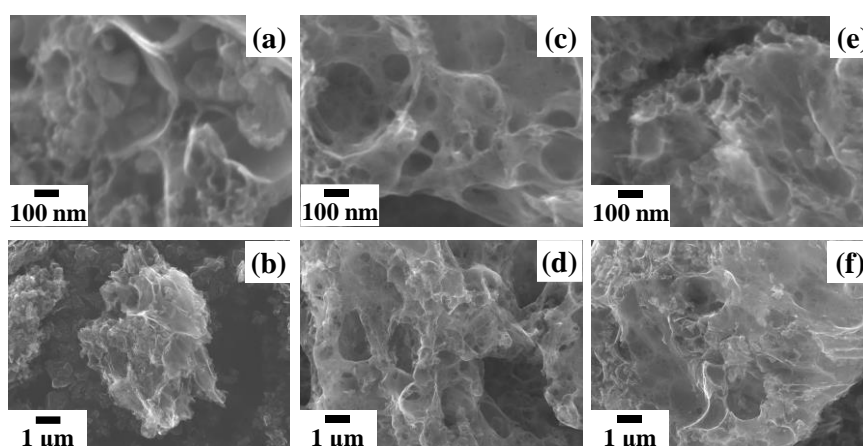
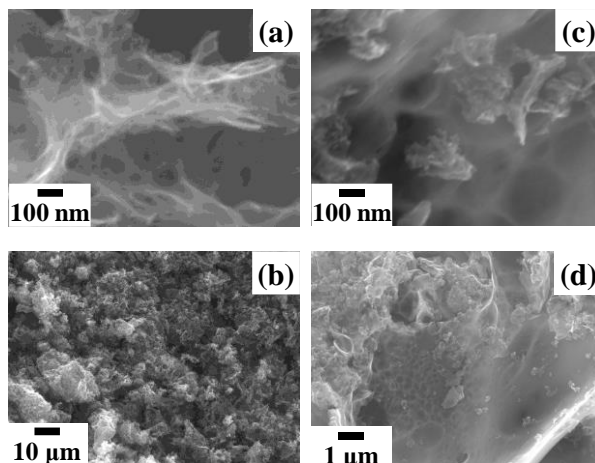


Figure 2-12. SEM images of the final samples obtained after acid washing with different urea amount: (a-b) Mg10Ur0Cot1g-1000; (c-d) Mg10Ur30Cot1g-1000; and (e-f) Mg10Ur40Cot1g-1000.



**Figure 2-13. SEM images of the final samples obtained after acid washing with different magnesium salt amount: (a-b) Mg10Ur20Cot1g-1000 and (c-d) Mg20Ur40Cot1g-1000.**

### **2-3-5. Pore structure characterization of MgO@C composites by N<sub>2</sub> adsorption/desorption measurements.**

The porous characteristics, including specific surface area (SSA), pore volume and pore size distribution, of the calcined MgO@C composites with four experimental parameters, including magnesium salt, carbonization temperature, urea amount and MgO template amount, were further evaluated by N<sub>2</sub> adsorption/desorption experiments, as shown in **Figure 2-14**. The details for the comparison of SSA and pore volumes are also summarized in **Table 2-1**.

**Figure 2-14** shows the N<sub>2</sub> adsorption/desorption isotherms (a, c, e, g) and NLDFT pore size distribution (b, d, f, h) of the calcined MgO@C composites obtained with different four experimental parameters. As shown in **Figure 2-14** (a), the calcined MgO@C composites illustrate the hysteresis type isotherms (absorption-desorption hysteresis with relative pressure  $P/P_0$  ranging from ~0.5 to 0.8), indicating the existence of mesopores. It is noted that the magnesium nitrate-derived composites present larger hysteresis as compared to that for magnesium acetate-derived samples. The isotherms for these composites show limited adsorption at  $P/P_0$  less than 0.1, indicating the shortage of micropores for these samples. The magnesium nitrate-derived composites show a sharp increase of adsorption at a relative pressure of ~0.9–1.0, demonstrating the presence of macropores. However, such a sharp increase is not observed for magnesium acetate-derived samples. NLDFT pore size distribution is shown in **Figure 2-14** (b), further confirming the absence of macropores for the acetate-derived samples. This observation about the difference in the pore structure of the MgO@C composites obtained with different magnesium salts demonstrates the importance of the nitrate-assisted exothermic reaction in creating numerous meso-macropores by exfoliating the micrometer-sized cotton fibers to highly 3D porous architecture, which was also confirmed in previous morphology observation.

The N<sub>2</sub> adsorption/desorption isotherms of another three experimental parameters, including carbonization temperature, urea amount and magnesium salt amount, are also shown in **Figure 2-14 (c)**, **Figure 2-14 (e)**, and **Figure 2-14 (g)**, respectively. The calcined MgO@C composites with different experimental parameters also present hysteresis type isotherms, suggesting that mesopores exist in these samples. The isotherms for these composites also show limited adsorption at P/P<sub>0</sub> less than 0.1, indicating the shortage of micropores for these samples. Additionally, the calcined MgO@C composites with different experimental parameters show a sharp increase of adsorption at a relative pressure of ~0.9–1.0, demonstrating the presence of macropores. The NLDFT pore size distribution of these samples are shown in **Figure 2-14 (d)**, **Figure 2-14 (f)**, and **Figure 2-14 (h)**, respectively.

**Table 2-1. Summary of the porous characteristics for MgO@C composites obtained after carbonization.**

| <i>Samples</i>     | BET SSA<br>(m <sup>2</sup> g <sup>-1</sup> ) | V <sub>0.95</sub><br>(cm <sup>3</sup> g <sup>-1</sup> ) | <i>Samples</i>       | BET SSA<br>(m <sup>2</sup> g <sup>-1</sup> ) | V <sub>0.95</sub><br>(cm <sup>3</sup> g <sup>-1</sup> ) |
|--------------------|--|---|----------------------|--|---|
| Mg10Ur20Cot1g-700  | 132.8  | 0.29  | MgAc10Ur0Cot1g-1000  | 317.7  | 0.23  |
| Mg10Ur20Cot1g-800  | 164.5  | 0.34  | MgAc10Ur20Cot1g-1000 | 108.7  | 0.15  |
| Mg10Ur20Cot1g-900  | 170.5  | 0.33  | Mg10Ur0Cot1g-1000    | 202.0  | 0.23  |
| Mg10Ur20Cot1g-1000 | 225.0  | 0.37  | Mg10Ur30Cot1g-1000   | 241.5  | 0.40  |
| Mg10Ur20Cot1g-1100 | 208.5  | 0.35  | Mg10Ur40Cot1g-1000   | 110.5  | 0.23  |
|                    |  |   | Mg20Ur40Cot1g-1000   | 59.4   | 0.13  |

BET SSA: specific surface area as-calculated from the adsorption data by BET method; V<sub>0.95</sub>: total pore volume at P/P<sub>0</sub>=0.95, corresponding to the pores with diameters up to around 40 nm;

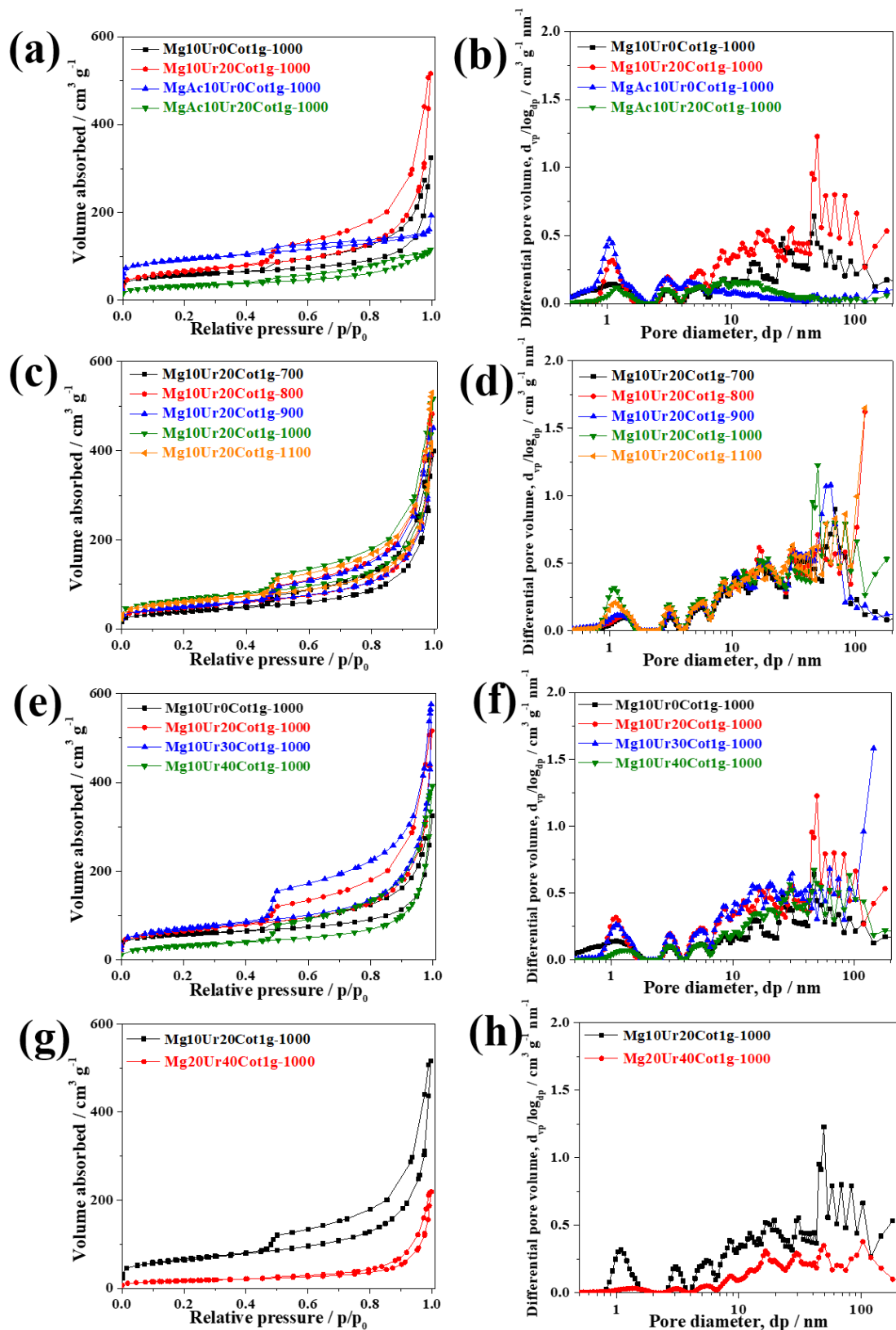


Figure 2-14.  $N_2$  adsorption/desorption isotherms (a, c, e, g) and NLDFT pore size distribution (b, d, f, h) for the calcined  $MgO@C$  composites. (a, b) species of magnesium salt effect, (c, d) carbonization temperature effect, (e, f) urea amount effect, and (g, h) magnesium salt amount effect.

### 2-3-6. Pore structure characterization of the NHPCs by N<sub>2</sub> adsorption/desorption measurement

**Figure 2-15** shows the N<sub>2</sub> adsorption/desorption isotherms (a, c, e, g) and NLDFT pore size distribution (b, d, f, h) of the NHPCs, after acid washing of the calcined MgO@C composites obtained with four different experimental parameters. The details for the comparison of SSA and pore volumes for these samples are also summarized in **Table 2-2**.

As for the species of magnesium effect, shown in **Figure 2-15** (a), magnesium nitrate-derived composites present larger hysteresis at a relative pressure of ~0.5–0.8 and more adsorption at a relative pressure of ~0.9–1.0, demonstrating the presence of meso-, and macropores as compared to that for magnesium acetate-derived samples. NLDFT pore size distribution is shown in **Figure 2-15** (b), further confirming the absence of macropores for the acetate-derived samples. This observation about the difference in the pore structure of the NHPCs obtained with different magnesium salts demonstrates the importance of the nitrate-assisted exothermic reaction in creating numerous meso- and macropores by exfoliating the micron-sized cotton fibers to highly 3D porous architecture, which was also confirmed in previous morphology observation.

As for the carbonization temperature effect, as shown in **Figure 2-15** (c) and **Figure 2-15** (d), the SSA of the carbon samples is increased from around 1000 m<sup>2</sup> g<sup>-1</sup> at 700°C to larger than 1100 m<sup>2</sup> g<sup>-1</sup> when the temperature is higher than 800°C. The values of total SSA for the carbon samples calcined from 800-1100°C are similar; however, the external surface area and pore volume show an increasing tendency with temperature. As confirmed by pore size distributions in **Figure 2-15** (d), the samples present pore size shift to higher values as carbonization temperature, which is caused by the crystal growth of the MgO template.

As for the urea amount effect, as shown in **Figure 2-15** (e) and **Figure 2-15** (f), when too much urea (40 mmol) is added, the obtained carbon product shows greatly decreased SSA from larger than 1000 m<sup>2</sup> g<sup>-1</sup> to around 400 m<sup>2</sup> g<sup>-1</sup>. This is because of that urea is also a carbon source, and in this case, too much urea makes a greatly weakened exothermic reaction and greatly decreased the ratio of MgO template in the MgO@C composite. Thereby, a decreased number of pores are created when an excess amount of urea is added. It is found that the optimal urea amount is 20 mmol, making the sample Mg10Ur20Cot1g-1000 have the highest SSA and well-developed hierarchical pore structure, indicating the highest ORR catalytic properties which will be discussed in detail in following Chapter 3.

As for the magnesium salt amount effect, as shown in **Figure 2-15** (g) and **Figure 2-15** (h), too much addition of magnesium precursor will make an excess ratio of MgO template in MgO@C composites, and in this case, the original porous structure may collapse when removing the template. Therefore, the SSA and pore volume are greatly decreased when the MgO template amount is twice.

**Table 2-2. Summary of the porous characteristics of porous carbon products obtained after acid washing.**

|                      | BET<br>SSA<br>(m <sup>2</sup> g <sup>-1</sup> ) | a <sub>total</sub><br>(m <sup>2</sup> g <sup>-1</sup> ) | a <sub>ex</sub><br>(m <sup>2</sup> g <sup>-1</sup> ) | a <sub>micro</sub><br>= a <sub>total</sub> - a <sub>ex</sub><br>(m <sup>2</sup> g <sup>-1</sup> ) | V <sub>0.95</sub><br>(cm <sup>3</sup> g <sup>-1</sup> ) | V <sub>micro</sub><br>(cm <sup>3</sup> g <sup>-1</sup> ) | V <sub>meso</sub><br>= V <sub>0.95</sub> -<br>V <sub>micro</sub><br>(cm <sup>3</sup> g <sup>-1</sup> ) |
|----------------------|---|---|--|---|---|--|--|
| Mg10Ur20Cot1g-700    | 993.7   | 1019.7  | 359.4  | 660.3   | 1.05  | 0.39   | 0.66   |
| Mg10Ur20Cot1g-800    | 1191.3  | 1189.9  | 445.5  | 744.4   | 1.33  | 0.53   | 0.80   |
| Mg10Ur20Cot1g-900    | 1113.9  | 1079.1  | 459.7  | 619.4   | 1.35  | 0.51   | 0.84   |
| Mg10Ur20Cot1g-1000   | 1173.4  | 1158.2  | 495.2  | 663.0   | 1.51  | 0.61   | 0.90   |
| Mg10Ur20Cot1g-1100   | 1162.8  | 1166.5  | 549.3  | 617.2   | 1.59  | 0.61   | 0.98   |
| MgAc10Ur0Cot1g-1000  | 720.0   | 705.1   | 54.3   | 695.8   | 0.68  | 0.59   | 0.09   |
| MgAc10Ur20Cot1g-1000 | 252.2   | 250.6   | 52.0   | 198.6   | 0.33  | 0.25   | 0.08   |
| Mg10Ur0Cot1g-1000    | 969.2   | 1037.8  | 129.4  | 908.4   | 0.69  | 0.46   | 0.23   |
| Mg10Ur30Cot1g-1000   | 1020.5  | 1027.2  | 549.6  | 477.6   | 1.43  | 0.45   | 0.98   |
| Mg10Ur40Cot1g-1000   | 400.3   | -   | -  | -   | 0.73  | 0.04   | 0.69   |
| Mg20Ur40Cot1g-1000   | 886.9   | 862.2   | 514.1  | 348.1   | 1.29  | 0.35   | 0.94   |

BET SSA: specific surface area as-calculated from the adsorption data by BET method; V<sub>0.95</sub>: total pore volume at P/P<sub>0</sub>=0.95, corresponding to the pores with diameters up to around 40 nm; a<sub>total</sub>: the total surface area as-determined by t method; a<sub>ex</sub>: the external surface area as-determined by t method; a<sub>micro</sub>: the micropore surface area as-determined by a<sub>total</sub>-a<sub>ex</sub>; V<sub>micro</sub>: the micropore volume as-analyzed by t method; V<sub>meso</sub>: the mesopore volume as-determined by V<sub>0.95</sub>-V<sub>micro</sub>. Sample Mg10Ur40Cot1g-1000 is not applicable to t-plot analysis due to the lack of micropore for this sample.

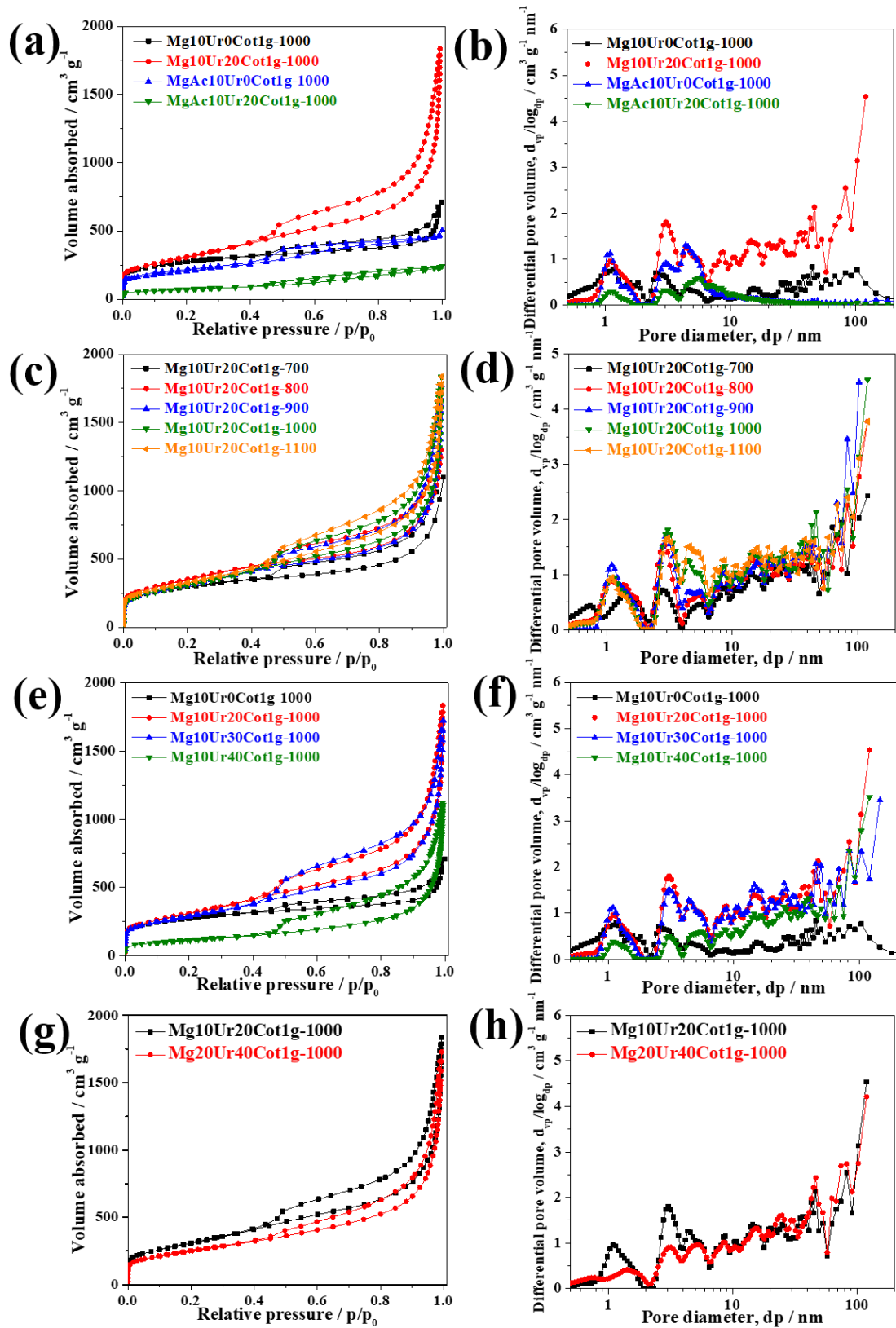
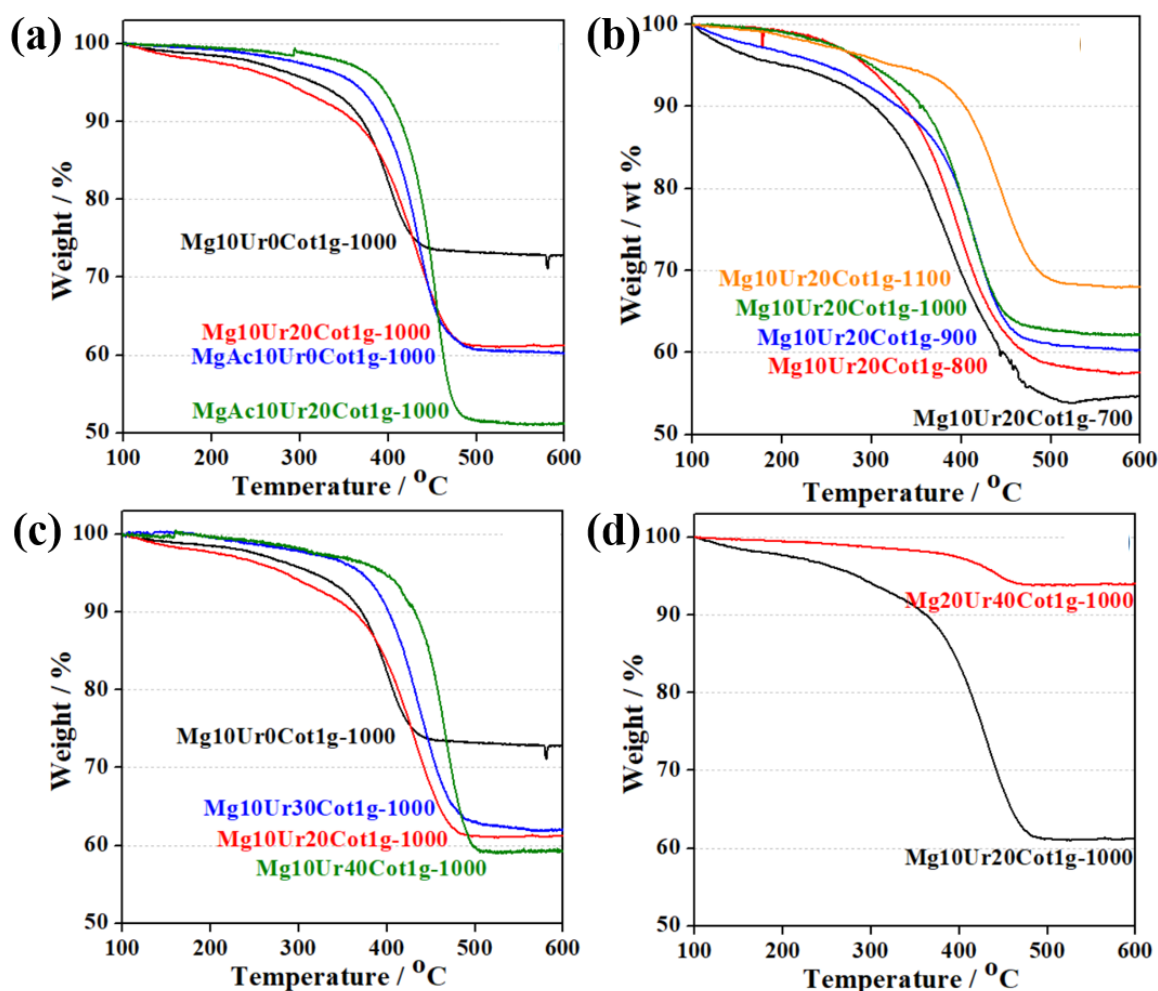


Figure 2-15.  $N_2$  adsorption/desorption isotherms (a, c, e, g) and NLDFT pore size distribution (b, d, f, h) for the NHPCs. (a, b) species of magnesium salt effect, (c, d) carbonization temperature effect, (e, f) urea amount effect, and (g, h) magnesium salt amount effect.

### 2-3-7. TG air combustion analysis to determine the yield

The carbon ratios in the MgO@C composites were determined by their combustion in oxygen flow in a TG analyzer, as shown in **Figure 2-16**. The carbon percentages in the MgO@C composites were determined by the weight loss from 100 to 600°C since carbon is combusted to CO<sub>2</sub> gas in temperature ranging from around 300 to 500°C, making the weight loss, while magnesium oxide is retained after carbon is combusted. Note that carbon ratio here refers to the amorphous carbon with doping elements such as N, O, and H, which were also combusted to gases during the measurement. Based on the carbon ratios in the MgO@C composites, we can calculate the theoretical yields with a unit of g-carbon/g-cotton for these samples, correspondingly. The results are summarized in **Table 2-3**.



**Figure 2-16.** TG curves of calcined samples under air flow to determine the carbon content in the calcined MgO@C composites. (a) species of magnesium salt effect (b) carbonization temperature effect, (c) urea amount effect, and (d) magnesium salt amount effect.

**Table 2-3. Summary of the carbon ratios in MgO@C precursors and production yield of carbon in a unit of g-carbon/g-cotton.**

| <i>Samples</i>     | Carbon ratio in MgO@C (wt %) | Yield (g-carbon/g-cotton) | <i>Samples</i>       | Carbon ratio in MgO@C (wt %) | Yield (g-carbon/g-cotton) |
|--------------------|------------------------------|---------------------------|----------------------|------------------------------|---------------------------|
| Mg10Ur20Cot1g-700  | 43.26                        | 0.31                      | MgAc10Ur0Cot1g-1000  | 40.30                        | 0.27                      |
| Mg10Ur20Cot1g-800  | 40.90                        | 0.28                      | MgAc10Ur20Cot1g-1000 | 48.65                        | 0.38                      |
| Mg10Ur20Cot1g-900  | 39.83                        | 0.27                      | Mg10Ur0Cot1g-1000    | 27.24                        | 0.15                      |
| Mg10Ur20Cot1g-1000 | 38.84                        | 0.26                      | Mg10Ur30Cot1g-1000   | 37.98                        | 0.25                      |
| Mg10Ur20Cot1g-1100 | 31.93                        | 0.19                      | Mg10Ur40Cot1g-1000   | 40.34                        | 0.27                      |
|                    |                              |                           | Mg20Ur40Cot1g-1000   | 5.74                         | 0.05                      |

### 2-3-8. XPS analysis

The characterization of the bonding features of the carbon samples was performed by XPS and Raman spectroscopy. **Figure 2-17** and **Figure 2-18** show the XPS measurement results. **Figure 2-17** (a) presents the XPS survey scan curves for the Mg10Ur20Cot1g samples with different carbonization temperatures, which show three peaks at ~285.0, 400.0 and 533.0 eV, referring to the C 1s, N 1s, and O 1s electrons, respectively.<sup>3,4</sup> Oxygen is normally contained in the amorphous carbon. The nitrogen atom is also doped in carbon since urea was added in the raw materials. The atomic percentages of N in (N+C) are determined to be 9.98, 9.28, 4.10, 2.02 and 1.03 % for the samples calcined from 700, 800, 900, 1000 and 1100°C, respectively. The ratio of doped nitrogen is decreased with carbonization temperature, especially when the temperature is higher than 800°C. The XPS survey scan curves for other samples obtained with different magnesium salt precursors, different urea amount, and different magnesium precursor amount are also presented in **Figure 2-17** (b), **Figure 2-17** (c) and **Figure 2-17** (d), respectively. At the same carbonization temperature of 1000°C and when urea is also added in the raw materials, the carbon samples present similar atomic percentages of N in (N+C), which are around 2.01~2.45%. When urea is not added in the raw materials, the obtained samples (MgAcUr0Cot1g-1000 and Mg10Ur0Cot1g-1000) present very limited N atomic percentages of lower than 1%, which is also properly derived from the measurement error. The N atomic percentages for these samples are summarized in **Table 2-4**.

The N 1s spectra for the samples with N-doping were carefully scanned, as presented in **Figure 2-18** (a) and **Figure 2-18** (b). The N 1s spectra can be divided into three typical peaks, representing the pyridinic N (~398.6 eV), pyrrolic or pyridonic N (~400.1 eV), and quaternary N (graphitic N, ~401.3 eV).<sup>5,6</sup> The ratios for the above three peaks are greatly influenced by carbonization temperature, which indicates an increasing ratio of graphitic N and decreasing ratios for pyridinic & pyrrolic N with an increase in carbonization temperature, as summarized in **Figure 2-18** (c) and **Figure 2-18** (d). Graphitic and pyridinic N are usually assumed to be the active sites for ORR.<sup>3,7</sup> With the increase of carbonization

temperature, the graphitization degree is enhanced, making a stable and high-conductive carbon, however, the doping amount of N is also decreased although the ratio for the sum of graphitic and pyridinic N is increased. Therefore, it is significantly important to find the optimized carbonization temperature to prepare a carbon sample with high ORR activities.

**Table 2-4. The atomic N percentage in (N+C) for the carbon samples analyzed by XPS.**

| <i>Samples</i>     | N/(C+N)<br>(atom. %) | <i>Samples</i>       | N/(C+N)<br>(atom. %) |
|--------------------|----------------------|----------------------|----------------------|
| Mg10Ur20Cot1g-700  | 9.98                 | MgAc10Ur0Cot1g-1000  | -                    |
| Mg10Ur20Cot1g-800  | 9.28                 | MgAc10Ur20Cot1g-1000 | 2.45                 |
| Mg10Ur20Cot1g-900  | 4.10                 | Mg10Ur0Cot1g-1000    | -                    |
| Mg10Ur20Cot1g-1000 | 2.02                 | Mg10Ur30Cot1g-1000   | 2.01                 |
| Mg10Ur20Cot1g-1100 | 1.03                 | Mg10Ur40Cot1g-1000   | 2.15                 |
|                    |                      | Mg20Ur40Cot1g-1000   | 2.45                 |

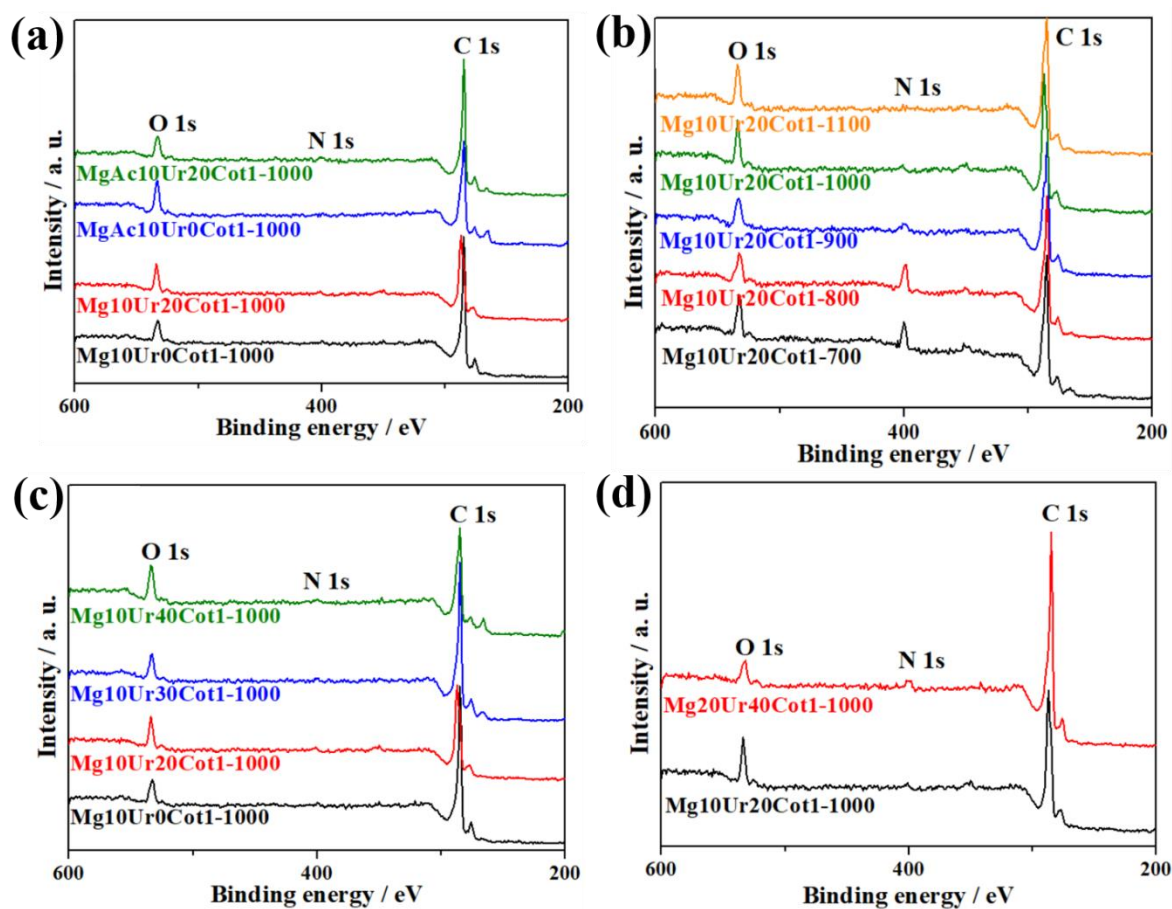


**Figure 2-17. XPS survey curves of the all samples. (a) species of magnesium salt effect (b) carbonization temperature effect, (c) urea amount effect, and (d) magnesium salt amount effect.**

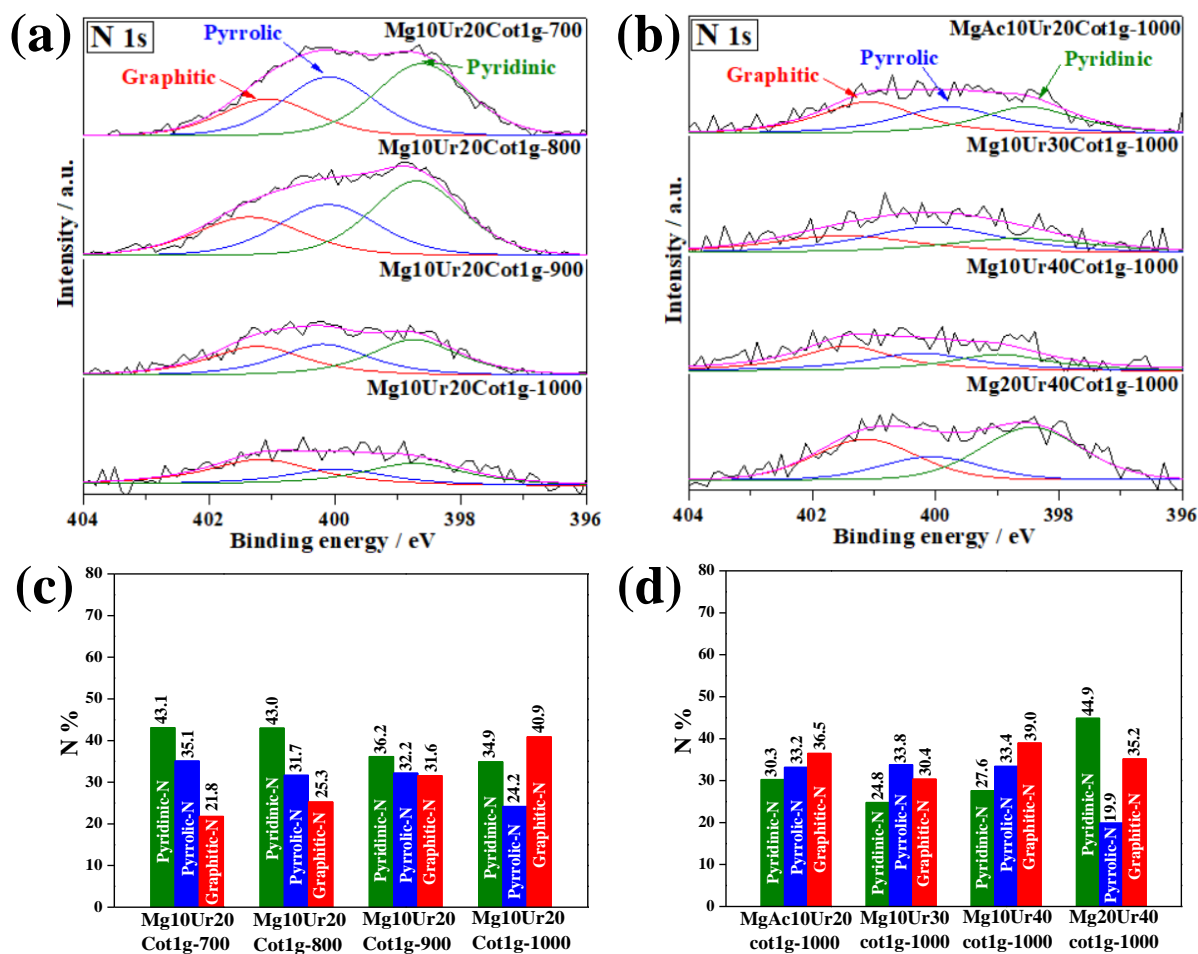


Figure 2-18. XPS analysis of the carbon samples. (a, b) the N 1s narrow scan, and (c, d) the summary of the percentage of different N species.

## 2-4. Conclusions

In summary, the exothermic reaction-induced formation of N-doped hierarchically porous carbon (NHPC) has been examined in this chapter. Cellulose fibers and urea are used as carbon and nitrogen sources, respectively. The accelerated pyrolysis of cellulose occurs with magnesium nitrate, which also introduces MgO template for pore generation. After pyrolysis, the samples have been further heat-treated at 700-1100°C, followed by acid washing to dissolve MgO template. Following conclusions are obtained in this chapter.

(1) The use of nitrate introduced the exothermic reactions promotes the pyrolysis at a low temperature and quickly exfoliate the cellulose fibers to highly porous architecture. However, the magnesium acetate-induced reaction is endothermic and the corresponding pyrolyzed samples still have the bulky fiber shape and is less porous.

(2) The carbonization temperature greatly influences the doping amount of N, the doping species

of N and the graphitization degree of carbon. The N content decreases with an increase in the carbonization temperature, and the relative amount of graphitic nitrogen increases with the carbonization temperature.

(3) Practically N-free carbon is formed without adding urea, but N-doped one is developed with the addition of urea in the precursors. Thus, urea, not nitrate, is a source of nitrogen in NHPC.

(4) MgO template was important for the creation of micro and mesopores. Thus, after acid washing to dissolve the MgO template, specific surface area, micropore volume and mesopore volume are highly increased.

## 2-5. Reference

- [1] C. Zhu, C.G. Han, T. Akiyama, Controlled synthesis of  $\text{LiNi}_{0.5}\text{Mn}_{1.5}\text{O}_4$  cathode materials with superior electrochemical performance through urea-based solution combustion synthesis, *RSC Adv.* 5 (2015) 49831-49837.
- [2] K.R. Prakasha, A.S. Prakash, A time and energy conserving solution combustion synthesis of nano  $\text{Li}_{1.2}\text{Ni}_{0.13}\text{Mn}_{0.54}\text{Co}_{0.13}\text{O}_2$  cathode material and its performance in Li-ion batteries, *RSC Adv.* 5 (2015) 94411-94417.
- [3] Y. Wang, H. Liu, K. Wang, S. Song, P. Tsiakaras, 3D interconnected hierarchically porous N-doped carbon with  $\text{NH}_3$  activation for efficient oxygen reduction reaction. *Appl. Catal. B* 210 (2017) 57-66.
- [4] Y. Chen, R. Ma, Z. Zhou, G. Liu, Y. Zhou, Q. Liu, S. Kaskel, J. Wang, An In Situ Source-Template-Interface Reaction Route to 3D Nitrogen-Doped Hierarchical Porous Carbon as Oxygen Reduction Electrocatalyst, *Adv. Mater. Interfaces* 2 (2015) 1500199.
- [5] Chung, D. Y.; Lee, K. J.; Yu, S. H.; Kim, M.; Lee, S. Y.; Kim, O. H.; Park, H. J.; Sung, Y. E., Alveoli-Inspired Facile Transport Structure of N-Doped Porous Carbon for Electrochemical Energy Applications. *Adv. Energy Mater.* 2015, 5, 1401309.
- [6] H. Zhang, J. Chen, Y. Li, P. Liu, Y. Wang, T. An, H. Zhao, Nitrogen-Doped Carbon Nanodots@Nanospheres as An Efficient Electrocatalyst for Oxygen Reduction Reaction, *Electrochim. Acta* 165 (2015) 7-13.
- [7] D. Guo, R. Shibuya, C. Akiba, S. Saji, T. Kondo, J. Nakamura, Active sites of nitrogen-doped carbon materials for oxygen reduction reaction clarified using model catalysts, *Science* 351 (2016) 361-365.

## Chapter 3.

### Oxygen reduction reaction (ORR) properties of the NHPCs

#### 3-1. Introduction

In Chapter 2, the NHPCs were prepared under four different experimental parameters, including species of magnesium salt precursors, carbonization temperature, urea amount and magnesium salt amount.

In this chapter, the ORR properties of the NHPCs are investigated by the rotating disk electrode (RDE) measurements in O<sub>2</sub>-saturated 0.1 M KOH electrolyte. Furthermore, to confirm the practical use of the NHPCs in a real battery, Zn-air batteries were constructed with the catalysts coated on carbon paper as the air cathode, 6 M KOH as the electrolyte and Zn foil as the anode.

As-benefited from the characteristics of hierarchical multi-porous, high specific surface area and N-doping, the optimized Mg<sub>10</sub>Ur<sub>20</sub>Cot<sub>1</sub>g-1000 shows superior electrocatalytic ORR activities, which is comparable to the commercial Pt/C catalyst.

#### 3-2. Experimental

##### 3-2-1. ORR electrochemical measurements

The electrochemical characterization of the NHPCs was performed in a conventional three-electrode system using a Princeton electrochemical analyzer, as shown in **Figure 3-1**. A platinum plate, an Ag/AgCl electrode with saturated KCl solution, and a rotating disk electrode (RDE) inserted with a polished glassy carbon disk with the diameter of 5 mm were used as the counter, reference and working electrode, respectively. The catalyst ink was prepared by mixing 2.0 mg NHPCs or commercial Pt/C (Sigma Aldrich, 20% Pt loading), 20  $\mu$ L 5% Nafion solution (Sigma-Aldrich, perfluorinated resin solution 5 wt. % in mixture of lower aliphatic alcohols and water, contains 45% water) and 400  $\mu$ L ethanol by ultrasonic agitation for at least 30 min. Then, 6  $\mu$ L catalyst ink was cast on the glassy carbon electrode and dried in air to make the working electrode. 0.1 M KOH solution was used as the electrolyte, which was saturated with Ar or O<sub>2</sub> gas for at least 30 min before each measurement. The measurements were conducted at room temperature.

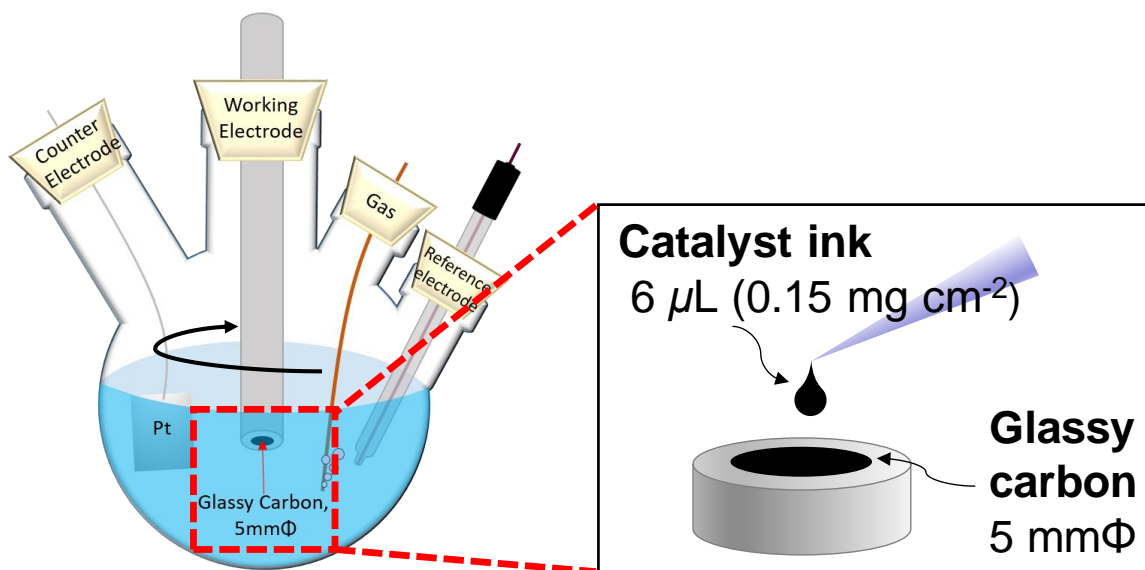


**Figure 3-1. Schematic diagram of three-electrode system of RDE measurement.**

Linear sweep voltammetry (LSV) for ORR was measured in O<sub>2</sub>-saturated electrolyte with a sweep rate of 10 mV s<sup>-1</sup> at various electrode rotation rates ranging from 400 to 1600 rpm in the potential range from 0 to 1 V vs RHE. Cyclic voltammetry (CV) was conducted in both Ar and O<sub>2</sub>-saturated electrolyte at a sweep rate of 50 mV s<sup>-1</sup> in the potential range of 0 to 1 V vs RHE. The measured potentials were converted to the reversible hydrogen electrode (RHE) via the Nernst equation:<sup>1</sup>

$$E_{RHE} = E_{Ag/AgCl} + 0.059 \text{ pH} + 0.197 \text{ V} \quad (1)$$

Equation (1) was verified by measuring the equilibrium potential of Pt in a 0.1M KOH (pH13).

The electron transfer number (*n*) per oxygen molecule involved was calculated by using Koutecky–Levich (K-L) equations:<sup>2</sup>

$$\frac{1}{j} = \frac{1}{j_L} + \frac{1}{j_K} = \frac{1}{B\omega^{1/2}} + \frac{1}{j_K} \quad (2)$$

$$B = 0.62nFC_0D_0^{2/3}\nu^{-1/6} \quad (3)$$

$$j_K = nFkC_0 \quad (4)$$

in which  $j$  is the measured current density;  $j_L$  and  $j_K$  are the diffusion-limiting and kinetic current densities ( $\text{mA cm}^{-2}$ ), respectively.  $n$  is the overall number of electrons gained per  $\text{O}_2$ ,  $C_0$  is the bulk concentration of  $\text{O}_2$  ( $1.2 \times 10^{-6} \text{ mol cm}^{-3}$ ),  $F$  is the Faraday constant ( $F = 96485 \text{ C mol}^{-1}$ ),  $D_0$  is the diffusion coefficient of  $\text{O}_2$  in 0.1 M KOH electrolyte ( $1.9 \times 10^{-5} \text{ cm}^2 \text{ s}^{-1}$ ),  $\nu$  is the kinetic viscosity of the electrolyte ( $0.01 \text{ cm}^2 \text{ s}^{-1}$ ),  $\omega$  is the angular velocity of the disk ( $\text{rad/s}$ ) ( $\omega = 2\pi N$ ,  $N$  is the linear rotation speed at rotation per second) and  $k$  is the electron transfer rate constant.<sup>2</sup>

### 3-2-2. Zn-air battery test

The primary Zn-air primary battery was constructed in a home-made electrochemical cell, as shown in **Figure 3-2**. A Toray Teflon treated carbon paper (TGP-H-090), acting as a gas diffusion layer, was uniformly coated with catalyst ink with a mass load of around  $1 \text{ mg cm}^{-2}$ , which was used as the air cathode. A 6 M KOH solution was used as the electrolyte and a Zn-foil was used as an anode. All measurements were conducted with a VersaSTAT 3 Princeton electrochemical analyzer.

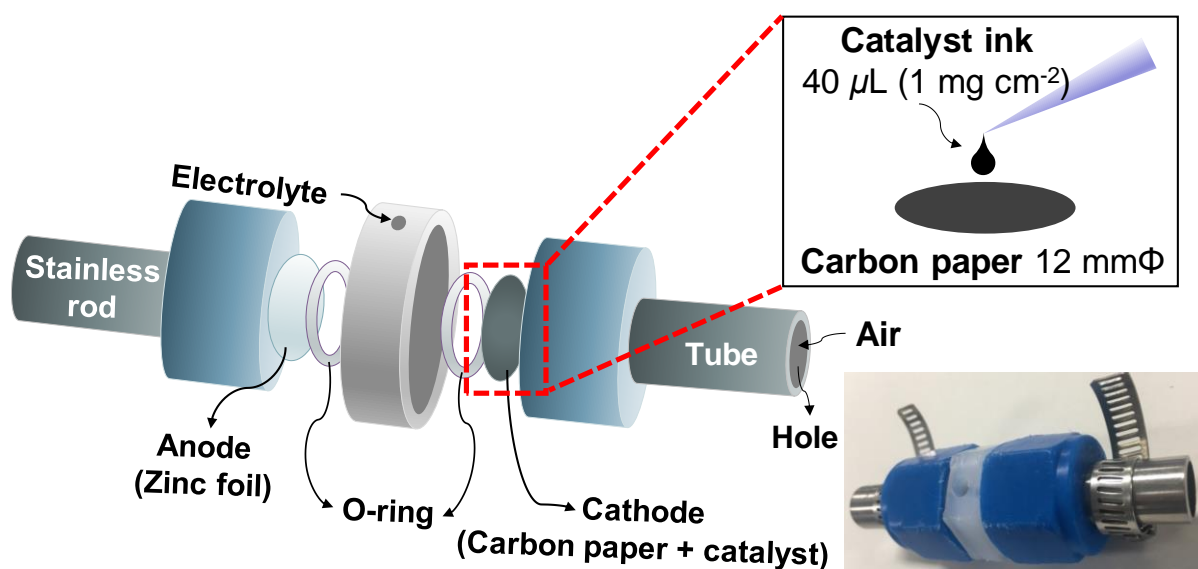


**Figure 3-2.** Schematic diagram of the two-electrode system for Zn-air battery

### 3-3. Results and discussion

#### 3-3-1. CV measurements

The electrocatalytic activities of the as-prepared the NHPCs were investigated using an RDE setup in 0.1 M KOH electrolyte. CV measurements on the porous carbon electrode were conducted in both Ar and O<sub>2</sub>-saturated electrolyte, as shown in **Figure 3-3**.

In Ar-saturated solution, no redox features were observed for all electrodes. However, in the O<sub>2</sub>-saturated electrolyte, significant cathodic ORR peaks between 0.6 to 0.9 V vs. RHE are observed, implying the electrocatalytic activity of the NHPCs for ORR. Moreover, sample Mg10Ur20Cot1g-1000 exhibits the most well-defined cathodic curve and the most positive cathodic peak potential (0.76 V), indicating a good ORR performance for such an electrode.

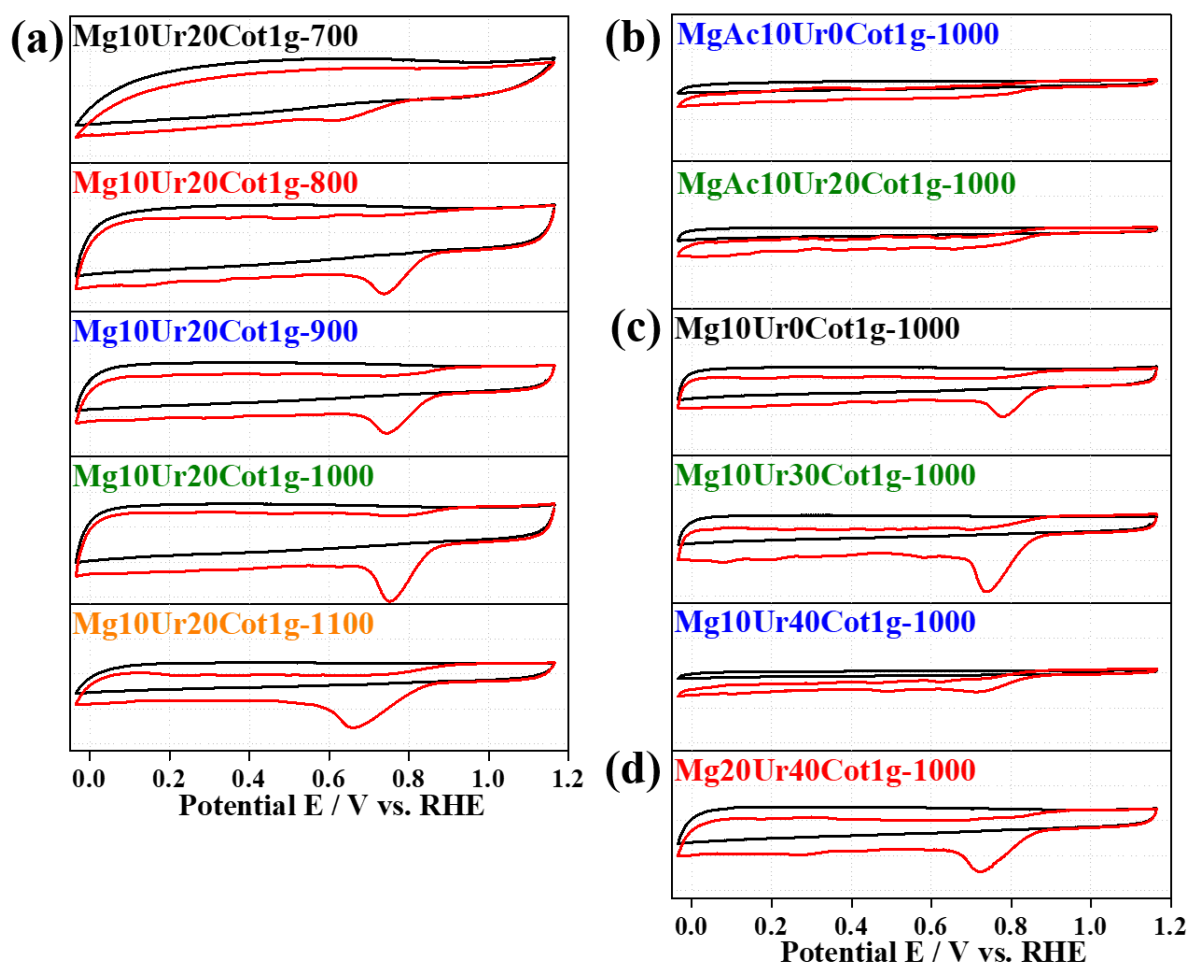


**Figure 3-3.** CV curves of the NHPCs under both Ar and O<sub>2</sub>-saturated electrolyte. (a) Carbonization temperature effect, (b) Species of magnesium salt effect, (c) Urea amount effect, and (d) Magnesium salt amount effect.

### 3-3-2. ORR activity measurement by RDE at various rotating speeds and K-L plots

To further investigate the ORR reaction kinetics, RDE measurements were conducted at different rotating speeds. **Figure 3-4** to **Figure 3-7** show the typical LSV curves for all samples at rotation speeds from 400 to 1600 rpm. The corresponding K-L plots reveal good linearity as shown in **Figure 3-8** to **Figure 3-11**, suggesting first-order reaction kinetics of the ORR as a function of dissolved oxygen levels.

The estimated numbers of the transferred electrons ( $n$ ) per oxygen molecule in the potential range of 0.3–0.6 V are plotted in **Figure 3-12**. It is observed that for the hierarchical porous carbon with N-doping and high specific surface area, including Mg10Ur20Cot1g-800, Mg10Ur20Cot1g-900, Mg10Ur20Cot1g-1000, Mg10Ur20Cot1g-1100, Mg10Ur30Cot1g-1000, and Mg20Ur40Cot1g-1000, the corresponding electrodes present  $n$  values varying from 3.5 to  $\sim$ 4.0, which is approaching the ideal four electron transfer pathway. Sample Mg10Ur20Cot1g-700 presents transfer numbers slightly higher than 4, which might be caused by the unexpected side reactions since the carbon is not well-graphitized at a low carbonization temperature. In contrast, samples Mg10Ur0Cot1g-1000, Mg10Ur40Cot1g-1000, MgAc10Ur0Cot1g-1000 and MgAc10Ur20Cot1g-1000 present low values of transfer numbers between  $\sim$ 2.5 and 3. The low selectivity toward the direct four-electron transfer reaction for these four samples is due to their lack of N-doping or non-hierarchical porous structure with a low specific surface area.

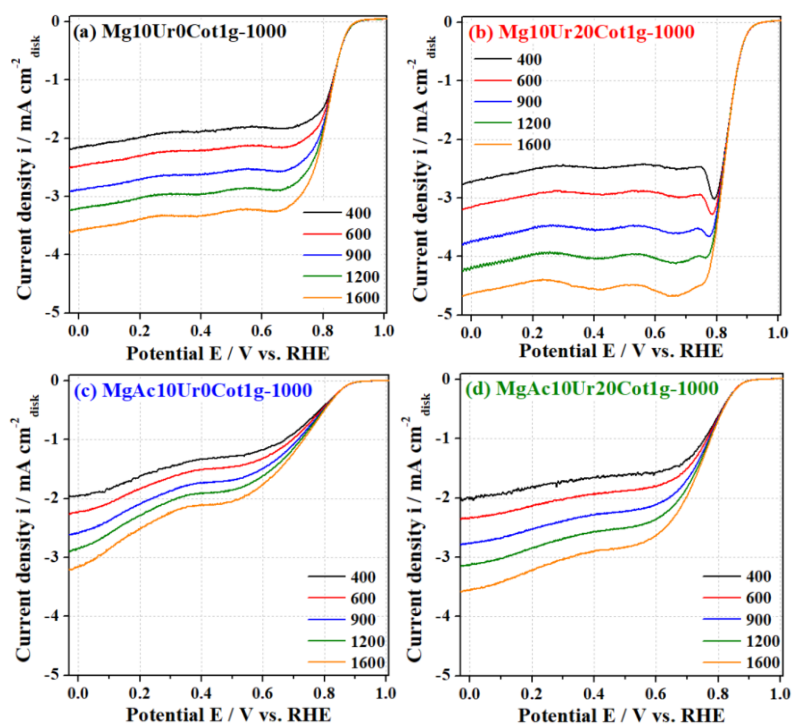


**Figure 3-4.** LSV curves at various rotation speeds for the NHPCs with different species of magnesium salt.

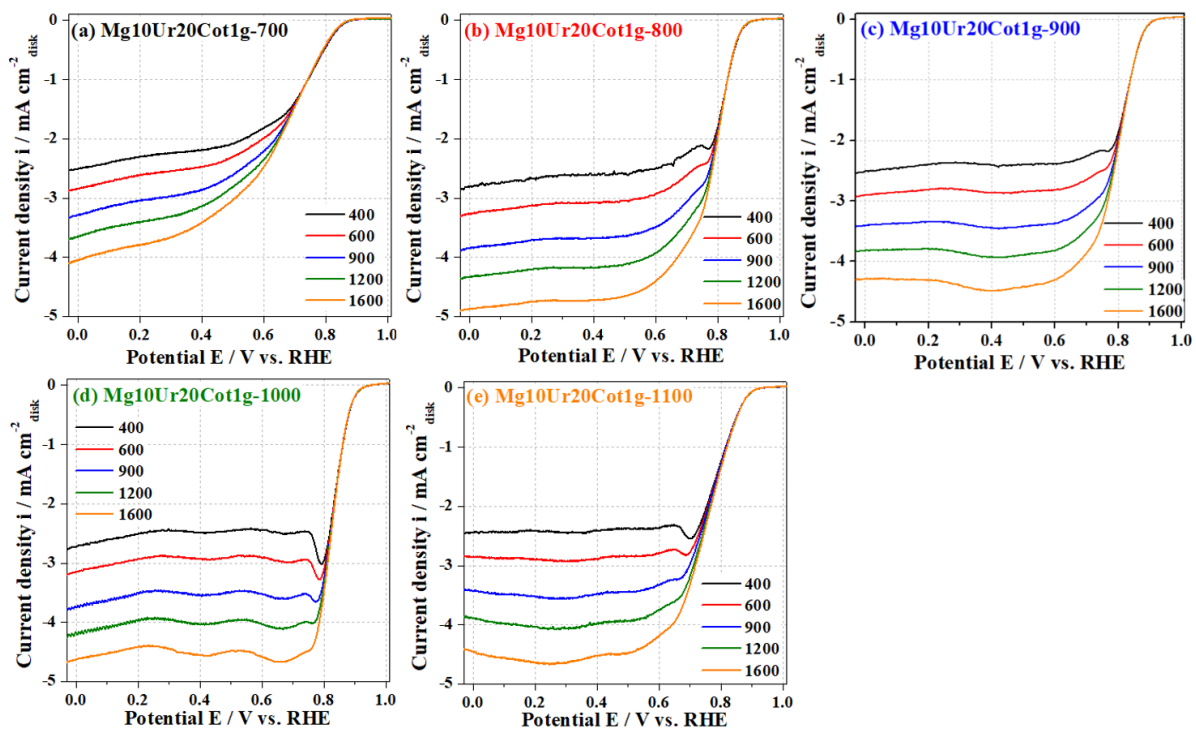


Figure 3-5. LSV curves at various rotation speeds for the NHPCs with different carbonization temperatures.

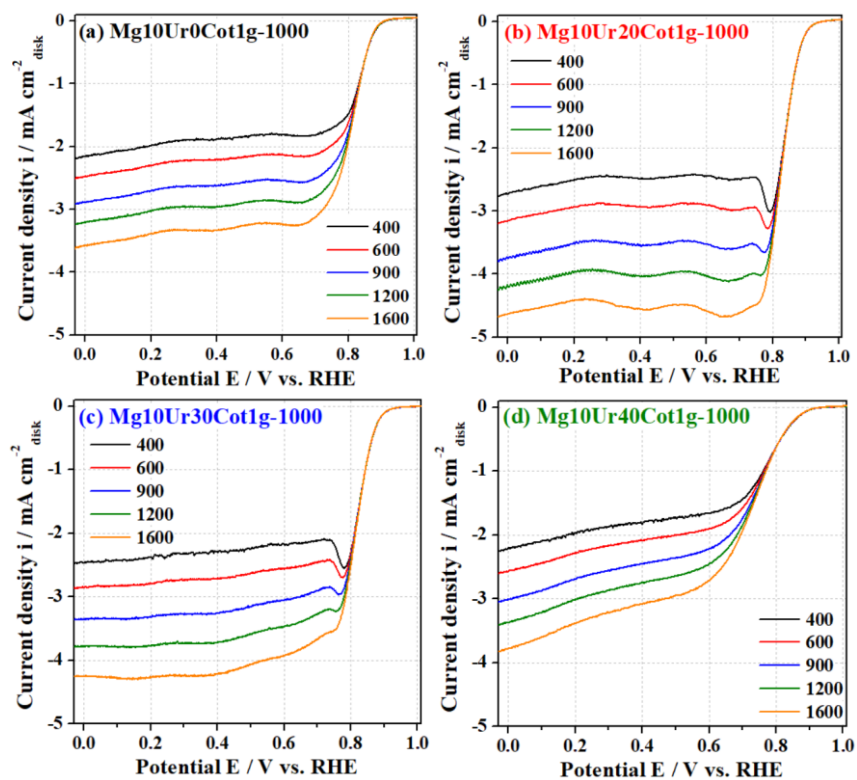


Figure 3-6. LSV curves at various rotation speeds for the NHPCs with different urea amounts.

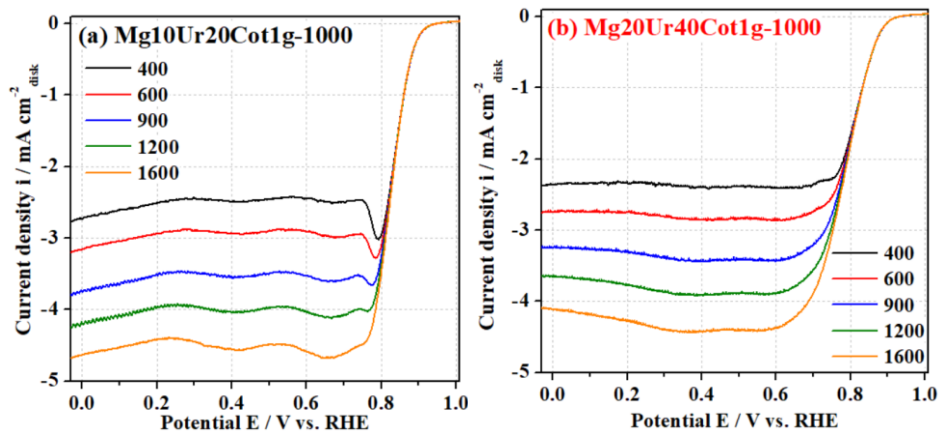


Figure 3-7. LSV curves at various rotation speeds for the NHPCs with different magnesium salt amounts.

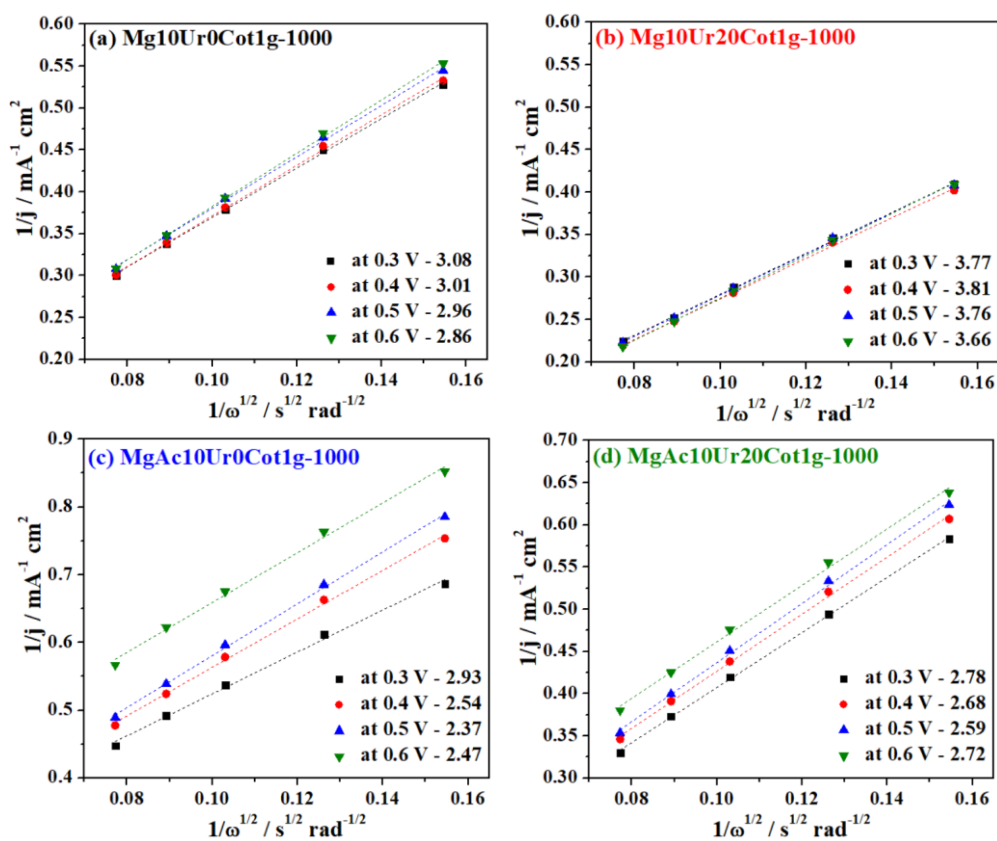


Figure 3-8. K-L plots and calculated electron transfer number of the NHPCs with different species of magnesium salt.

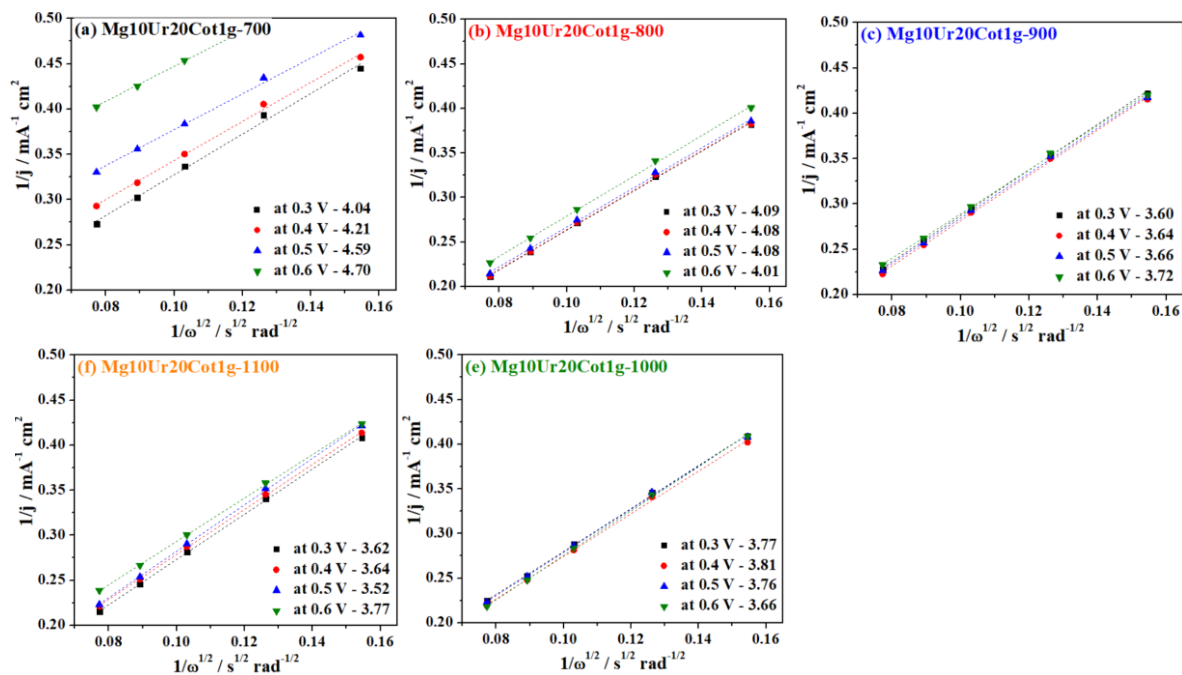


Figure 3-9. K-L plots and calculated electron transfer number of the NHPCs with different carbonization temperatures.

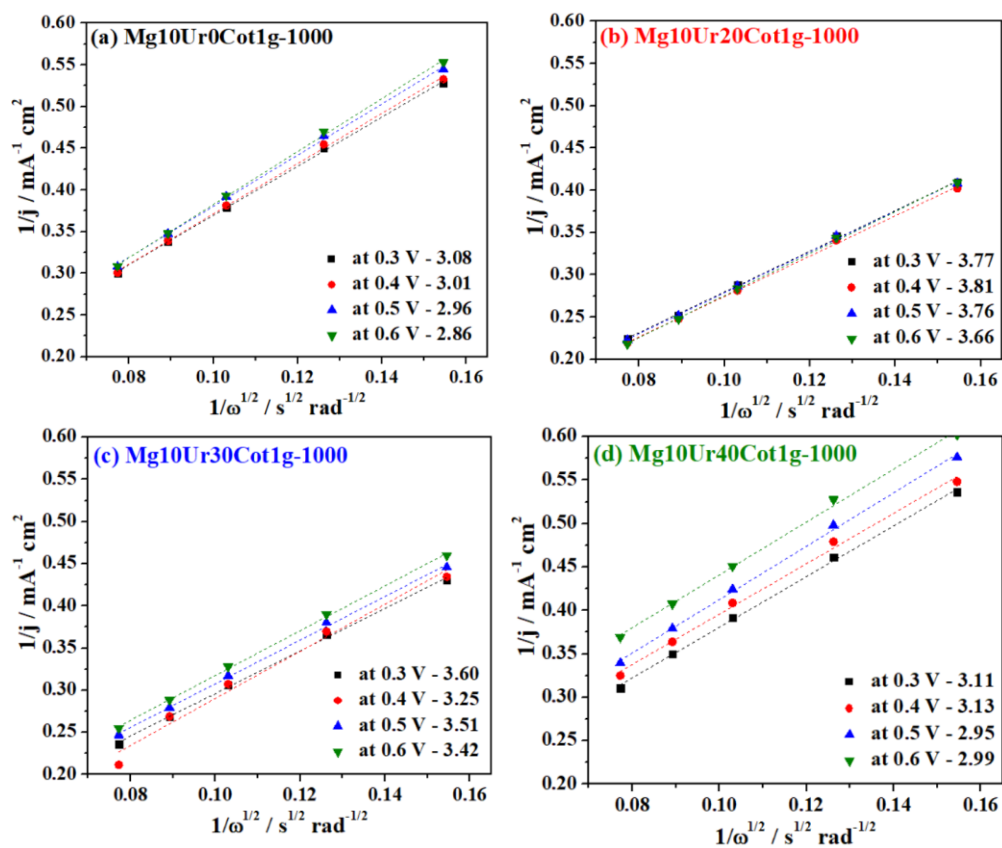


Figure 3-10. K-L plots and calculated electron transfer number of the NHPCs with different urea amounts.

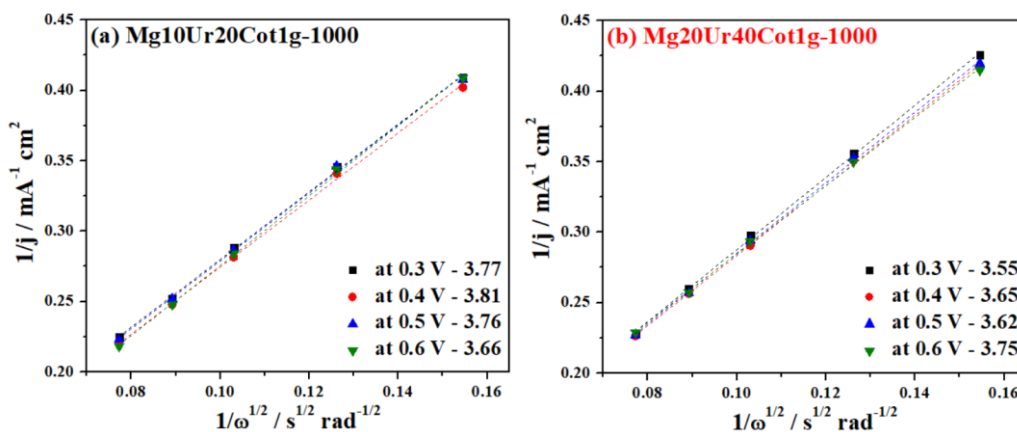


Figure 3-11. K-L plots and calculated electron transfer number of the NHPCs with different magnesium salt amounts.

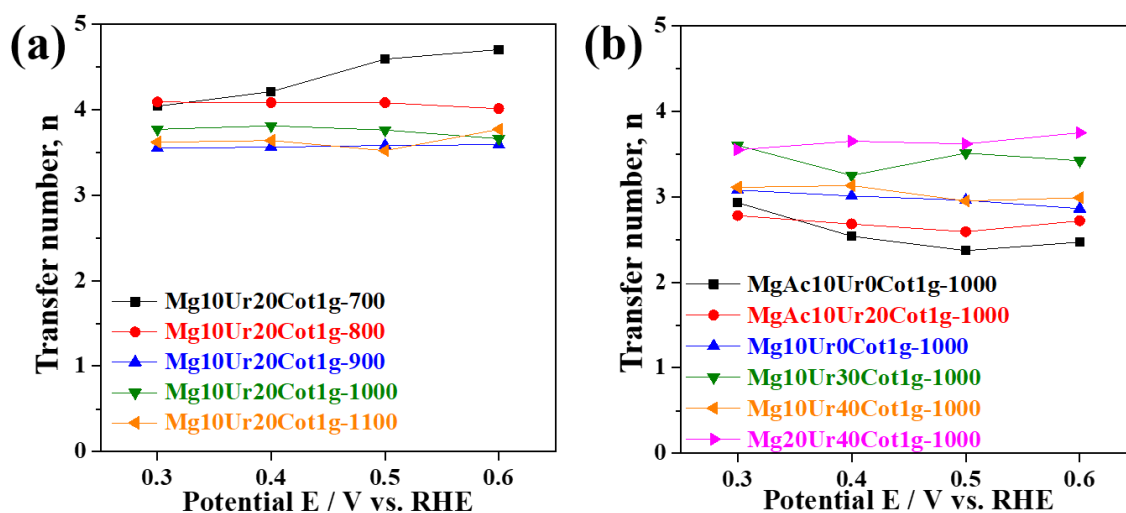


Figure 3-12. The calculated electron transfer number,  $n$ , based on K-L plots.

### 3-3-3. ORR activity comparison

The ORR performance for all electrodes is compared in their LSV curves at a rotating speed of 1600 rpm, as shown in **Figure 3-13**. The ORR activities are discussed in terms of experimental parameters including (a) species of magnesium salt, (b) carbonization temperature, (c) urea amount, and (d) magnesium salt amount.

**Figure 3-13** (a) shows the comparison of the samples using different magnesium salt precursors. It is obvious that the nitrate-derived samples present greatly enhanced ORR activity than that of the acetate-derived samples. This is because of the formation of highly hierarchical porous structure and high specific surface area when magnesium nitrate is used in the raw material, which has been discussed in detail in Chapter 2. It is also observed that when urea is not added in the raw material, the

corresponding carbon products illustrate poorer activity, representing the importance of urea in the doping of N element.

For the samples prepared with different carbonization temperatures as shown in **Figure 3-13** (b), it is observed that sample Mg10Ur20Cot1g-1000 illustrates the best ORR activities, including highest onset potential (0.94 V) and half-wave potential (0.83 V). Carbonization temperature is a very important parameter for preparing N-doped carbon with high ORR performance, which could greatly influence the doping amount of N, the doping species of N, and the graphitization degree of carbon. The results here indicate that an optimized carbonization temperature is 1000 °C in our experimental system, which is also frequently used by other research groups.<sup>3-6</sup>

The amount of urea as-added in the raw material is also optimized, as shown in **Figure 3-13** (c). Urea20 is an optimal amount, and when the excess amount of urea is added, the corresponding carbon shows decreased specific surface area, thereby a decreased ORR activity is obtained.

Magnesium salt amount is also very important, and when the excess amount of magnesium nitrate is introduced in the precursor, the corresponding carbon also shows decreased specific surface area, hence a poorer ORR activity is obtained, as shown in **Figure 3-13** (d).

In summary, sample Mg10Ur20Cot1g-1000 presents the best ORR activities, which are even similar to that of commercial Pt/C, as shown in **Figure 3-13** (d). The summary of the ORR properties, including onset potential, half-wave potential and limiting current density are shown in **Table 3-1**.

**Table 3-1. Summary of the ORR activities.**

| <i>Samples</i>              | <b>Onset potential<br/>(<math>E_{\text{onset}} / \text{V}</math><br/>vs RHE)</b> | <b>Half-wave potential<br/>(<math>E_{1/2} / \text{V}</math> vs<br/>RHE)</b> | <b>Current density<br/>at 0.7 V<br/>(<math>I_{0.7} / \text{mA cm}^{-2}</math>)</b> | <b>Limiting current<br/>density at 0.2 V<br/>(<math>I_{\text{Lim}} / \text{mA cm}^{-2}</math>)</b> |
|-----------------------------|--|---|--|--|
| Mg10Ur20Cot1g-700           | 0.87   | 0.65  | -1.47  | -3.79  |
| Mg10Ur20Cot1g-800           | 0.91   | 0.79  | -3.76  | -4.75  |
| Mg10Ur20Cot1g-900           | 0.92   | 0.80  | -3.86  | -4.03  |
| Mg10Ur20Cot1g-1000          | 0.94   | 0.83  | -4.61  | -4.42  |
| Mg10Ur20Cot1g-1100          | 0.92   | 0.77  | -3.29  | -4.64  |
| <i>MgAc10Ur0Cot1g-1000</i>  | <i>0.86</i>  | <i>0.64</i>   | <i>-1.21</i>   | <i>-2.50</i>   |
| <i>MgAc10Ur20Cot1g-1000</i> | <i>0.87</i>  | <i>0.72</i>   | <i>-1.96</i>   | <i>-3.22</i>   |
| Mg10Ur0Cot1g-1000           | 0.90   | 0.81  | -3.11  | -3.38  |
| Mg10Ur30Cot1g-1000          | 0.92   | 0.83  | -3.66  | -4.27  |
| Mg10Ur40Cot1g-1000          | 0.88   | 0.70  | -1.91  | -3.38  |
| <i>Mg20Ur40Cot1g-1000</i>   | <i>0.92</i>  | <i>0.79</i>   | <i>-3.87</i>   | <i>-4.25</i>   |

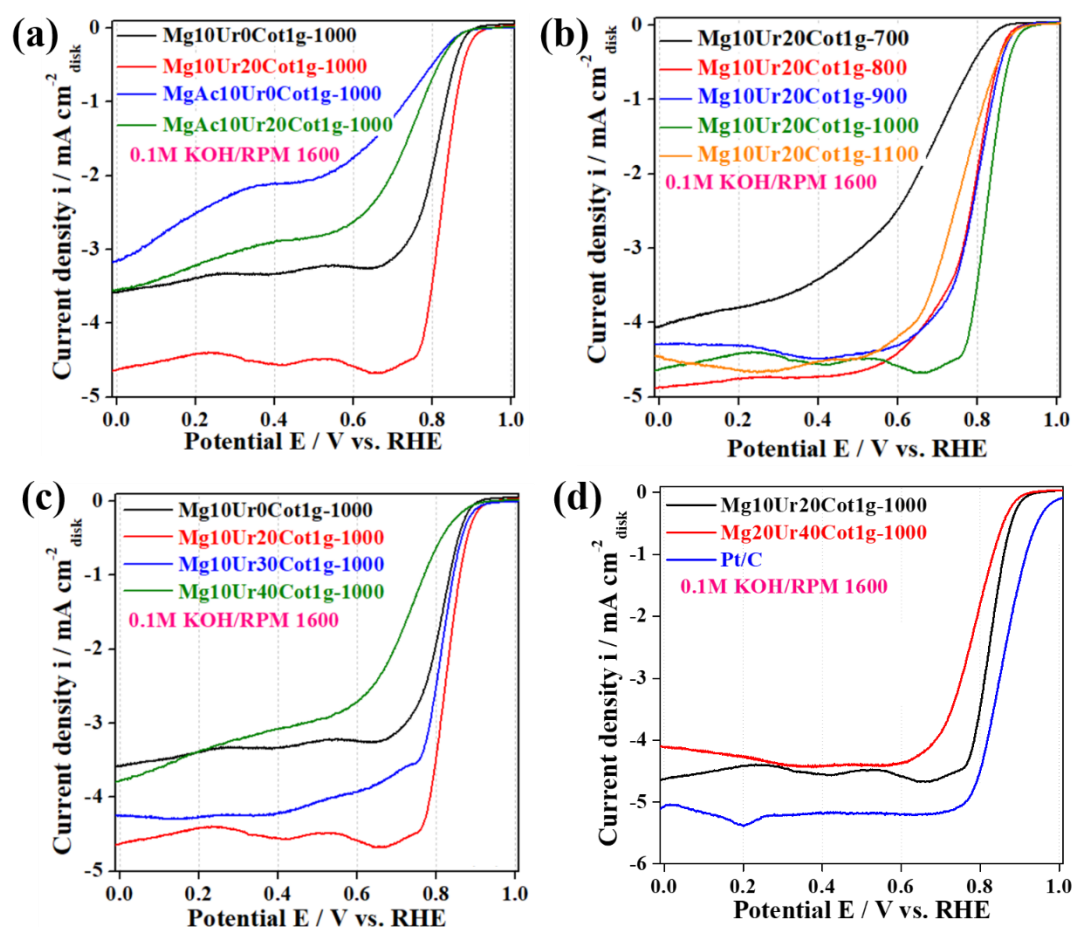


**Figure 3-13.** The comparison of the ORR activity using LSV curves at 1600 rpm for the samples prepared under different parameters: (a) Species of magnesium salt, (b) Carbonization temperature, (c) Urea amount, and (d) Magnesium salt amount. The comparison with commercial Pt/C is also shown in (d), respectively.

### 3-3-4. Chronoamperometric measurement

Besides the good electrocatalytic activity, the NHPC also exhibits high durability superior to Pt/C catalyst evaluated by chronoamperometric examination, which is shown in **Figure 3-14** (a). The measurement was conducted at -0.4 V vs. Ag/AgCl in O<sub>2</sub>-saturated KOH solution at a rotation speed of 1600 rpm. The NHPC electrode (Mg10Ur20Cot1g-1000) can retain ~88% of its original current density after 10 h holding. However, commercial Pt/C loses ~17% of its original current density in the same condition. Moreover, it is well known that the possible crossover of methanol from the anode to the cathode in fuel cells causes the poisoning of the Pt catalyst in the cathode. Therefore, the durability of catalysts against possible methanol crossover is another important issue for the practical application.

Methanol tolerance was evaluated by the chronoamperometric measurement at -0.4 V vs. Ag/AgCl in O<sub>2</sub>-saturated KOH solution as shown in **Figure 3-14** (b), in which 2 vol.% methanol was added in

the electrolyte. The ORR current does not change after methanol addition for the NHPC electrode, while a significantly decreased current shift is observed immediately after methanol addition for the Pt/C electrode. The results indicate that the NHPCs have a superior methanol tolerance property, making it a promising cathodic catalyst for alkaline direct methanol fuel cells.

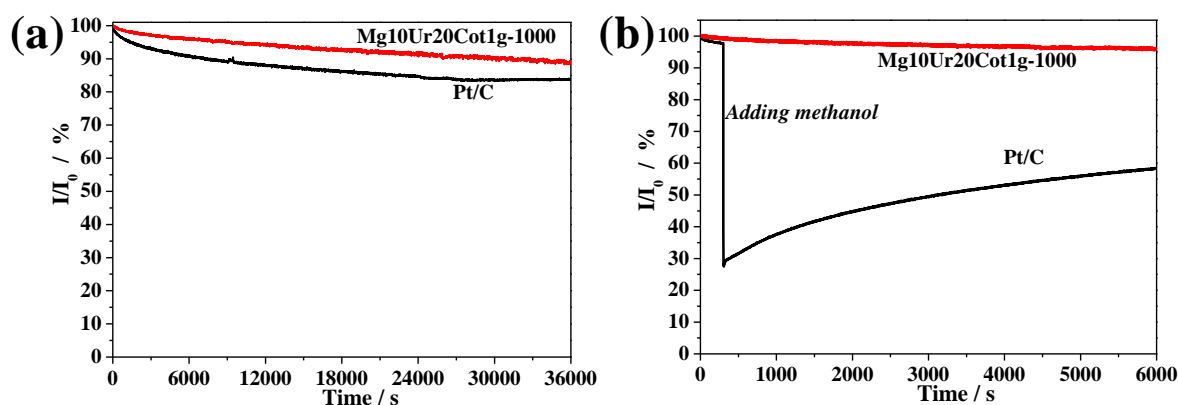


**Figure 3-14.** Electrochemical measurement using the chronoamperometric method. (a) Chronoamperometric responses of the NHPC and Pt/C on glassy carbon electrodes kept at 0.4 V vs Ag/AgCl in  $O_2$ -saturated 0.1 M KOH electrolyte; (b) Chronoamperometric responses of the NHPC and Pt/C electrodes with the addition of methanol at 300 s.

### 3-3-5. Summary about the influence of the four preparation parameters to electrochemical properties

In summary, the influence of four preparation parameters, including species of magnesium salt precursors, carbonization temperature, added urea amount and magnesium salt amount, on the porous properties and electrochemical performance of the NHPCs were comprehensively investigated. Following conclusions can be obtained for each parameter.

(1) For the comparison of the effect of species of magnesium salt precursors, magnesium nitrate and magnesium acetate were used. It was confirmed that the use of nitrate introduced the exothermic reactions, which could exfoliate the cellulose fibers to highly porous architecture, making a high-active ORR catalyst. However, the magnesium acetate-induced samples showed the endothermic reaction and still had the bulky fiber shape, limited specific surface area and less porous structure of final carbon, making a low-active ORR catalyst.

(2) The carbonization temperature was optimized, which could greatly influence the doping amount of N, the doping species of N and the graphitization degree of carbon, and it was concluded the NHPC prepared at 1000 °C showed the best electrochemical performance.

(3) The importance of urea addition in the raw materials was obvious, since it offered the doping source for N element and promoted the complete exfoliation of cellulose fibers; however, excess addition of urea in the raw materials would decrease the specific surface area of the final carbon, making a low-active ORR catalyst due to low-active site.

(4) MgO template was important for the creation of micro and mesopores, therefore, the added MgO amount was optimized and it is found that excess amount of MgO template could decrease the specific surface area of final carbon, making a low-active ORR catalyst.

After the discussion of the above four parameters, the optimized the NHPC with highest ORR performance is Mg10Ur20Cot1g-1000.

The superior electrochemical ORR performance of the Mg10Ur20Cot1g-1000 can be explained by its novel hierarchical porous structure with N-doping and high specific surface area. Firstly, the abundant graphitic and pyridinic N-doped carbon offers a large amount of N-C active sites. At the same time, the high specific surface area and hierarchical open pore structure can enhance the penetrability of electrolytes into the interior surfaces, which can increase the number of exposed active sites, provide efficient electrolyte/mass contact and facilitate fast ion transportation. These characteristics of the NHPCs greatly contribute to the enhancement of the electrocatalytic activities. Finally, the electrocatalytic performance of the NHPCs is also comparable to the best reported carbon-based ORR catalysts,<sup>7-9</sup> making it a promising substitute to commercial Pt/C.

### 3-3-6. Zn-air battery test

Finally, to confirm the practical use of the NHPCs in a real battery, we constructed primary Zn-air batteries with the catalysts on carbon paper as the air cathode, 6 M KOH as the electrolyte and Zn foil as the anode. It is noted that all cells have an active area of 0.785 cm<sup>2</sup>. **Figure 3-15** (a) presents the polarization and power density curves for the Zn-air batteries catalyzed with Mg10Ur0Cot1g-1000, Mg10Ur20Cot1g-1000, and Pt/C. Mg10Ur20Cot1g-1000 shows a peak power density of 57 mW cm<sup>-2</sup> at 82 mA cm<sup>-2</sup>, which is greatly superior to the Mg10Ur0Cot1g-1000 electrode (20 mW cm<sup>-2</sup> at 37 mA cm<sup>-2</sup>) and close to the Pt/C catalyst (50 mW cm<sup>-2</sup> at 70 mA cm<sup>-2</sup>). The galvanostatic discharge measurement, as shown in **Figure 3-15** (b), indicates that the Mg10Ur20Cot1g-1000 electrode presents potential platform at 1.24, 1.19, 1.15, 1.07, and 0.66 V at the discharge current of 1, 5, 10, 20 and 50 mA, respectively. These plateau potentials are similar to that for Pt/C catalyst, but superior to that of sample Mg10Ur0Cot1g-1000, illustrating the corresponding plateau potentials of 1.22, 1.15, 1.02, 0.75, and 0.22 V, respectively. All of these results indicate that the NHPC prepared under optimized conditions is suitable for ORR catalyst with high activity and durability.

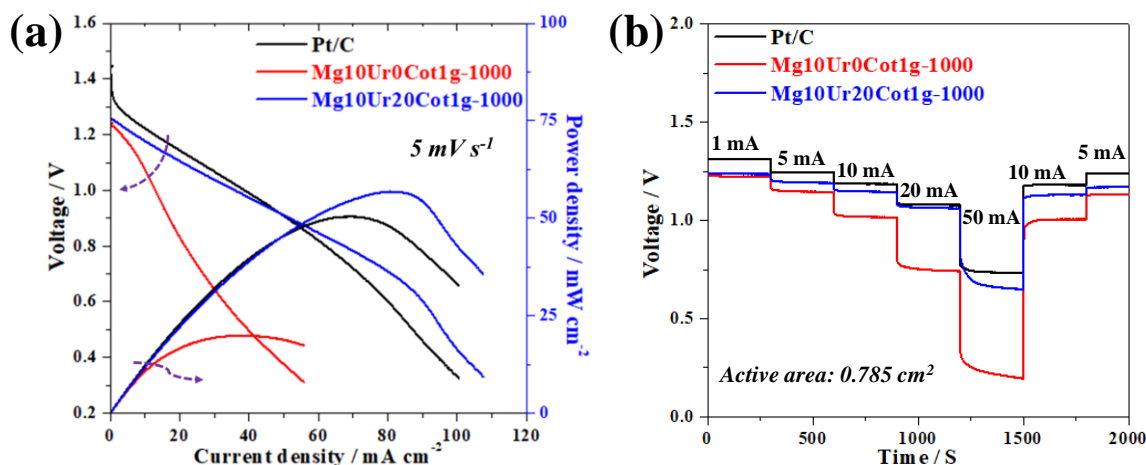


**Figure 3-15.** Electrochemical measurement using Zn-air full cell. (a) Polarization and power density curves of the primary Zn-air batteries with Mg10Ur0Cot1g-1000, Mg10Ur20Cot1g-1000, and Pt/C catalysts; (b) Discharge curves of the Zn-air batteries at various current densities.

### 3-4. Conclusions

In this chapter, ORR activity of NHPCs in KOH electrolyte is comprehensively investigated, and following conclusions are drawn:

(1) Compared with N-doped carbon, with low specific surface area and pore volume, derived from magnesium acetate precursor, NHPCs derived from magnesium nitrate precursor exhibits very high ORR activity, owing to high specific surface area and N-doping.

(2) Although N content decreases with an increase in the carbonization temperature, the ORR activity increases with the temperature up to 1000°C. Such an activity enhancement may be associated with increased graphitization degree of carbon that enhances the conductivity. The NHPCs prepared at 1000°C showed the best ORR performance.

(3) Even N-free hierarchically porous carbon exhibits relatively high ORR activity, but the electron transfer number is lower than that of NHPC. The carbon with high surface area with hierarchical pore structure is one of the way to increase the ORR activity, but heteroatom doping is necessary to promote four-electron reduction of oxygen.

(4) From the examination of four experimental parameters of magnesium salt precursor, carbonization temperature, urea content and the amount of magnesium salt, the optimized NHPCs with the highest ORR performance is Mg10Ur20Cot1g-1000, which is beneficial from its hierarchical porous structure, optimized N-doping and high specific surface area ( $1173 \text{ m}^2 \text{ g}^{-1}$ ). The ORR performance of NHPCs is also comparable to the best reported carbon-based ORR catalysts in alkaline electrolyte, making it a promising substitute for commercial Pt/C.

### 3-5. Reference

- [1] O. Diaz-Morales, D. Ferrus-Suspedra, M.T.M. Koper, The importance of nickel oxyhydroxide deprotonation on its activity towards electrochemical water oxidation, *Chem. Sci.* 7 (2016) 2639–2645.
- [2] Y. Zhan, F. Xie, H. Zhang, Z. Lin, J. Huang, W. Zhang, X. Sun, Y. Zhang, J. Chen, H. Meng, Non Noble Metal Catalyst for Oxygen Reduction Reaction and Its Characterization by Simulated Fuel Cell Test, *J. Electrochem. Soc.* 165 (2018) J3008–J3015.
- [3] X. Wu, X. Yu, Z. Lin, J. Huang, L. Cao, B. Zhang, Y. Zhan, H. Meng, Y. Zhu, Y. Zhang, Nitrogen doped graphitic carbon ribbons from cellulose as non noble metal catalyst for oxygen reduction reaction, *Int. J. Hydrogen Energy* 41 (2016) 14111-14122.
- [4] J. Zhang, Z. Zhao, Z. Xia, L. Dai, A metal-free bifunctional electrocatalyst for oxygen reduction and oxygen evolution reactions, *Nat. Nanotechnol.* 10 (2015) 444.
- [5] W. Yuan, Y. Feng, A. Xie, X. Zhang, F. Huang, S. Li, X. Zhang, Y. Shen, Nitrogen-doped nanoporous carbon derived from waste pomelo peel as a metal-free electrocatalyst for the oxygen reduction reaction, *Nanoscale* 8 (2016) 8704-8711.
- [6] M. Wang, X. Lei, L. Hu, P. Zhang, H. Hu, J. Fang, High-performance Waste Biomass-derived Microporous Carbon Electrocatalyst with a Towel-like Surface for Alkaline Metal/air batteries, *Electrochim. Acta* 250 (2017) 384-392.
- [7] C. Hu, L. Dai, Multifunctional Carbon-Based Metal-Free Electrocatalysts for Simultaneous Oxygen Reduction, Oxygen Evolution, and Hydrogen Evolution, *Adv. Mater.* 29 (2017) 1604942.
- [8] K. Wan, A.D. Tan, Z.P. Yu, Z.X. Liang, J.H. Piao, P. Tsiakaras, 2D nitrogen-doped hierarchically porous carbon: Key role of low dimensional structure in favoring electrocatalysis and mass transfer for oxygen reduction reaction, *Appl. Catal. B* 209 (2017) 447-454.
- [9] B. Men, Y. Sun, J. Liu, Y. Tang, Y. Chen, P. Wan, J. Pan, Synergistically Enhanced Electrocatalytic Activity of Sandwich-like N-Doped Graphene/Carbon Nanosheets Decorated by Fe and S for Oxygen Reduction Reaction, *ACS Appl. Mater. Interfaces* 8 (2016) 19533-19541.

## Chapter 4.

### Preparation of the NHPCs with a tunable pore structure and high specific surface area

#### 4-1. Introduction

In chapter 2, the NHPCs were prepared by the exothermic pyrolysis of magnesium nitrate-carbohydrates (urea and cellulose). The NHPCs have a high specific surface area more than  $1000 \text{ m}^2 \text{ g}^{-1}$  and a hierarchically porous structure with micro-, meso-, and macropores. Chapter 3 demonstrates that the NHPCs thus prepared have high potential for highly active and durable metal-free ORR electrocatalysts for an-air battery application.

The NHPCs are also of great interest as electrode materials for supercapacitors because the NHPCs have high specific surface areas that contribute to the capacitance increase and the nitrogen doping is known to enhance further the capacitance. However, for the capacitor applications, the specific surface area of the NHPCs has still limited; The specific capacitance must be increased to  $> 2000 \text{ m}^2 \text{ g}^{-1}$ . Understanding of the influence of pore size distribution on the supercapacitor performance is also of fundamental interest.

In this chapter, the NHPCs with a tunable pore structure and very high specific surface area more than  $2000 \text{ m}^2 \text{ g}^{-1}$  were prepared by the exothermic pyrolysis of magnesium/potassium-carbohydrate (urea and cellulose) with subsequent carbonization treatment and acid washing. The general synthesis process of the NHPCs with a tunable pore structure is the same as before mentioned it in chapter 2. The pore size distribution of NHPCs was controlled by metal composite templates with a different ratio of magnesium nitrate and potassium nitrate in precursors. After removing the template, more micro- and mesopores were created and the NHPCs showed the different pore size distribution. In this manner, the NHPCs with a tunable pore structure interconnected micro-, meso-, and macropores with very high specific surface area larger than  $2700 \text{ m}^2 \text{ g}^{-1}$  and heteroatom N-doping are produced.

#### 4-2. Experimental

##### 4-2-1. General synthetic process of the NHPCs with a tunable pore structure

The NHPCs with a tunable pore structure were synthesized by the exothermic pyrolysis of magnesium/potassium nitrate-carbohydrates (Urea and cellulose) with subsequent carbonization treatment and acid washing. **Figure 4-1** presents the schematic diagram for the preparation of the

NHPCs with a tunable pore structure. The general synthesis process of the NHPCs with a tunable pore structure is the same as that in chapter 2. However, to obtain the NHPCs with different pore size distribution, the precursors were prepared by different ratio of magnesium and potassium nitrate. The more details of pore formation mechanism will be discussed in section 4-3-5. The different ration of metal (Mg or Mg•K or K) nitrates and urea were dissolved in water, which were then impregnated into the cotton cellulose and dried. The dried nitrate-urea-cellulose precursors were heated under Ar flow for pyrolysis and carbonization. After carbonization, the samples were washed to remove the potassium and magnesium compounds and the final porous carbon products were obtained.

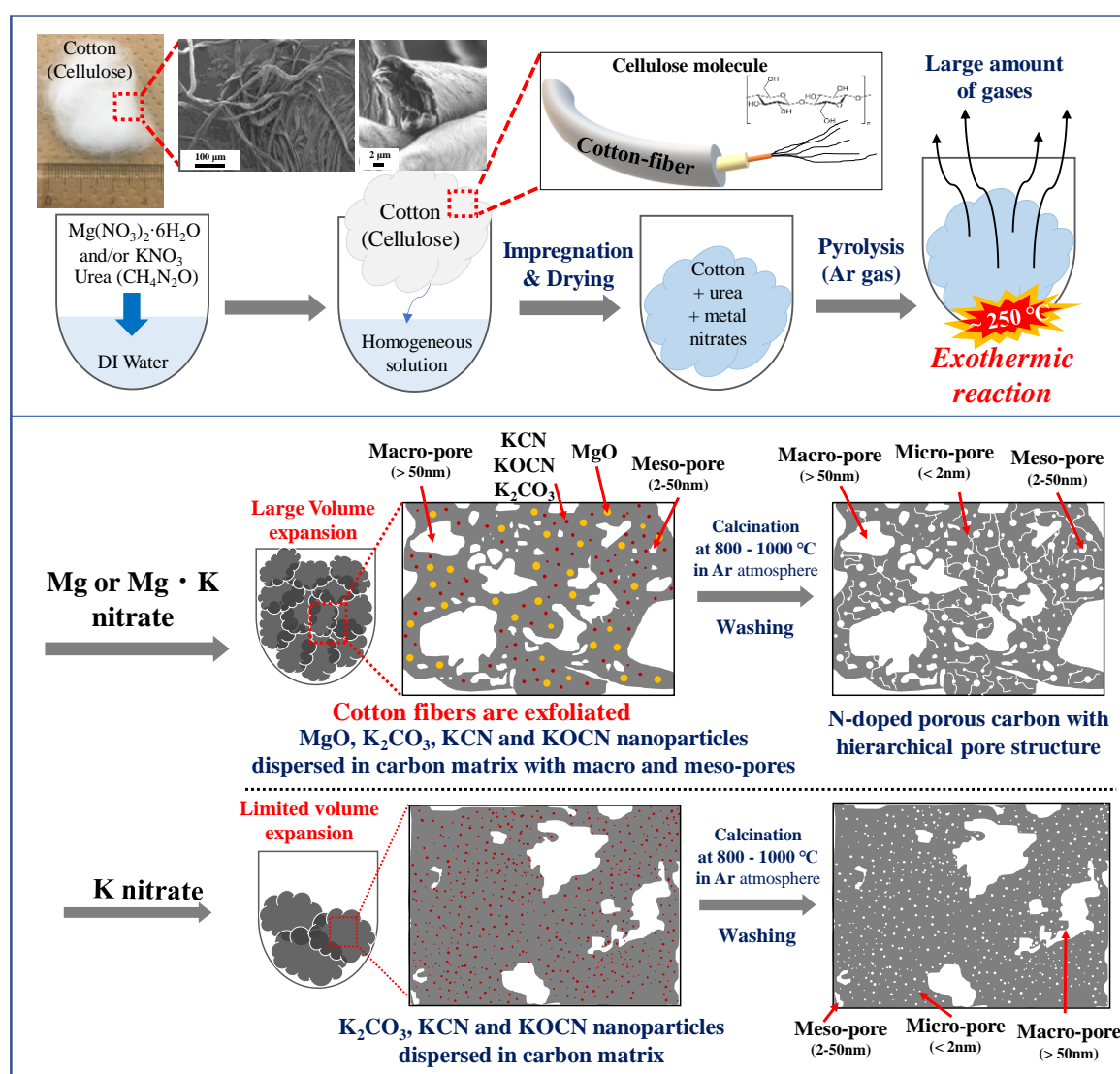


Figure 4-1. Schematic diagram for the preparation of the NHPCs with a tunable pore structure.

#### 4-2-2. Preparation of the NHPCs with a tunable pore structure

In the experiment of magnesium nitrate precursor, 10 mmol magnesium nitrate hexahydrate ( $\text{Mg}(\text{NO}_3)_2 \cdot 6\text{H}_2\text{O}$ ) and 20 mmol urea ( $\text{CH}_4\text{N}_2\text{O}$ ) were dissolved in 5 mL ultrapure Milli-Q water to form a homogeneous solution. The above solution was impregnated with 1 g commercially available absorbent cotton cellulose. After that, the wet cotton absorbed with the above solution was dried at 60 °C. The dried sample was then heated to 500°C for pre-pyrolysis at a heating rate of 10 K min<sup>-1</sup> under Ar flow in a vertical tubular reactor. Subsequently, the pyrolyzed sample was roughly pulverized using a mortar and pestle, after which the sample was carbonized at 900°C in Ar flow for 3 h. It is noted that the pre-pyrolysis and high-temperature carbonization processes can be combined in one step by heating the precursors directly to high temperatures.

We separated the treatment into two processes due to the following two reasons: (1) the maintenance of our high-temperature furnace to avoid the pollution during pyrolysis with large amount of gas emission; (2) the observation of the changes of compositions for samples after pyrolysis in order to investigate the pore formation mechanism of the final carbon.

The carbonized sample was further washed with 0.5 M HCl aqueous solution, ultrapure water, and ethanol for several times, and finally dried for use. This sample was named as *Mg10Ur20Cot1g-900* based on the magnesium nitrate amount, urea amount and carbonization temperature.

A certain amount of potassium nitrate ( $\text{KNO}_3$ ), obtained from Kanto chemical, was used to substitute magnesium nitrate, in which the samples were prepared in the same manner except for the difference in nitrate precursors. The amount of  $\text{NO}_3^-$  was kept the same for all samples, therefore another two samples with the same carbonization temperature of 900°C were prepared. One sample was prepared with 9 mmol magnesium nitrate and 2 mmol potassium nitrate which was referred as *Mg9K2Ur20Cot1g-900*, while another sample was prepared with 8 mmol magnesium nitrate and 4 mmol potassium nitrate which was named as *Mg8K4Ur20Cot1g-900*. To evaluate the influence of carbonization temperature, another two samples with a heat treatment temperature of 800 and 1000°C were also produced, which were referred to as *Mg8K4Ur20Cot1g-800* and *Mg8K4Ur20Cot1g-1000*, respectively. When potassium nitrate was also added in the precursors, the corresponding carbonized samples were firstly washed with ultrapure water to remove the potassium species, after which the samples were washed with HCl solution, water, and ethanol for several times.

Finally, another sample with the use of only potassium nitrate was also prepared. Here, 10 mmol potassium nitrate, 20 mmol urea and 1 g cotton cellulose with a carbonization temperature of 900°C were used, and the sample was named as *K10Ur20Cot1g-900*.

Totally, six samples were produced, including Mg10Ur20Cot1g-900, Mg9K2Ur20Cot1g-900, Mg8K4Ur20Cot1g-900, Mg8K4Ur20Cot1g-800, Mg8K4Ur20Cot1g-1000, and K10Ur20Cot1g-900.

#### 4-2-3. Material characterizations

The phase compositions of the samples were characterized by X-ray diffraction (XRD, Rigaku Miniflex with Cu K $\alpha$  radiation). The morphology of the samples was observed by transmission electron microscopy (TEM, 200 kV, JEOL, JEM-2010F) and scanning electron microscopy (SEM, JEOL, JSM-7400F). The bonding features of the samples were analyzed by an X-ray photoelectron spectroscopy (XPS, JEOL, JPS-9200) system using Mg-K $\alpha$  X-ray source ( $h\nu=1253.6$  eV) under high vacuum condition of around  $5.0 \times 10^{-6}$  Pa. Raman spectra of the samples were obtained using a RENISHAW Raman spectrometer (inVia Reflex) with an excitation wavelength of 532 nm. The pyrolysis behavior for the nitrate-urea-cotton mixtures was evaluated by a thermogravimetric analyzer combined with a differential thermal analyzer (TG-DTA, NETZSCH STA 2500 Regulus).

The SSA, pore volume and pore size distribution of the samples were characterized by nitrogen adsorption using a Microtrac-BEL (BELSORP-mini) surface area analyzer. The total pore volumes ( $V_{0.95}$ ) were determined from the amount of N<sub>2</sub> adsorbed at the relative pressure  $P/P_0$  of 0.95, corresponding to pores with diameters up to around 40 nm. The SSA was calculated by both Brunauer-Emmett-Teller (BET) and t-plot methods. The t-plot analysis directly deduced the total surface area ( $a_{total}$ ), external (mesopore) surface area ( $a_{ex}$ ) and micropore volume ( $V_{micro}$ ).

Based on this, the micropore surface area ( $a_{micro}$ ) was determined by  $a_{total}-a_{ex}$ , and the mesopore volume ( $V_{meso}$ ) was calculated by  $V_{0.95}-V_{micro}$ . Here  $V_{0.95}$  was used as the sum of meso- and micropore to avoid the overestimation of mesopore volume. The pore size distributions were estimated by non-localized density functional theory (NLDFT) method using the absorption data with a slit-type pore model.

### 4-3. Results and discussion

#### 4-3-1. TG-DTA analysis for pyrolysis behavior of the precursors

The pyrolysis behavior of the precursors was characterized by TG-DTA analysis as shown in **Figure 4-2**. It is observed that the pyrolysis of the nitrate-urea-cellulose involves exothermic reactions with sudden weight decreases (**Figure 4-2** (a-c)), which occur at around 250°C for the magnesium nitrate-added samples and at 300°C for the potassium nitrate-added samples. In addition, the weight

decreases lower than around 100°C in the TG curves were due to the evaporation of absorbed and bonded water. This kind of exothermic reaction is the well-known redox reaction, which is also known as nitrate-introduced combustion reaction. The carbohydrates act as the reductant fuels, while the nitrates are the oxidant.<sup>1-3</sup> Here, the carbohydrates act as the reductant fuels, while the nitrates are the oxidant. This process is quite different from the endothermic reaction of the direct pyrolysis of pure cellulose, which requires higher decomposition temperature and proceeds slowly, as shown in **Figure 4-2 (d)**. The exothermic pyrolysis of nitrate-urea-cotton proceeds very fast and efficiently, which can be finished in several minutes when the precursor is ignited. It is also observed that when magnesium nitrate is added, the introduced samples are expanded largely in volume as compared to the only potassium nitrate introduced sample. The use of magnesium nitrate and potassium nitrate makes greatly different pore structure to the final carbon products, which will be discussed in the following sections.

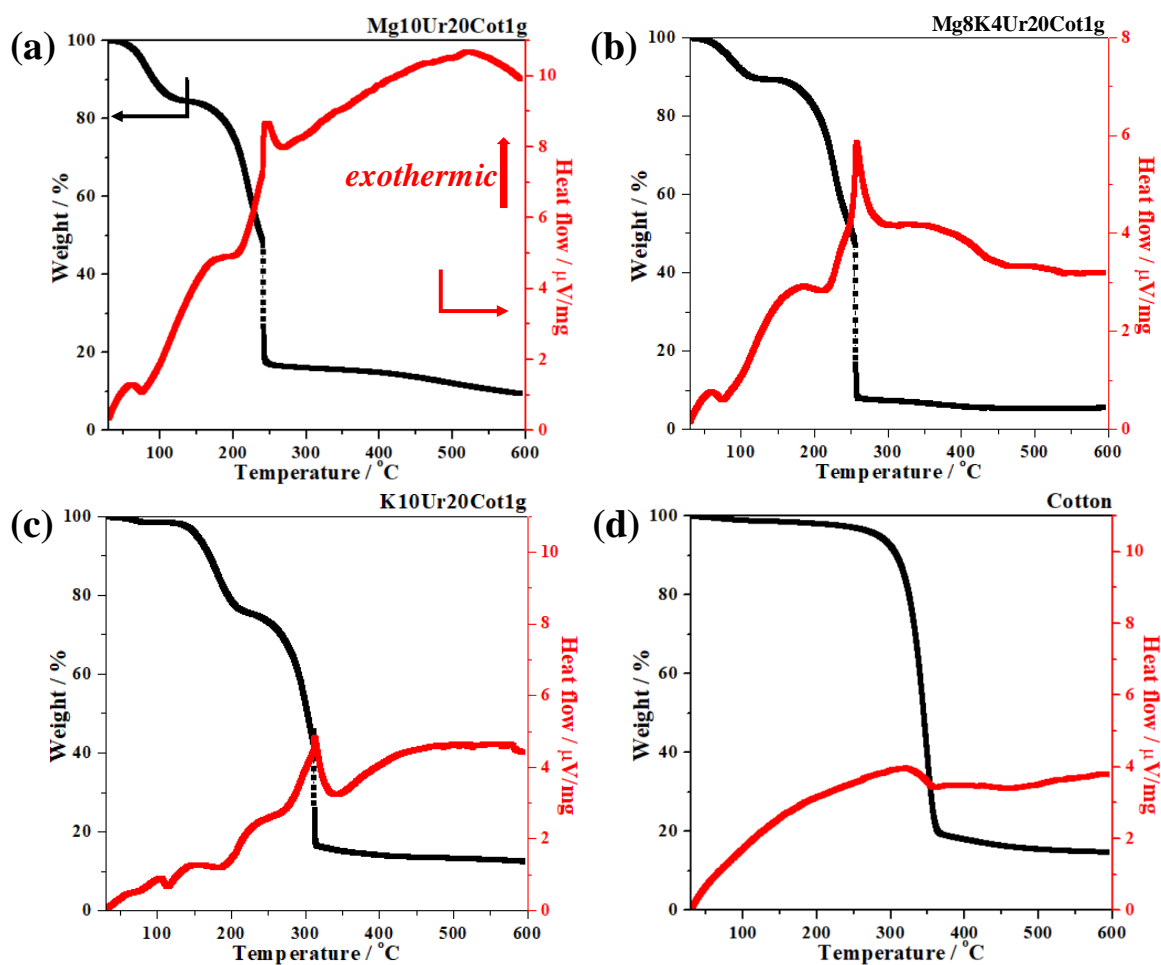


**Figure 4-2.** TG-DTA curves of the pyrolysis behavior of different precursors. (a) Mg10Ur20Cot1g; (b) Mg8K4Ur20Cot1g; (c) K10Ur20Cot1g; and (d) only cotton.

### 4-3-2. Structure characterization of the precursors & the NHPCs with a tunable pore structure by XRD patterns

The phase composition of the precursors and the NHPCs obtained were evaluated by XRD analysis as shown in **Figure 4-3** and **Figure 4-4**. The typical XRD pattern for the magnesium-potassium nitrate-induced samples after pyrolysis at 500°C is shown in **Figure 4-3**. As shown in **Figure 4-3** (a), the only magnesium nitrate-introduced sample after pyrolysis at 500°C contains broadened carbon 002 peak and peaks referring to MgO phase. As shown in **Figure 4-3** (b), the magnesium and potassium nitrate-introduced sample, Mg8K4Ur20Cot1g after pyrolysis at 500°C, presents the phases of  $K_2CO_3$ ,  $K_2CO_3 \cdot 1.5H_2O$ , KCN, KOCN, and MgO. **Figure 4-3** (c) shows the only potassium nitrate-introduced sample after pyrolysis at 500°C, which contains phases of  $K_2CO_3$ ,  $K_2CO_3 \cdot 1.5H_2O$ , KCN, and KOCN. Here, the  $K_2CO_3 \cdot 1.5H_2O$  phase in the potassium nitrate-introduced samples was due to the reaction of  $K_2CO_3$  with water when the samples were exposed to air.

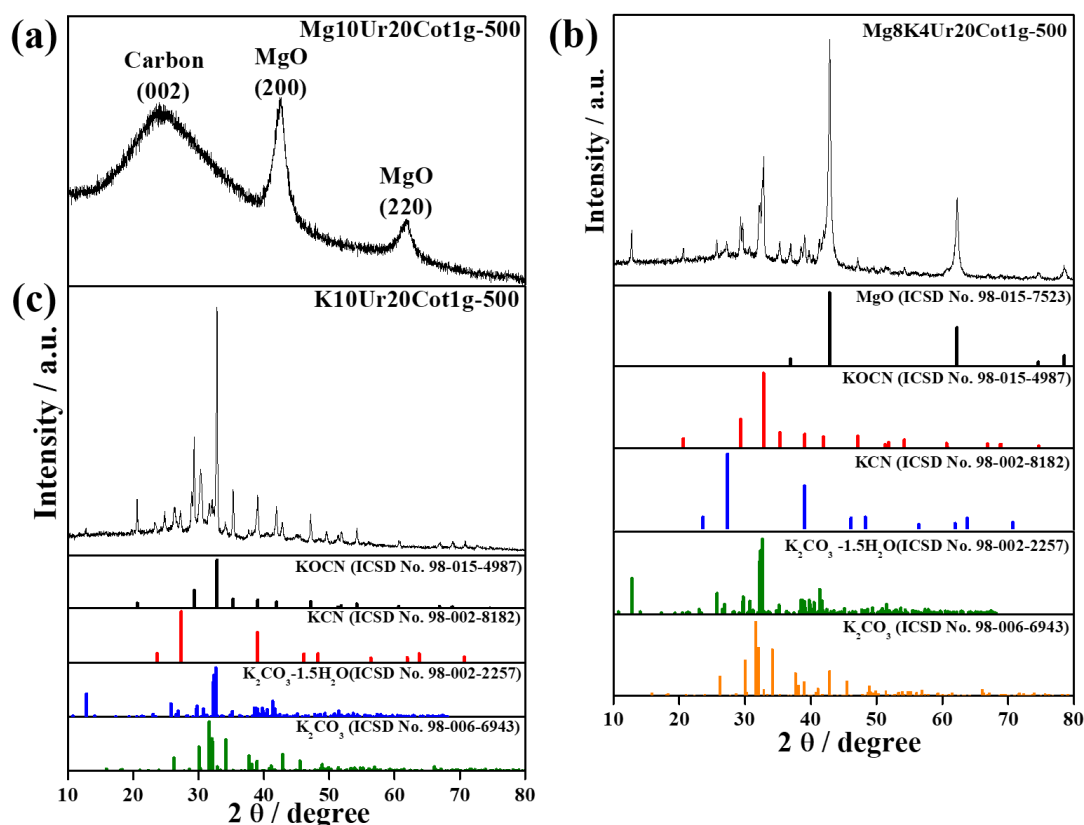


**Figure 4-3.** XRD pattern of the Mg10Ur20Cot1g-500 (a); Mg8K4Ur20Cot1g-500 (b); and the K10Ur20Cot1g-500°C (c).

The pre-pyrolyzed precursors were further carbonized at 800-1000°C, with the XRD patterns shown in **Figure 4-4** (a) and **Figure 4-4** (b). For the samples treated at 900 and 1000°C, including Mg10Ur20Cot1g-900, Mg9K2Ur20Cot1g-900, Mg8K4Ur20Cot1g-900, and Mg8K4Ur20Cot1g-1000, a single phase of MgO is observed from the XRD patterns; the XRD peaks for Mg8K4Ur20Cot1g-800 obtained at 800°C presents multi-phases including MgO, KOCN and KCN; in addition, the carbonized K10Ur20Cot1g-900 presents weak peaks of KCN and  $K_2CO_3 \cdot 1.5H_2O$ . After washing treatment, the magnesium and potassium species can be easily removed. The XRD patterns for these washed samples in **Figure 4-4** (c) and **Figure 4-4** (d) present the typical amorphous carbon diffraction patterns with greatly broadened peaks at around 23 and 42°, corresponding to carbon 002 and 10, respectively.

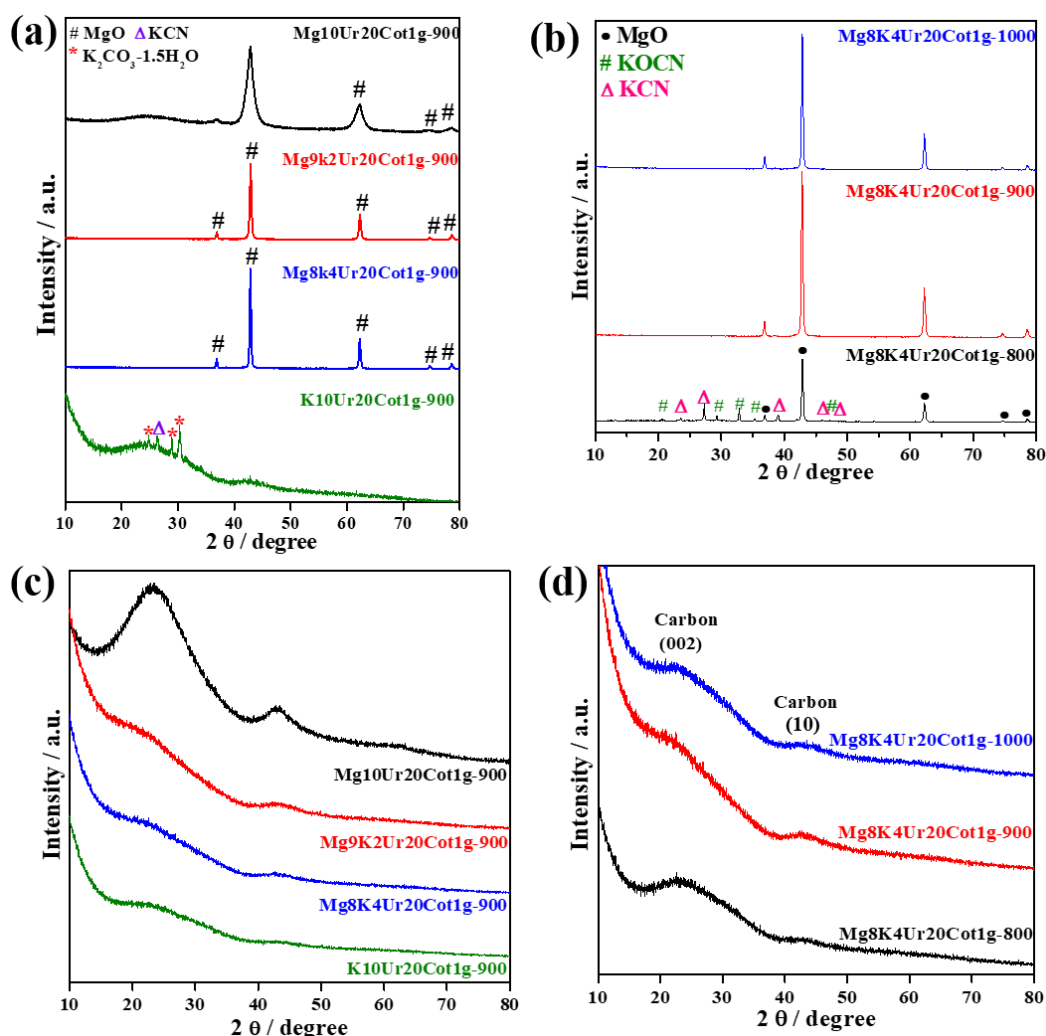


**Figure 4-4.** XRD patterns of the samples obtained after carbonization (a, b) and acid washing (c, d), respectively. (a, c) The samples with different precursor salts; (b, d) the Mg8K4Ur20 samples with different carbonization temperature.

### 4-3-3. Morphological characterization

SEM and TEM techniques were used for the morphology and microstructure observation of the samples, as shown in **Figure 4-5**, **Figure 4-6** and **Figure 4-7**. **Figure 4-5** shows the typical SEM images for samples after carbonization. The magnesium nitrate-added samples are highly porous with pores in the range of several tens of nanometers to several hundreds of nanometers; in addition, many nanoparticles of several tens of nanometers according to MgO are observed to be confined in the porous carbon matrix. However, the only potassium nitrate-introduced sample is less porous, and these nanoparticles are not observed. The carbonized samples were further washed to obtain the final carbon products. The magnesium nitrate-introduced carbon samples present enhanced porous structure as compared with the only potassium nitrate-introduced one.

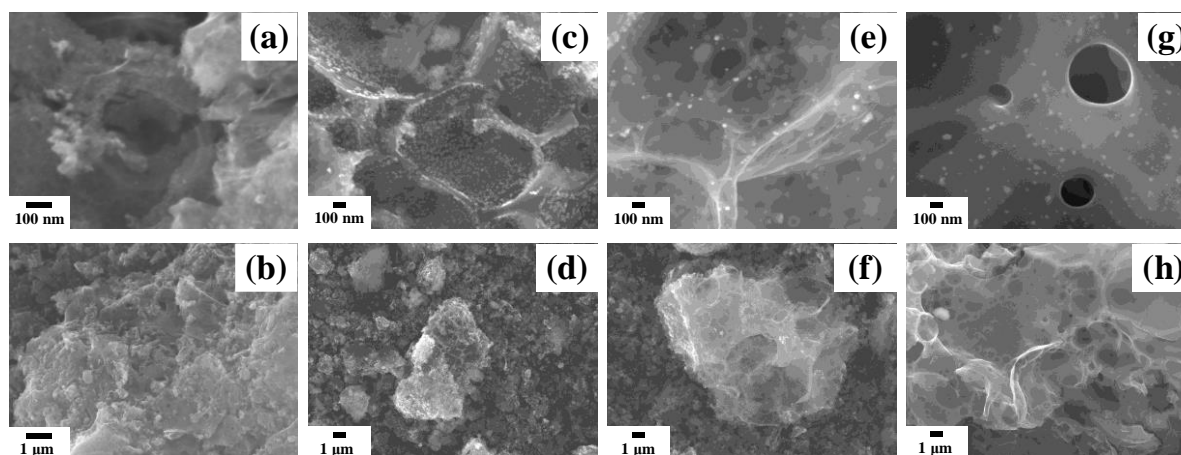


**Figure 4-5.** Typical SEM images of the samples obtained after heat treatment. (a-b) Mg10Ur20Cot1g-900, (c-d) Mg9K2Ur20Cot1g-900, (e-f) Mg8K4Ur20Cot1g-900, and (g-h) K10Ur20Cot1g-900.

**Figure 4-6** shows the SEM images of the NHPCs with a tunable pore structure. The magnesium nitrate-introduced carbon samples, such as Mg10Ur20Cot1g-900, Mg9K2Ur20Cot1g-900, Mg8K4Ur20Cot1g-900, Mg8K4Ur20Cot1g-800, and Mg8K4Ur20Cot1g-900, are highly porous, containing pores in a wide range of several nanometers to several hundreds of nanometers as seen from the SEM images; however, the K10Ur20Cot1g-900 carbon is less porous, and only a few big pores of larger than around 100 nm are observed from the SEM images.

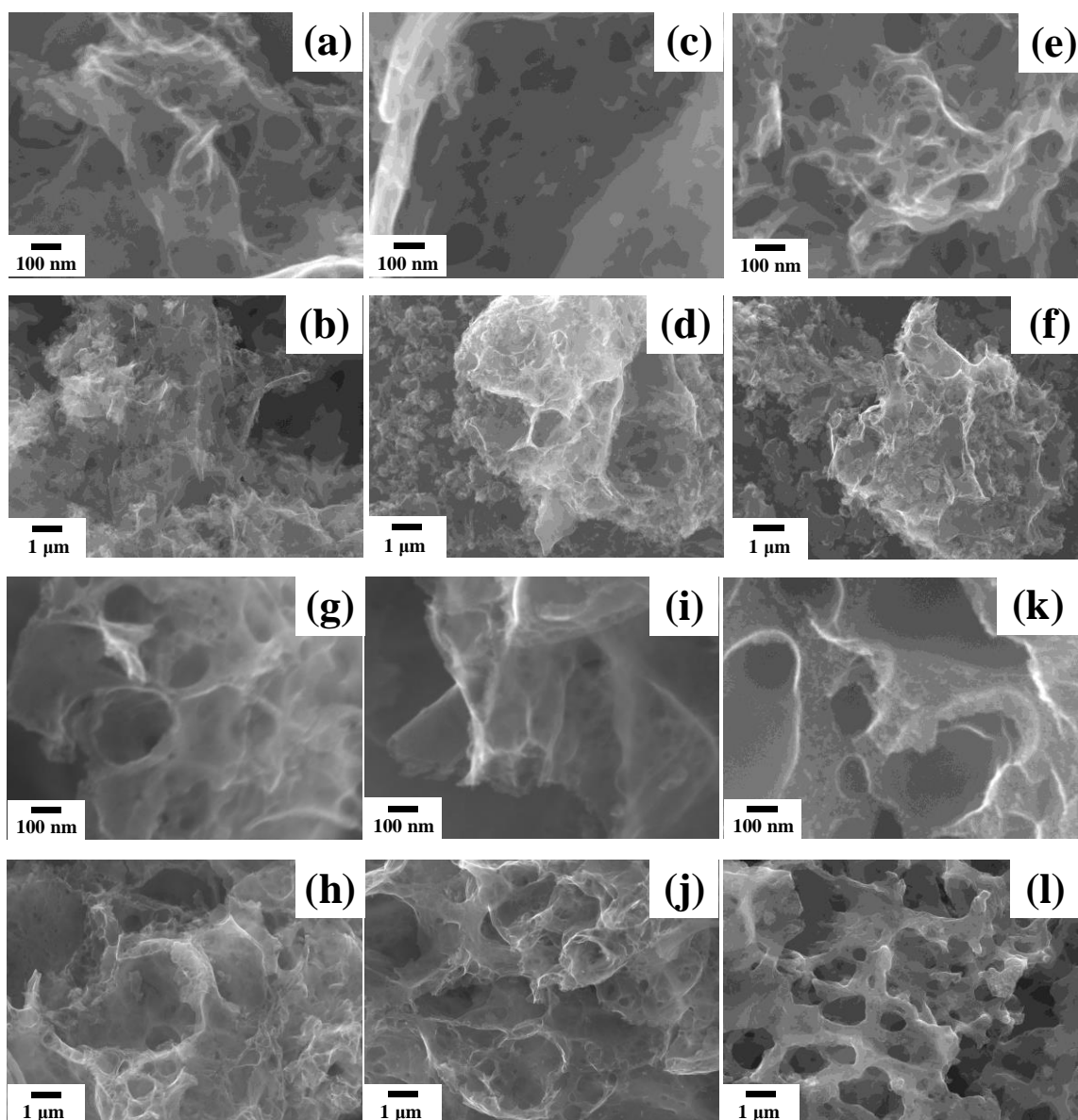


**Figure 4-6. Typical SEM images of the final carbon samples obtained after washing. (a, b) Mg<sub>10</sub>Ur<sub>20</sub>Cot<sub>1</sub>g-900, (c, d) Mg<sub>9</sub>K<sub>2</sub>Ur<sub>20</sub>Cot<sub>1</sub>g-900, (e, f) Mg<sub>8</sub>K<sub>4</sub>Ur<sub>20</sub>Cot<sub>1</sub>g-900, (g, h) Mg<sub>8</sub>K<sub>4</sub>Ur<sub>20</sub>Cot<sub>1</sub>g-800, (i, j) Mg<sub>8</sub>K<sub>4</sub>Ur<sub>20</sub>Cot<sub>1</sub>g-1000, and (k, l) K<sub>10</sub>Ur<sub>20</sub>Cot<sub>1</sub>g-900.**

The porous structures for Mg<sub>8</sub>K<sub>4</sub>Ur<sub>20</sub>Cot<sub>1</sub>g-900 and K<sub>10</sub>Ur<sub>20</sub>Cot<sub>1</sub>g-900 were further confirmed by TEM observation in **Figure 4-7**. It is observed from the TEM image in **Figure 4-7** (a), sample Mg<sub>8</sub>K<sub>4</sub>Ur<sub>20</sub>Cot<sub>1</sub>g-900 contains a large number of interconnected mesopores in the range of several tens of nanometers (< 50 nm) and macropores in the range of several tens of nanometers (>50 nm) to several hundreds of nanometers. The high-resolution image in **Figure 4-7** (b) indicates that the carbon is highly defective with the typical distorted amorphous carbon fringes and the carbon contains

numerous small micropores of less than 2 nm. The highly interconnected mesopores in the range of several tens of nanometers are not observed for sample K10Ur20Cot1g-900; however, this sample contains numerous small nanopores of the size less than around 4 nm, as shown in **Figure 4-7** (c, d).

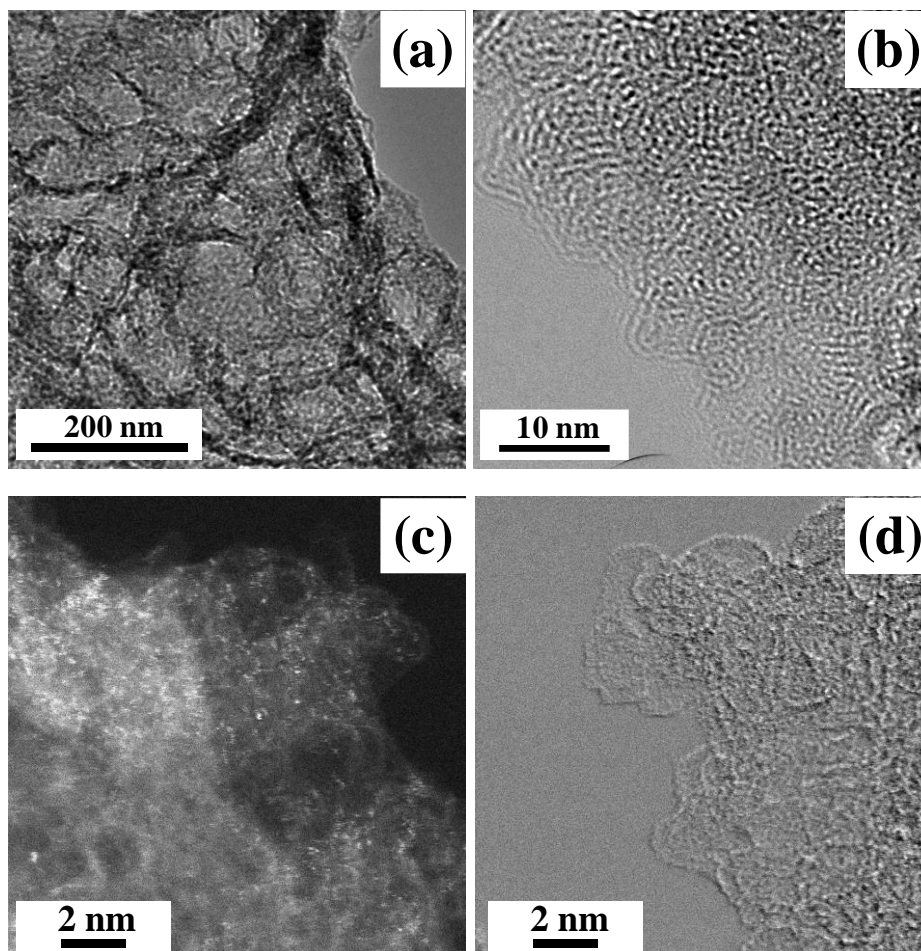


**Figure 4-7.** TEM (a, c) and HR-TEM (b, d) observation results of the typical samples. (a, b) sample Mg8K4Ur20Cot1g-900 after washing; (c, d) K10Ur20Cot1g-900 after washing.

#### 4-3-4. Characterization by N<sub>2</sub> adsorption/desorption measurements

The above morphology observation was used to qualitatively observe the porous features of obtained carbon samples. In this section, the nitrogen adsorption/desorption measurements were carefully conducted to analyze the porous characteristics of the samples. The porous features including SSA, pore volume and pore size distribution of samples were compared. **Figure 4-8** shows the nitrogen adsorption/desorption isotherms and NLDFT pore size distributions for the final carbon samples after washing treatment.

The adsorption curves for the magnesium nitrate-added samples (Mg10Ur20Cot1g-900, Mg9K2Ur20Cot1g-900, Mg8K4Ur20Cot1g-900, Mg8K4Ur20Cot1g-800 and Mg8K4Ur20Cot1g-1000) illustrate the typical hysteresis type isotherms, showing large absorption-desorption hysteresis in relative pressure  $P/P_0$  ranging from  $\sim 0.5$  to  $0.8$ . This indicates the existence of numerous mesopores ( $2\sim 50$  nm). These isotherms also present sharp increases of adsorption at a relative pressure of  $\sim 0.9\text{--}1.0$ , representing the presence of macropores ( $> 50$  nm). These isotherms also show steep absorption at  $P/P_0$  near  $0$ , indicating the existence of many micropores ( $< 2$  nm). However, for sample K10Ur20Cot1g-900, the absorption-desorption hysteresis in relative pressure  $P/P_0$  ranging from  $\sim 0.5$  to  $0.8$  and the steep absorption at a relative pressure of  $\sim 0.9\text{--}1.0$  is very limited, indicating the shortage of mesopores and macropores for this sample. NLDFT pore size distributions of these samples clearly confirm these differences.

From **Figure 4-8** (c, d), one can find that the magnesium nitrate-added samples present numerous large mesopores ( $> 4$  nm) and macropores, which were created by the vigorous exothermic pyrolysis with a large amount of gas emission and the removal of MgO nanoparticles. These samples also contain plenty of small pores ( $< 4$  nm); the pore ratio in this size range ( $< 4$  nm), especially for the micropores less than  $2$  nm, is decreased with the increase of magnesium ratio in the Mg/K-nitrates. However, for sample K10Ur20Cot1g-900, the pore distribution is limited to size of almost less than  $4$  nm, and this sample presents a large ratio of pores less than  $2$  nm. These differences in pore size distribution are caused by the different role of magnesium and potassium compounds, in which magnesium compound creates pores large than  $4$  nm while potassium compounds account for the formation small nanopores less than  $4$  nm.

The porous indicators including SSA and pore volumes for the carbon samples are summarized in **Table 4-1**. Sample Mg10Ur20Cot1g-900 presents the lowest BET SSA of  $1102\text{ m}^2\text{ g}^{-1}$ . With the addition of potassium precursor, the BET SSA of the samples is greatly increased, which are  $2071\text{ m}^2\text{ g}^{-1}$  for Mg9K2Ur20Cot1g-900,  $2600\text{ m}^2\text{ g}^{-1}$  for Mg8K4Ur20Cot1g-900 and  $2486\text{ m}^2\text{ g}^{-1}$  for K10Ur20Cot1g-900. The pore volumes are also greatly increased for the potassium added samples. The SSA and pore volume of the porous carbons are considered to greatly affect their capacitance.

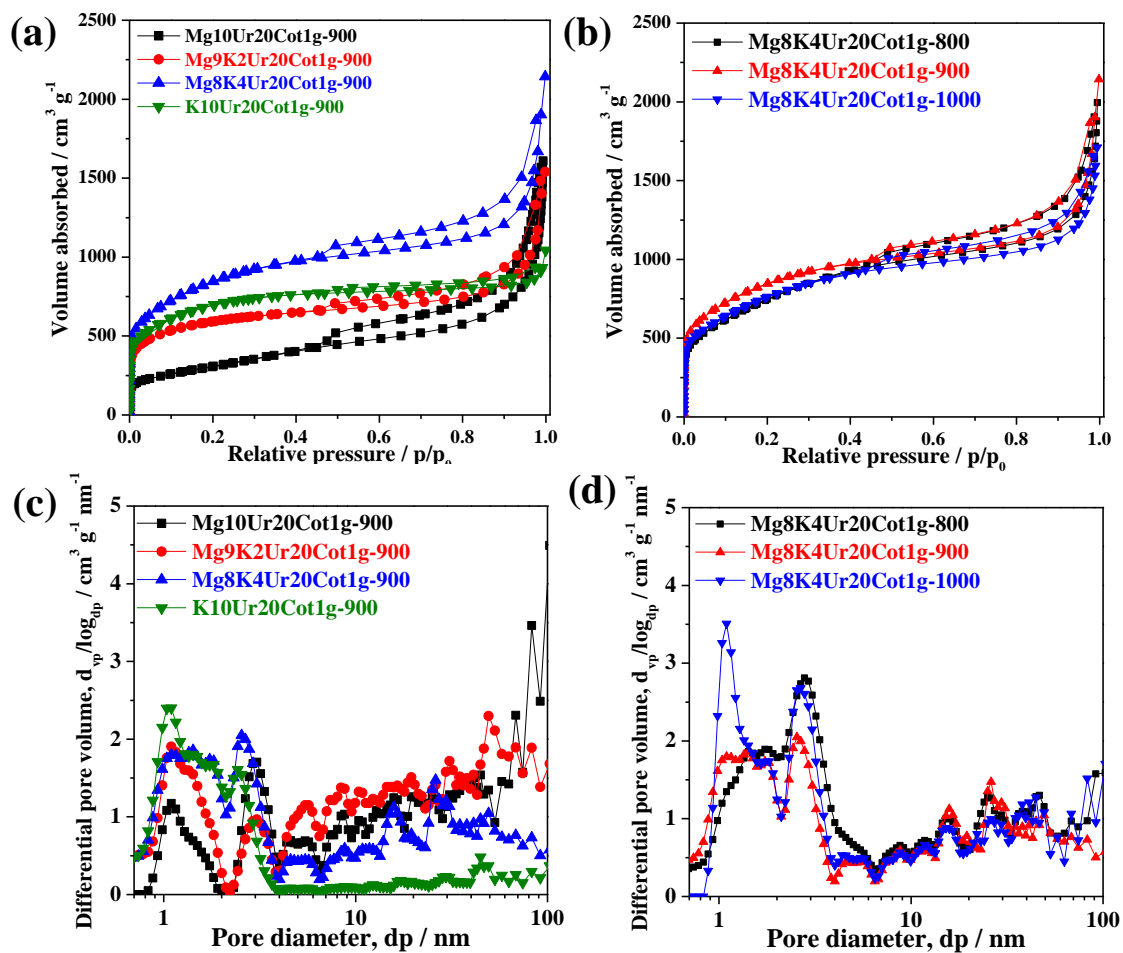


Figure 4-8. Nitrogen adsorption isotherm (a, b) and NLDFT pore size distribution (c, d) for the final carbon samples obtained after washing treatment.

**Table 4-1. Summary of the porous characteristics of porous carbon products obtained after acid washing.**

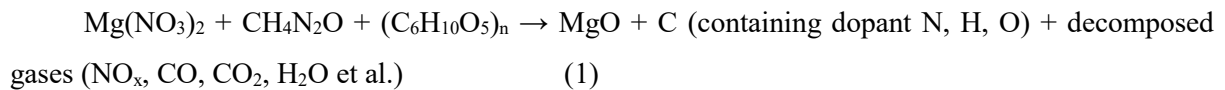
|                     | BET<br>SSA<br>(m <sup>2</sup> g <sup>-1</sup> ) | a <sub>total</sub><br>(m <sup>2</sup> g <sup>-1</sup> ) | a <sub>ex</sub><br>(m <sup>2</sup> g <sup>-1</sup> ) | a <sub>micro</sub> =a <sub>total</sub> -<br>a <sub>ex</sub><br>(m <sup>2</sup> g <sup>-1</sup> ) | V <sub>0.95</sub><br>(cm <sup>3</sup> g <sup>-1</sup> ) | V <sub>micro</sub><br>(cm <sup>3</sup> g <sup>-1</sup> ) | V <sub>meso</sub> =V <sub>0.95</sub><br>-V <sub>micro</sub><br>(cm <sup>3</sup> g <sup>-1</sup> ) |
|---------------------|---|---|--|--|---|--|---|
| Mg10Ur20Cot1g-900   | 1102  | 1073  | 468  | 605  | 1.31  | 0.48   | 0.83  |
| Mg9K2Ur20Cot1g-900  | 2071  | 2217  | 350  | 1867   | 1.47  | 0.84   | 0.63  |
| Mg8K4Ur20Cot1g-800  | 2743  | 2407  | 372  | 2035   | 2.04  | 1.38   | 0.64  |
| Mg8K4Ur20Cot1g-900  | 2600  | 2355  | 386  | 1969   | 1.83  | 1.17   | 0.66  |
| Mg8K4Ur20Cot1g-1000 | 2774  | 2564  | 321  | 2243   | 1.90  | 1.34   | 0.56  |
| K10Ur20Cot1g-900    | 2486  | 2480  | 83   | 2397   | 1.30  | 1.16   | 0.14  |

BET SSA: specific surface area as-calculated from the adsorption data by BET method; V<sub>0.95</sub>: total pore volume at P/P<sub>0</sub>=0.95, corresponding to the pores with diameters up to around 40 nm; a<sub>total</sub>: the total surface area as determined by t method; a<sub>ex</sub>: the external surface area as determined by t method; a<sub>micro</sub>: the micropore surface area as determined by a<sub>total</sub>-a<sub>ex</sub>; V<sub>micro</sub>: the micropore volume as-analyzed by t method; V<sub>meso</sub>: the mesopore volume as-determined by V<sub>0.95</sub>-V<sub>micro</sub>.

#### 4-3-5. Discussion on the pore formation mechanism

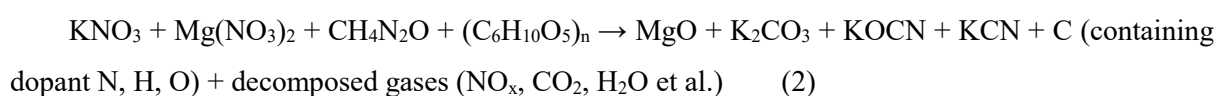
Based on the above characterization results, the reactions occurred in the whole process and the pore formation mechanism is discussed in this section.

For the magnesium nitrate-urea-cellulose case, during the pre-pyrolysis process, the following total reaction is proposed to occur:



The continuing high-temperature heat treatment induces further carbonization of the amorphous carbon precursor, while MgO phase is dispersed in the carbon matrix showing no phase change during heat treatment, as confirmed by XRD analysis. During the pre-pyrolysis process, many macropores are

formed due to the vigorous exothermic reaction with the emission of a large amount of gases. Washing treatment removes the MgO template, creating numerous micro-mesopores in the carbon. Especially, the MgO template has the size of several to several tens of nanometers as confirmed by SEM, inducing the formation of numerous mesopores. When potassium nitrate is also added in the precursors, the involved reactions are much more complex. As evidenced by the previous XRD analysis, after the pre-pyrolysis, five substances are formed for the Mg•K nitrate added samples, including the amorphous carbon (containing dopants of N, H, O), MgO, K<sub>2</sub>CO<sub>3</sub>, KCN, and KOCN. The total reaction can be written in the following formula:

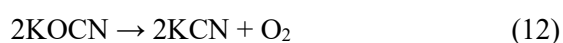


Here, Mg(NO<sub>3</sub>)<sub>2</sub> is decomposed to form MgO nanoparticles, which are also stable during the high-temperature carbonization process, as evidenced by the XRD analysis. KNO<sub>3</sub> is decomposed and further reacts with the carbohydrate-derived species (CO<sub>2</sub>, HOCN, HCN, H<sub>2</sub>O, etc.) to form potassium compounds including K<sub>2</sub>CO<sub>3</sub>, KCN, and KOCN. Decomposition of cellulose may release CO<sub>2</sub>, H<sub>2</sub>O, and other C-H gases, while the pyrolysis of urea may release gases such as HOCN, HCN, and NH<sub>3</sub> etc.<sup>4</sup>  
<sup>5</sup> The proposed potassium-included reactions in the pre-pyrolysis step (up to 500 °C) may contain follows:



With further heating to high temperatures for carbonization, the compositions of potassium compounds change based on the carbonization temperature. At 800°C, the carbonized sample contains four substances, including carbon, MgO, KCN and KOCN. Here, K<sub>2</sub>CO<sub>3</sub> phase disappears, which is decomposed at a temperature higher than 700°C<sup>6</sup> and reacts with the C-N species to form KCN and metallic K. Here, the KCN XRD peak intensity in the 800 °C sample become stronger, while the peak for KOCN become weaker as compared to the corresponding precursor obtained at 500°C. The reported decomposition temperature for KOCN is around 700-900°C. Therefore, the high-temperature activation

reactions for the highly porous carbon samples may contain:



In addition, At the much higher temperature of 900 and 1000°C, potassium species are almost removed due to the carbon reduction to form metallic potassium and its evaporation. The evaporation of metallic potassium makes a lot of small cracks in the carbon. It is observed from the XRD patterns that the carbonized samples at 900 and 1000°C present a small amount of potassium-related species. EDS analysis as shown in **Figure 4-9** also confirms the removal of potassium at treatment temperature higher than 900°C. Finally, with washing treatment to remove the potassium species and MgO template, abundant micro-mesopores are created in the final carbon sample.

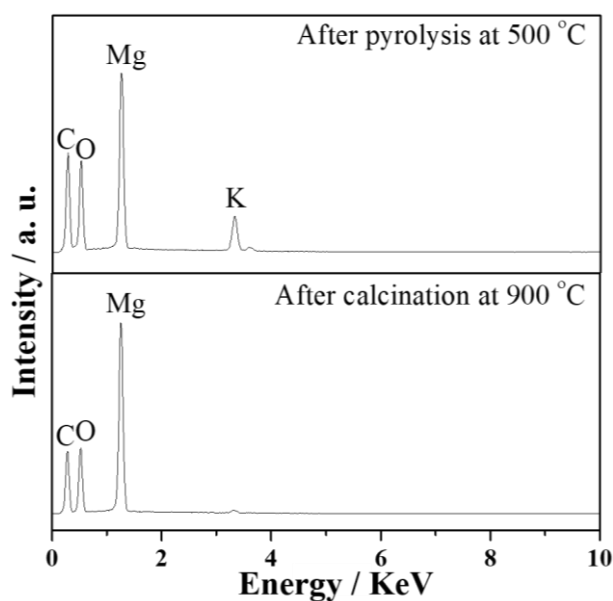


**Figure 4-9.** Typical EDS spectra for the samples obtained after carbonization at 500 and 900 °C.

The addition of potassium nitrate in the precursor accounts for the increase of specific surface area and pore volume, especially for the small nanopores (< 4 nm). The potassium compounds act as both template and corrosive agent to carbon for creating small nanopores. This is similar but more complex than the conventional KOH activation process for activated carbons since the presence of N makes the formation of more complex potassium compounds.<sup>6</sup>

As for the only potassium nitrate-introduced sample, a few macropores larger than 100 nm, as confirmed by SEM observation, were also created due to the emission of a large amount of gases during pyrolysis; the continuing carbonization process at high temperature induced the potassium-based activation process to create numerous nanopores (mainly less than 4 nm). Particularly, the numerous mesopores (> 4 nm) are not contained in this sample.

In summary, the nitrate-induced exothermic reaction is vigorous and fast, which emits a lot of gases that will create many large macropores in the pyrolyzed carbon; the magnesium nitrate addition in the precursor accounts for the formation of a large number of mesopores (mainly > 4 nm) due to the introduction of MgO nanoparticles with size ranging from several nanometers to several tens of nanometers; the introduced potassium compounds are responsible for the formation of small nanopores less than 4 nm due to the activation effect of potassium species. By controlling the use of magnesium and potassium nitrate, we can obtain a series of porous carbon with tunable pore size distribution and high specific surface area. The as-synthesized porous carbons with typical pore structures are: (1) Mg10Ur20Cot1g-900 has the continuous and interconnected micro-meso-macro hierarchical pores, but the SSA is the lowest of 1102 m<sup>2</sup> g<sup>-1</sup>; (2) Mg8K4Ur20Cot1g-900 has continuous and interconnected micro-meso-macro hierarchical pores and very high SSA of 2600 m<sup>2</sup> g<sup>-1</sup>; (3) K10Ur20Cot1g-900 has micro-meso hierarchical nanopores, which are mainly limited to less than 4 nm, and very high SSA of 2486 m<sup>2</sup> g<sup>-1</sup>.

#### 4-3-6. XPS analysis

The elemental compositions and bonding features of the carbon materials were measured via XPS as shown in **Figure 4-10**. The survey spectra as shown in **Figure 4-11** (a, d) illustrate the presence of three obvious peaks centered at ~285, 400, and 520 eV, which can be assigned to C1s, N1s, and O1s, respectively. N element is derived from urea. O is the carbonization residue from both cellulose and urea, which is contained in all kinds of activated porous carbon. The N dopant is believed to greatly affect the electrochemical capacitance, which can make additional pseudo-capacitance and increase the wetting of the carbon. The atomic ratios of the N component are summarized in **Table 4-2**. The percentage of N dopant is decreased with increasing the heat-treatment temperature due to the enhanced

carbonization and decomposition of N species at the higher temperature. The addition of potassium precursor also increases the graphitization of carbon and decreases the amount of N dopant due to the formation of potassium compounds with N and their decomposition/reduction to metallic potassium at high temperatures.

The high-resolution spectra for C 1s and N 1s were also obtained. **Figure 4-12** (b, e) shows the C 1s spectra, which can be separated into three peaks located at around 284.8, 286.2 and 288.5 eV, referring to the C-C or C-H, C-N and/or C-O, and O=C-C bonding, respectively. The narrow scan of the N 1s spectra is shown in **Figure 4-13** (c, f). The deconvolution of the N 1s spectra shows three peaks centered at 398.6, 400.2 and 401.7 eV, corresponding to the pyridinic N, pyrrolic N, and graphitic N, respectively. The ratios for the above three N species are greatly influenced by carbonization temperature and the addition of potassium, which are summarized in **Table 4-2**. With the increase of carbonization temperature, the samples present increasing ratio of graphitic N, a slight decrease of pyridinic N and a great decrease of pyrrolic N. With the addition of potassium, the samples show the enhanced ratio of graphitic N. These results indicate the enhancement of carbonization with increasing the carbonization temperature and adding potassium precursor.

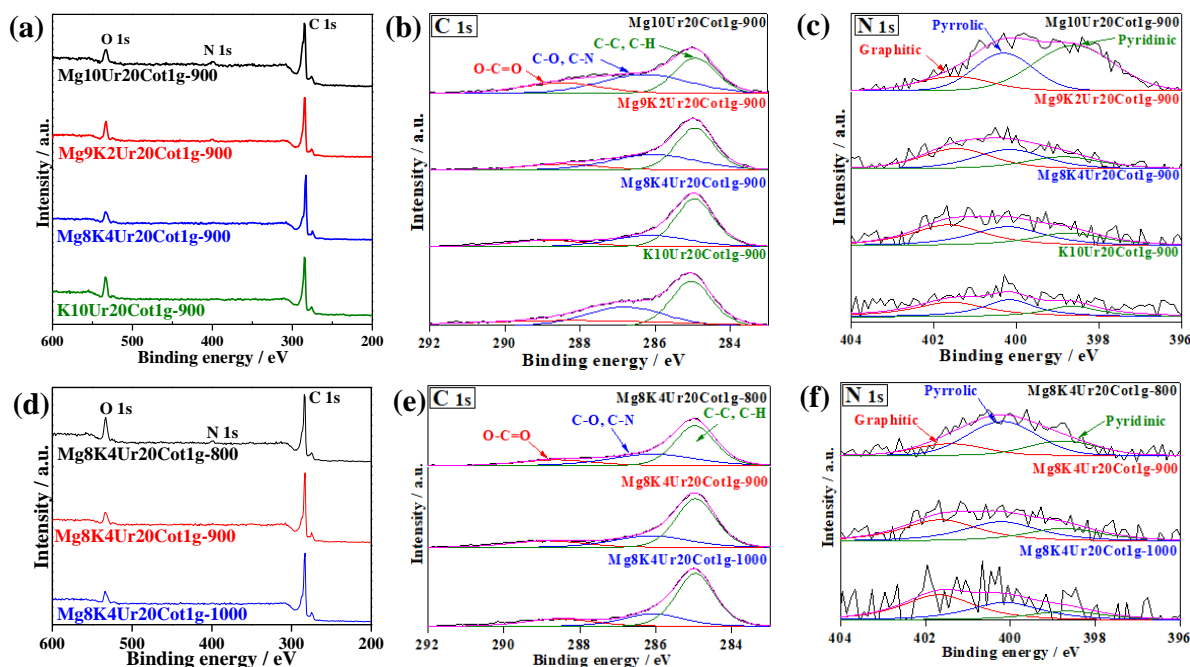


**Figure 4-14.** XPS analysis of the NHPCs with a tunable pore structure. (a, d) the wide scan; (b, e) the narrow scan of C 1s; (c, f) the narrow scan of N 1s.

**Table 4-2. Summary of the chemical bonding properties of the NHPCs with a tunable pore structure obtained by XPS.**

| <i>Samples</i>             | <i>N content</i><br>[at. %] | <i>Percentage of N species</i> |                    |                    |
|----------------------------|-----------------------------|--------------------------------|--------------------|--------------------|
|                            |                             | <b>Graphitic</b>               | <b>Pyrrolic</b>    | <b>Pyridinic</b>   |
|                            |                             | (~401.3 eV)<br>[%]             | (~400.0 eV)<br>[%] | (~398.5 eV)<br>[%] |
| <b>Mg10Ur20Cot1g-900</b>   | 4.1                         | 31.6                           | 32.2               | 36.2               |
| <b>Mg9K2Ur20Cot1g-900</b>  | 1.8                         | 38.9                           | 37.1               | 23.9               |
| <b>Mg8K4Ur20Cot1g-800</b>  | 2.0                         | 19.4                           | 56.6               | 24.0               |
| <b>Mg8K4Ur20Cot1g-900</b>  | 1.1                         | 40.3                           | 36.2               | 23.5               |
| <b>Mg8K4Ur20Cot1g-1000</b> | 0.8                         | 48.8                           | 34.1               | 17.1               |
| <b>K10Ur20Cot1g-900</b>    | 0.7                         | 41.4                           | 35.5               | 23.0               |

#### 4-4. Conclusions

In summary, we efficiently synthesized the heteroatom doped hierarchical porous carbon by using biomass cellulose as a carbon source. By involving the vigorous exothermic pyrolysis of the Mg/(K)-nitrate-urea-cellulose mixture, meso-macropores were created in the cellulose-derived carbon. After being further carbonized at high temperature and washed, additional numerous micro-mesopores were formed by removing the Mg, K compounds that were dispersed in the carbon matrix. Finally, the NHPCs interconnected micro-meso-macro-pore with very high specific surface area larger than 2700 m<sup>2</sup> g<sup>-1</sup> were produced. The addition of potassium nitrate in the raw materials could greatly increase the SSA to larger than 2000 m<sup>2</sup> g<sup>-1</sup>, as compared to the magnesium nitrate added sample with SSA of around 1100 m<sup>2</sup> g<sup>-1</sup>. This was due to the activation effect of potassium in creating numerous small micro-mesopores. The obtained porous carbons presented good capacitive performance as the electrodes in energy storage devices, due to their advantageous characteristics including high surface area, hierarchical pore structure, and heteroatom doping.

#### 4-5. References

- [1] C. Zhu, M. Takata, Y. Aoki, H. Habazaki, Nitrogen-doped porous carbon as-mediated by a facile solution combustion synthesis for supercapacitor and oxygen reduction electrocatalyst, *Chem. Eng. J.* 350 (2018) 278-289.
- [2] C. Zhu, A. Nobuta, I. Nakatsugawa, T. Akiyama, Solution combustion synthesis of LaMO<sub>3</sub> (M = Fe, Co, Mn) perovskite nanoparticles and the measurement of their electrocatalytic properties for air cathode, *Int. J. Hydrogen Energy* 38 (2013) 13238-13248.
- [3] F. Deganello, A.K. Tyagi, Solution combustion synthesis, energy and environment: Best parameters for better materials, *Prog. Cryst. Growth and Charact. Mater.* 64 (2018) 23-61.
- [4] N. Tsubouchi, M. Nishio, Y. Mochizuki, Role of nitrogen in pore development in activated carbon prepared by potassium carbonate activation of lignin, *Appl. Surf. Sci.* 371 (2016) 301-306.
- [5] P.M. Schaber, J. Colson, S. Higgins, D. Thielen, B. Anspach, J. Brauer, Thermal decomposition (pyrolysis) of urea in an open reaction vessel, *Thermochim. Acta* 424 (2004) 131-142.
- [6] J. Wang, S. Kaskel, KOH activation of carbon-based materials for energy storage, *J. Mater. Chem.* 22 (2012) 23710-23725.

## Chapter 5.

### Supercapacitor properties of the NHPCs with a tunable pore structure

#### 5-1. Introduction

In Chapter 4, the NHPCs with a tunable pore structure were prepared by Mg/Mg•K/K-nitrate template and different calcination temperature from 800 to 1000°C. Among the prepared NHPCs with a tunable pore structure, well-defined NHPCs, especially Mg<sub>8</sub>K<sub>4</sub>Ur<sub>20</sub>Cot<sub>1</sub>g calcined at 800 to 1000°C, have hierarchically porous structure with micro-, meso-, and macropores, high specific surface area more than 2500 m<sup>2</sup> g<sup>-1</sup>. These characteristics of the NHPCs with a tunable pore structure are expected to produce the high electrochemical performance.

In this chapter, the electrochemical properties of the NHPCs with a tunable pore structure were investigated by two- and three-electrode system supercapacitors with 6M KOH electrolyte. Among the NHPCs with a tunable pore structure calcined at 900°C, Mg<sub>8</sub>K<sub>4</sub>Ur<sub>20</sub>Cot<sub>1</sub>g shows the high specific capacitance at each current density and good stability at current density 2 A g<sup>-1</sup> during 10,000 cycles. Among the Mg<sub>8</sub>K<sub>4</sub>Ur<sub>20</sub>Cot<sub>1</sub>g with different calcination temperature at 800 to 1000°C, Mg<sub>8</sub>K<sub>4</sub>Ur<sub>20</sub>Cot<sub>1</sub>g-800 with high concentration of nitrogen shows the high specific capacitance at each current density due to extra pseudo-capacitance.

#### 5-2. Experimental

##### 5-2-1. Electrochemical measurements

The electrochemical measurement for supercapacitors was conducted in both a two-electrode cell and a three-electrode configuration, as shown in **Figure 5-1**. The working electrodes were prepared by mixing the obtained porous carbon, acetylene black conductive carbon, and polytetrafluoroethylene (PTFE)-coated teflonized acetylene black (TAB-2<sup>®</sup>) binder, with a weight ratio of 80:10:10, in ethanol solvent to form a dough-like paste. The electrode mixture was coated onto a disk-shaped nickel foam current collector with a diameter of 10 mm. The mass of each electrode was controlled at around 3.5 mg cm<sup>-2</sup>.

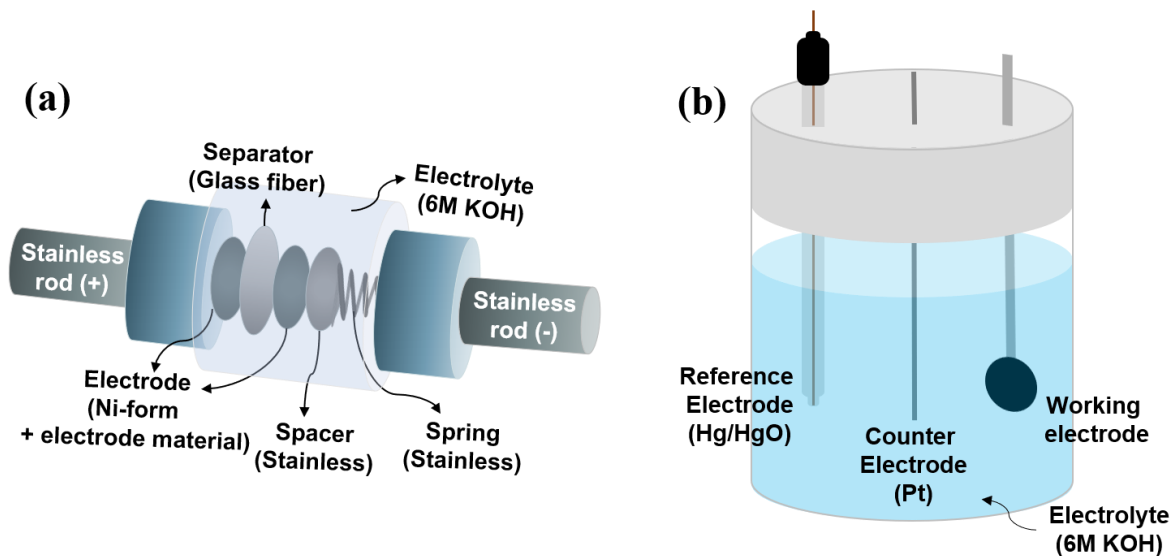


**Figure 5-1. Schematic diagram of supercapacitors. (a) Two-electrode system supercapacitor and (b) Three-electrode system supercapacitor.**

6 M KOH aqueous electrolyte was used for all measurement. For the three-electrode measurements, Pt wire and Hg/HgO electrodes were used as the counter and reference electrode, respectively. The measurements were conducted in the potential range of -1.0 V to 0.0 V vs. Hg/HgO. Cyclic voltammetry (CV) measurements were performed at a potentiostat/galvanostat electrochemistry workstation (Princeton VersaSTAT 3), while galvanostatic charge-discharge measurement was performed at a battery tester (Hokudo Denko). Electrochemical impedance spectroscopy (EIS) were measured at a frequency range of 0.1 Hz to 100 kHz and a 10 mV AC amplitude.

The specific capacitance based on three-electrode charge-discharge measurement was calculated based on the following formula:<sup>1-3</sup>

$$C = \frac{I\Delta t}{m\Delta V} \quad (1)$$

where  $C$  ( $F g^{-1}$ ) is the specific capacitance,  $I$  ( $A g^{-1}$ ) is current density,  $\Delta t$  (s) is discharge time,  $m$  (g) is the mass of a single electrode, and  $\Delta V$  (V) is the potential window during the discharge process (excluding the IR drop), respectively.

The two-electrode symmetric cell was assembled in a Swagelok-type configuration.<sup>1</sup> The

symmetric supercapacitor was tested within a voltage range from 0.0 to 1.0 V. CV and charge-discharge measurement were conducted. The specific capacitance based on two-electrode measurement was calculated based on the following formula:

$$C = \frac{2I\Delta t}{m\Delta V} \quad (2)$$

The energy density (E, Wh kg<sup>-1</sup>) and power density (P, Wh kg<sup>-1</sup>) of the two-electrode cells were calculated by using the following equations:

$$E = \frac{C(\Delta V)^2}{2 \times 3.6} \quad (3)$$

$$P = \frac{E}{\Delta t} \times 3600 \quad (4)$$

Here C (F g<sup>-1</sup>) represents the specific capacitance of the supercapacitor calculated from the discharge curves in two-electrode cells. ΔV (V) and Δt (s) refer to the voltage change within the discharge time and the discharge time, respectively.

### 5-3. Results and discussion

The supercapacitor performance of the porous carbons was evaluated in both two-electrode and three-electrode configurations using a 6 M KOH electrolyte. **Figure 5-2** to **Figure 5-4** present the two-electrode system measurement results and **Figure 5-6** to **Figure 5-8** present the three-electrode system measurement results.

#### 5-3-1. CV measurement by two-electrode system

**Figure 5-2** shows the typical CV curves for all samples which illustrate the symmetrical rectangular shape at scan rate of 10 and 100 mV s<sup>-1</sup>, excluding Mg8K4Ur20Cot1g-800. It is indicated

that the good double-layer capacitance behavior, excluding sample Mg8K4Ur20Cot1g-800. The CV curves for Mg8K4Ur20Cot1g-800 are less rectangular, especially at high scan rate, which is because of its low carbonization degree and more pseudo-capacitance derived from the abundant heteroatom dopants.

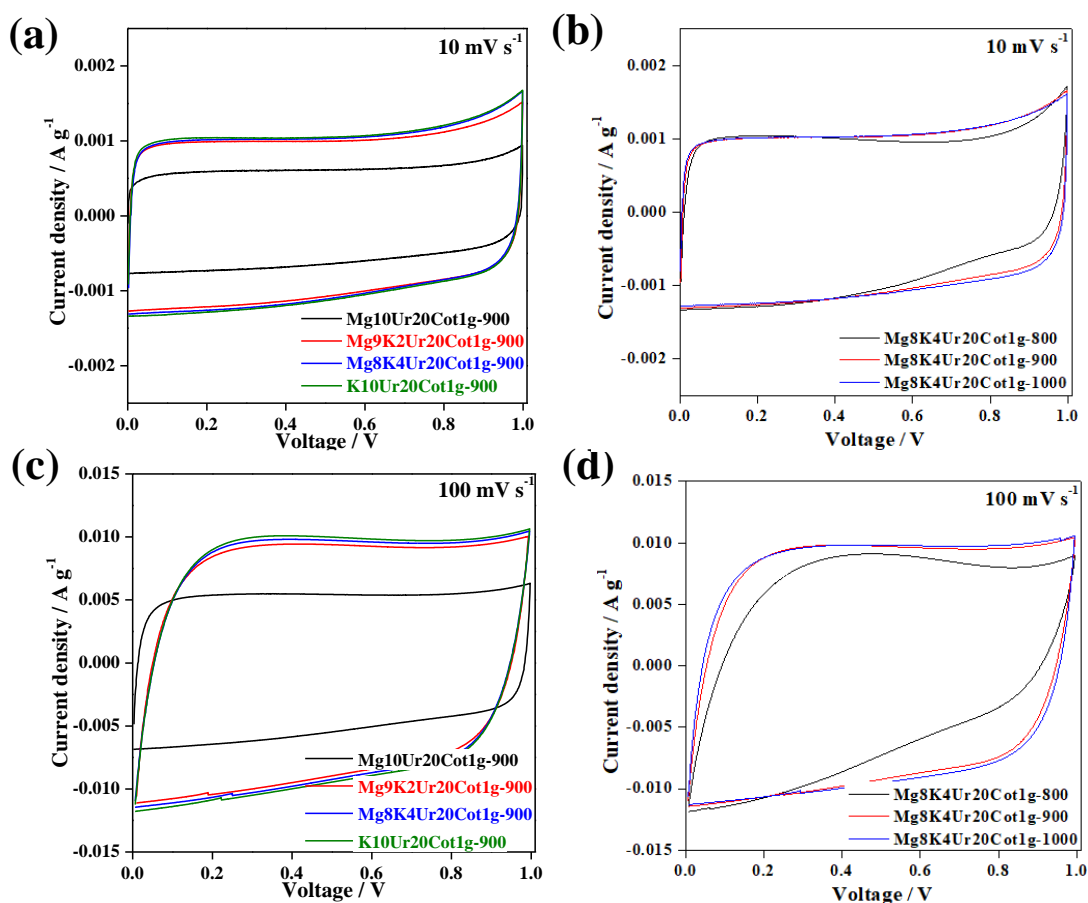
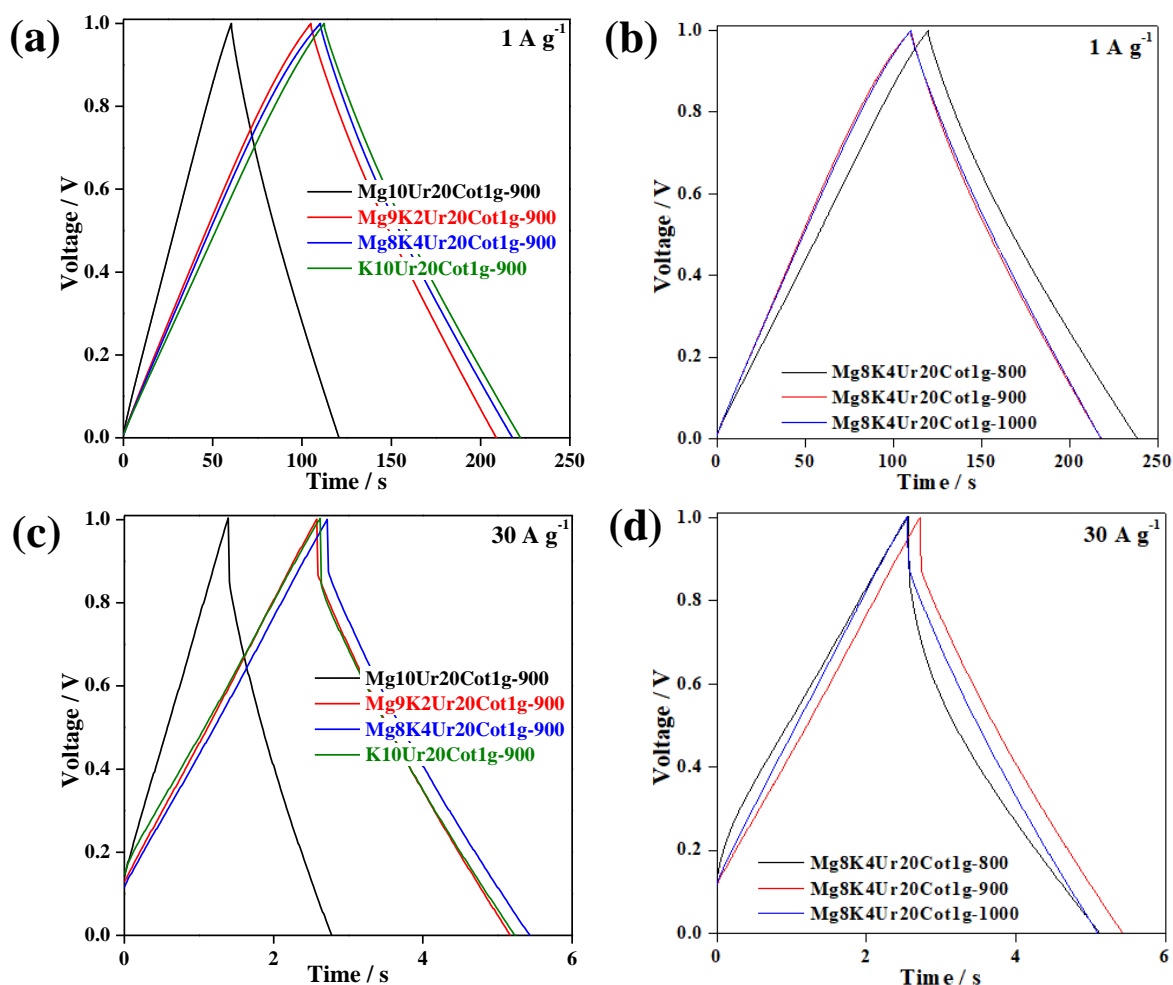


Figure 5-2. Cyclic voltammogram curves at sweep rates of (a, b)  $10 \text{ mV s}^{-1}$  and (c, d)  $100 \text{ mV s}^{-1}$ .

### 5-3-2. Galvanostatic charge and discharge curves by two-electrode system

The galvanostatic charge-discharge curves for all samples were obtained at current density of 1 and  $30 \text{ A g}^{-1}$ , as shown in **Figure 5-3**. All the charge-discharge curves, excluding the one for sample Mg8K4Ur20Cot1g-800 at the high current density of  $30 \text{ A g}^{-1}$ , present symmetric triangular shapes, indicating the typical double-layer capacitive behavior of the porous carbon with good reversibility, which agree well with CV measurement. The deformed curves for sample Mg8K4Ur20Cot1g-800 at  $30 \text{ A g}^{-1}$  is due to its low conductivity of this sample obtained at low carbonization temperature.



**Figure 5-3.** Two-electrode test of supercapacitors in 6 M KOH. Galvanostatic charge-discharge curves at current density of (a, b)  $1 \text{ A g}^{-1}$  and (c, d)  $30 \text{ A g}^{-1}$ .

### 5-3-3. Specific capacitance at various current density and long cycle stability by two-electrode system

**Figure 5-4** summarizes the gravimetric specific capacitance of the NHPCs with a tunable pore structure at various current densities. **Figure 5-4 (a)** and **Figure 5-4 (b)** show the specific capacitance at various current density and **Figure 5-4 (c)** and **Figure 5-4 (d)** show the long cycle stability in 10,000 cycles at a current density of  $2 \text{ A g}^{-1}$ .

Among the three samples carbonized at  $900^\circ\text{C}$  in **Figure 5-4 (a)**, sample Mg8K4Ur20Cot1g-900 presents the largest capacitances with values of 241 and  $195 \text{ F g}^{-1}$  at 1 and  $30 \text{ A g}^{-1}$ , respectively. The greatly increased capacitances for sample Mg8K4Ur20Cot1g-900 is due to its highest SSA as compared with other samples. As shown in **Figure 5-4 (b)**, for the Mg8K4Ur20Cot1g samples carbonized at 800- $1000^\circ\text{C}$ , the one obtained at  $800^\circ\text{C}$  presents the highest capacitances with values of 279 and  $235 \text{ F g}^{-1}$

at 1 and 30 A g<sup>-1</sup>, respectively. Although the SSAs of these three samples are similar, sample Mg8K4Ur20Cot1g-800 shows larger capacitances, which is due to its larger amount of heteroatom dopants, making the increased pseudo-capacitance.

To further evaluate the relationship between the pore structure/N-doping content and the SC properties of these samples, the specific capacitances (F m<sup>-2</sup>) are also calculated for the typical samples at current densities of 1 and 30 A g<sup>-1</sup>, which are summarized in **Figure 5-4 (c, d)**. **Figure 5-4 (c)** shows the comparison of the samples carbonized at the same temperature of 900°C. It is noted that the specific capacitance decreases in the following sequence: Mg10Ur20Cot1g-900 > Mg8K4Ur20Cot1g-900 > K10Ur20Cot1g-900. This is mainly caused by N content and pore structure of the carbon samples. Mg10Ur20Cot1g-900 and Mg8K4Ur20Cot1g-900 have similar hierarchical porous structure with interconnected micro-meso-macropores. Although the SSA of Mg8K4Ur20Cot1g-900 is around double of Mg10Ur20Cot1g-900, Mg10Ur20Cot1g-900 has higher specific capacitance which is due to the higher N content of 4.1% for Mg10Ur20Cot1g-900 than 2.0% for Mg8K4Ur20Cot1g-900. The high content of heteroatom dopant can increase the pseudo-capacitance. By comparing sample Mg8K4Ur20Cot1g-900 and K10Ur20Cot1g-900, the SSA of these two samples are similar, however, the specific capacitance is larger for sample Mg8K4Ur20Cot1g-900, which is due to its higher N content and hierarchical pore structure, which is benefit for the efficient use of the charge surface. **Figure 5-4 (d)** shows the comparison of specific capacitance for the samples carbonized at different temperatures for samples Mg8K4Ur20Cot1g-800/900/1000. The values of specific capacitance decrease with the increase of carbonization temperature. This is mainly due to the increased pseudo-capacitance for the sample with higher N content which is carbonized at a lower temperature.

The long cycling test of the samples was conducted under 2 A g<sup>-1</sup> up to 10,000 cycles, as shown in **Figure 5-5**. Generally, all samples can present good stability upon cycling with capacity retention efficiency of larger than 89% after 10,000 cycles. Although sample Mg8K4Ur20Cot1g-800 can present relatively higher capacitances in the initial cycles due to the higher heteroatom doping amount as compared with those carbonized at a higher temperature, the capacitance of Mg8K4Ur20Cot1g-800 decreases quickly in the initial cycles and stabilizes after around 1000 cycles. A large amount of heteroatom doping for the sample carbonized at a lower temperature makes the increase of pseudo-capacitance, however, the low graphitization degree and structure instability induce a quicker capacity decrease upon cycling. Based on the above discussion with both rate capability and cycling stability, we may conclude that Mg8K4Ur20Cot1g-900 are the best samples with optimal performance. After 10,000 cycles at 2 A g<sup>-1</sup>, high capacitances of around 225 F g<sup>-1</sup> can be remained. The good capacitive performance of the heteroatom-doped hierarchical porous carbon obtained in this study is also among the recently reported carbon materials for supercapacitors.<sup>1-10</sup>

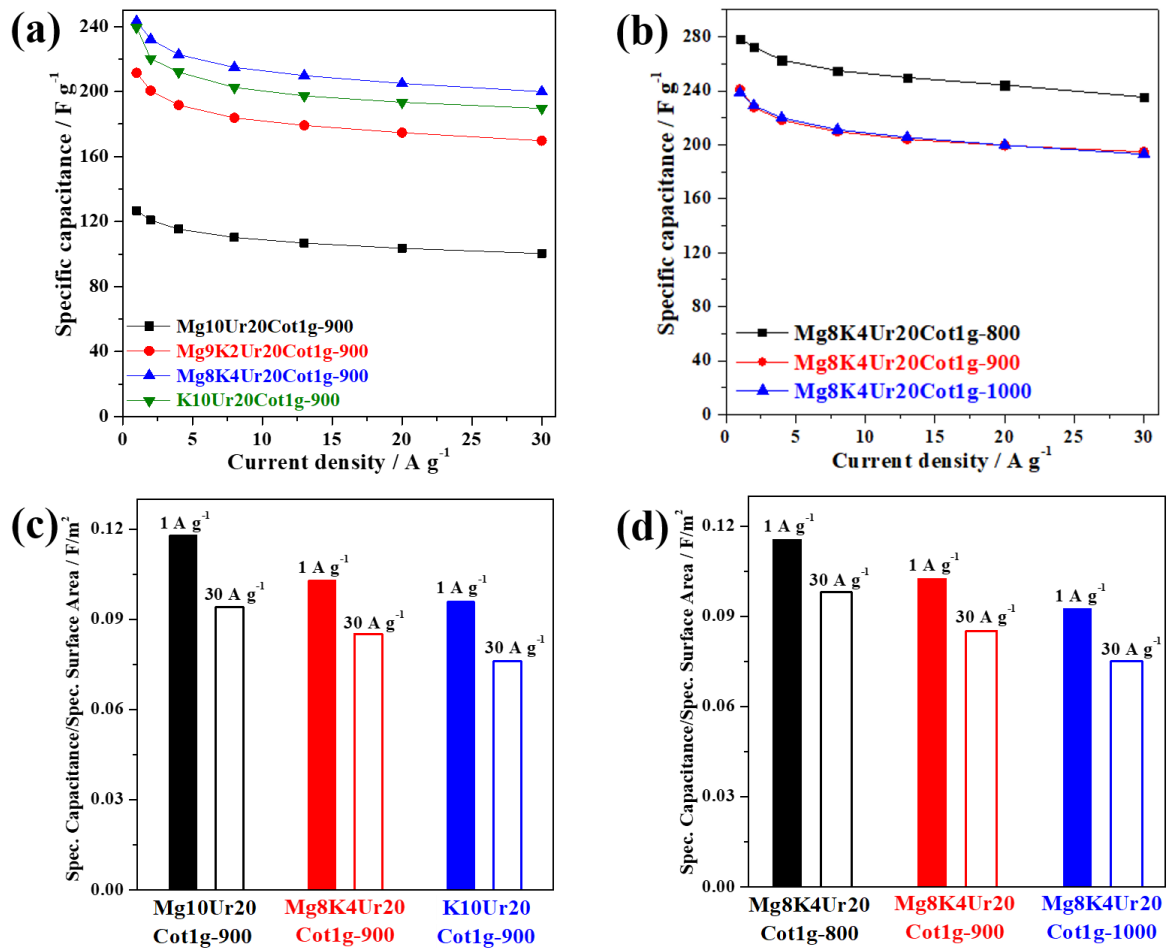


Figure 5-4. Two-electrode test of the supercapacitors in 6 M KOH. (a, b) Specific capacitance at various current density. (c, d) Specific capacitance per surface area based as total specific surface area obtained from t-plot method) for the typical samples.

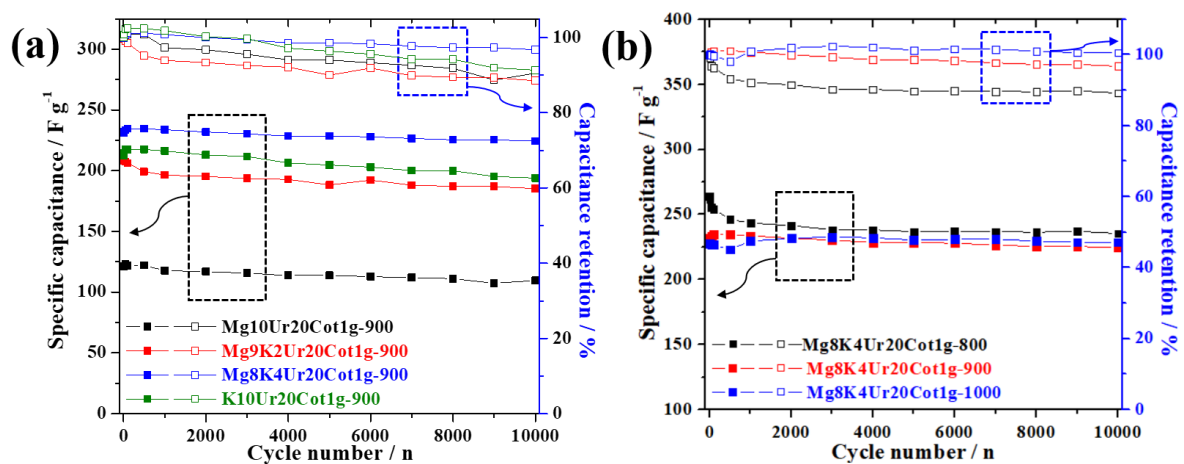
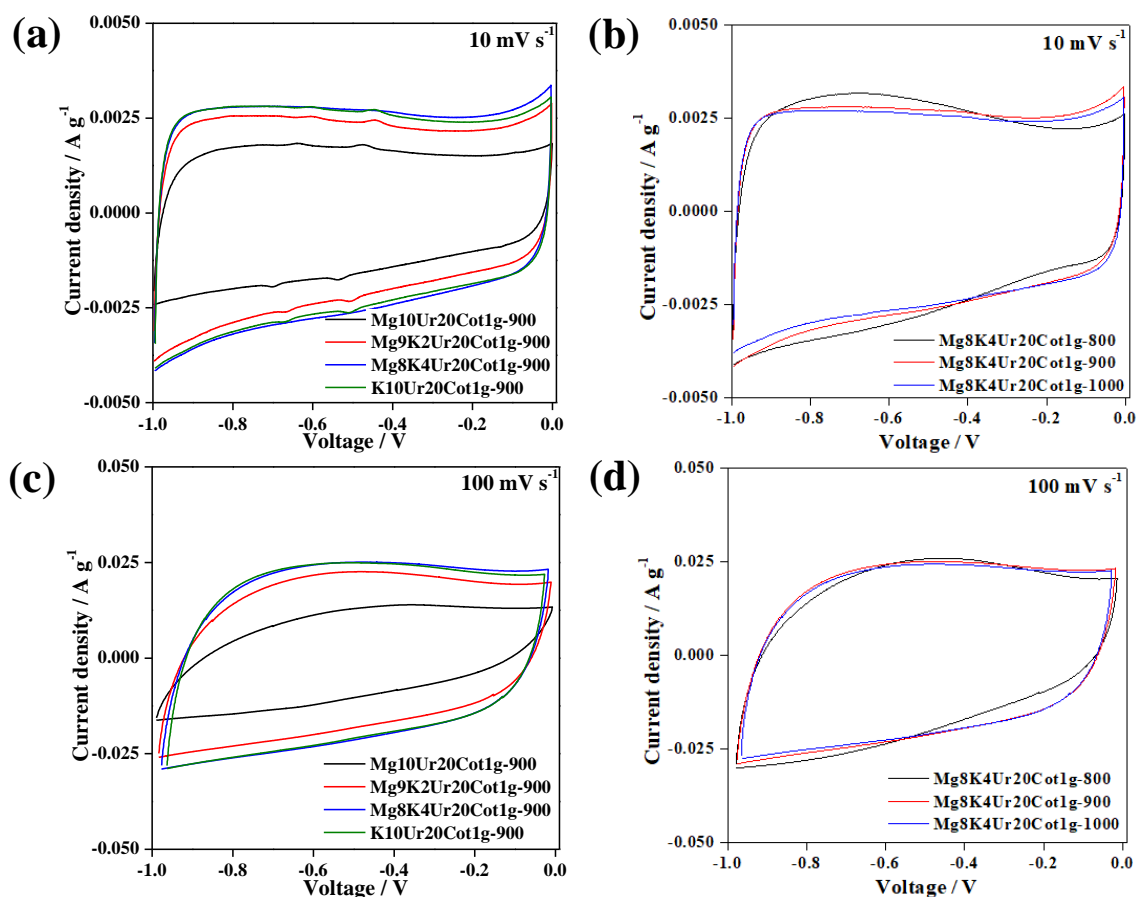


Figure 5-5. Long cycle stability in 10000 cycles at a current density of 2 A g<sup>-1</sup> using two-electrode supercapacitors in 6 M KOH. (a) the samples with typical different pore size distribution; (b) the Mg8K4Ur20Cot1g with different carbonization temperature.

### 5-3-4. Three-electrode system test

Three-electrode measurements, including galvanostatic charge/discharge and CV experiments, were also conducted to further confirm the electrochemical performance. The results are summarized in **Figure 5-6**, **Figure 5-7** and **Figure 5-8**. The same tendency and conclusions can be obtained with the two-electrode measurement results. Generally, the gravimetric capacitances obtained from three-electrode tests are higher than those calculated from two-electrode measurement, which is normally found in three-electrode measurement due to the possible additional pseudo-capacitances.<sup>11</sup>

The capacitance contribution of pure nickel foam in alkaline solution especially for pseudo-capacitor tests is usually considered to be non-negligible.



**Figure 5-6.** Three-electrode test of the carbon samples in 6 M KOH. Cyclic voltammogram curves at scan rate of (a, b) 10 mV s<sup>-1</sup> and (c, d) 100 mV s<sup>-1</sup>.

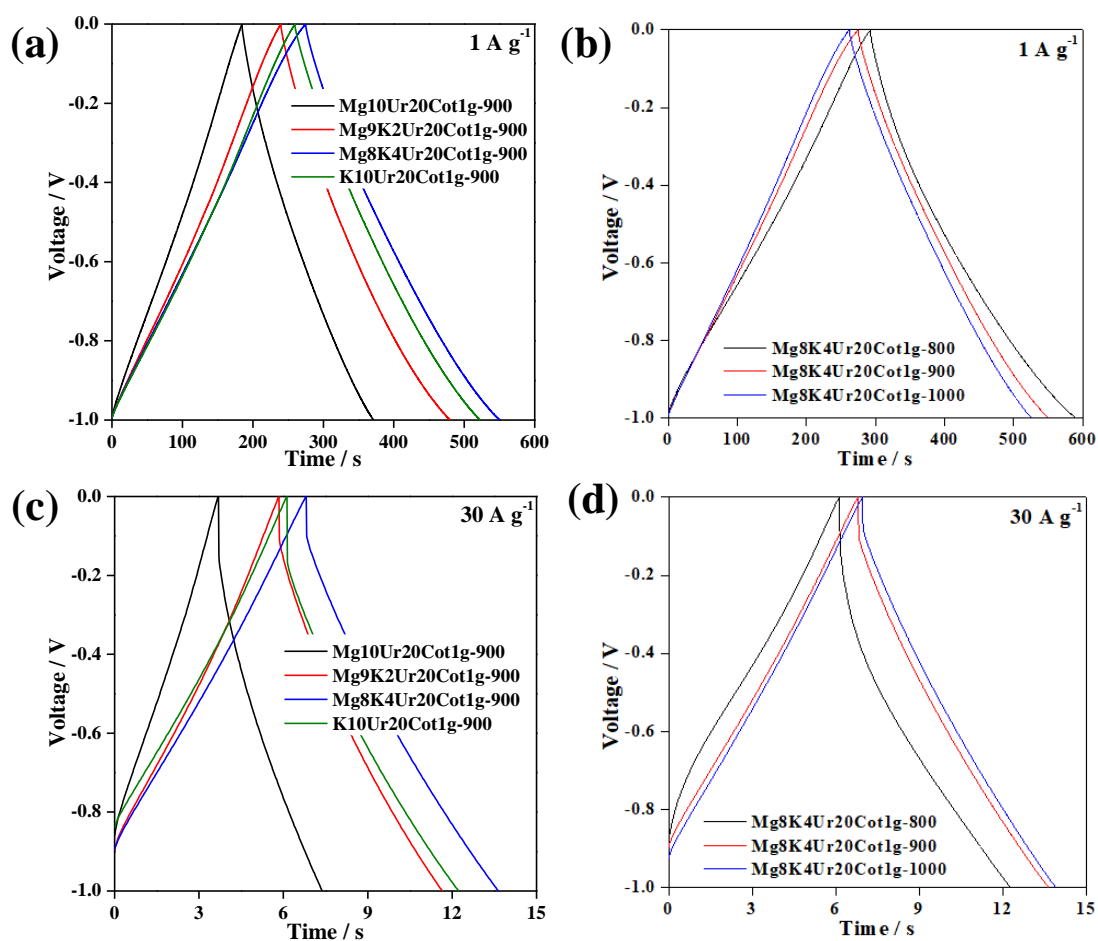


Figure 5-7. Three-electrode test of the carbon samples in 6 M KOH. Galvanostatic charge-discharge curves at current densities of (a, b)  $1 \text{ A g}^{-1}$  and (c, d)  $30 \text{ A g}^{-1}$ .

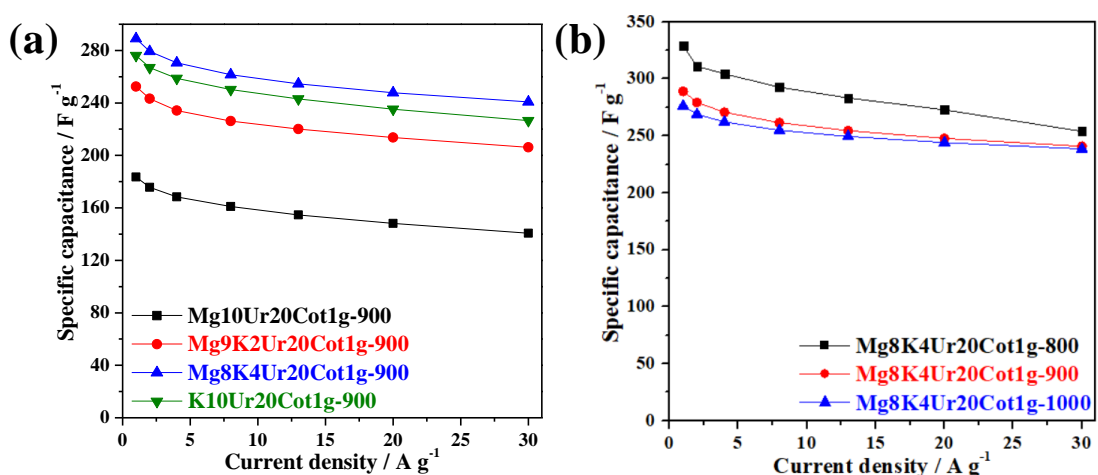


Figure 5-8. Three-electrode test of the supercapacitors in 6 M KOH. Specific capacitance at various current density; (a) The samples with typical different pore size distribution; (b) the samples with different carbonization temperature.

### 5-3-5. EIS measurements by three-electrode system

EIS measurements were also carried out to evaluate the electrochemical behavior of the electrodes. **Figure 5-9** shows the Nyquist plots of the typical samples in three-electrode configuration. Theoretically, the Nyquist plot for a supercapacitor consists of a high-frequency semicircular arc and a low-frequency straight line.<sup>12, 13</sup> The straight lines in the low-frequency region are related to capacitive performance, and the steep lines suggest that the electro-sorption of ions at the interface is not limited by the diffusion process, revealing the excellent behavior of supercapacitors of the prepared carbon samples. The diameters of the semicircles represent the charge transfer resistances ( $R_{ct}$ ).

All plots show small semicircles (with diameters less than 1 ohm), indicating the fast ion transport between the electrodes and the electrolyte. The horizontal axis intercept in the high frequency region of the Nyquist plot is called the equivalent series resistance ( $R_s$ ), which contains the electrolyte resistance, the intrinsic resistance of the active electrode materials, and the contact resistance at the interface between the current collector. The  $R_s$  is at around 0.6 ohm for these electrodes, indicating the good contact and electrolyte conduction of these electrodes. The equivalent circuit is simulated, which is consisted of  $R_s$ ,  $R_{ct}$ , constant phase element (CPE) and Warburg resistance ( $W_s$ ).

The slope of the 45° portion of the curve at intermediate-frequency is  $W_s$ , which is a result of frequency dependence of ion diffusion/transport in the electrolyte to the electrode surface. These values are summarized in **Table 5-1**.

By comparing the plots of K10Ur20Cot1g-900 and Mg8K4Ur20Cot1g-900 in **Figure 5-9** (a), the  $R_{ct}$  for Mg8K4Ur20Cot1g-900 is smaller than K10Ur20Cot1g-900. This is due to the containing of much more open and large pores for sample Mg8K4Ur20Cot1g-900, which is beneficial to a faster ion transport in the hierarchical porous structure. **Figure 5-9** (b) presents the comparison of the Nyquist plots for the samples obtained under different carbonization temperatures. The  $R_s$  and  $W_s$  values are similar, however,  $R_{ct}$  is lower for the samples obtained at higher carbonization temperature (0.63, 0.41 and 0.38  $\Omega$  for samples obtained at 800, 900 and 1000, respectively). indicating the increasing electron and ion conduction for the highly graphited samples obtained at a higher carbonization temperature. Another feature is the straight line at low frequency. Normally, it is well known that  $W_s$  is related to the distributed electronic and ionic conductivity and double-layer capacitance inside the micropores.<sup>14</sup>

**Figure 5-9** (c) shows the Nyquist plots with low frequency region of the Mg8K4Ur20Cot1g samples obtained at different carbonization temperatures. Mg8K4Ur20Cot1g-900 and Mg8K4Ur20Cot1g-1000 show the lower Warburg impedance until 0.25 Hz compared to Mg8K4Ur20Cot1g-800. Moreover, Mg8K4Ur20Cot1g-900 and Mg8K4Ur20Cot1g-1000 increase the angle of the slope at low frequency (0.25 Hz to 0.05 Hz), indicating that the double-layer capacitance

will be increased compared to Mg8K4Ur20Cot1g-800.

**Figure 5-9** (d) shows the bode plots of Mg8K4Ur20Cot1g samples, which can be clearly distinguished by the high, middle and low frequency regions. The phase angle at the low frequency region ( $\sim 1$  Hz) indicates capacitive behavior. It is known that the phase angle towards  $-90^\circ$  attributes the better capacitor behavior.<sup>15</sup> The phase angles of Mg8K4Ur20Cot1g-900 and Mg8K4Ur20Cot1g-1000 are  $-71^\circ$  and  $-70^\circ$ , respectively, which are closer to  $-90^\circ$  than Mg8K4Ur20Cot1g-800 with a value of  $-54^\circ$ .

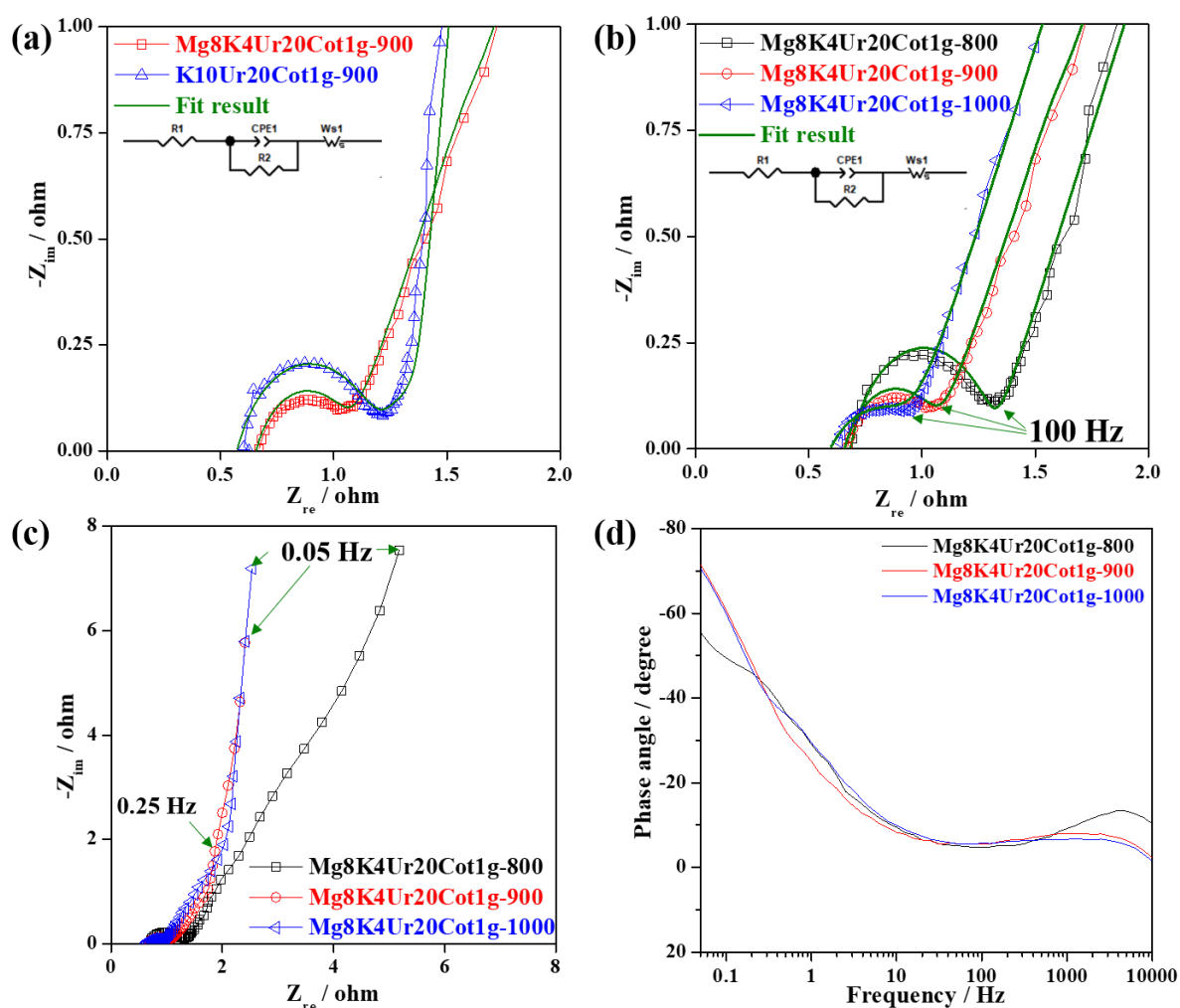


**Figure 5-9.** Typical Nyquist plots (a, b) and Bode plots of the supercapacitors in 6 M KOH after CV measurement. (a) the samples with typical different pore size distribution; (b) the samples with different carbonization temperature; (c) the Mg8K4Ur20Cot1g with different carbonization temperature in low frequency; (d) Bode plots of the Mg8K4Ur20Cot1g with different carbonization temperature.

**Table 5-1. Summarized resistance values.**

| Sample              | $R_s$ ( $\Omega$ ) | $R_{ct}$ ( $\Omega$ ) |
|---------------------|--------------------|-----------------------|
| Mg8K4Ur20Cot1g-800  | 0.684              | 0.626                 |
| Mg8K4Ur20Cot1g-900  | 0.658              | 0.41                  |
| Mg8K4Ur20Cot1g-1000 | 0.593              | 0.38                  |
| K10Ur20Cot1g-900    | 0.572              | 0.59                  |

### 5-3-6. Ragone plots

**Figure 5-10** shows the Ragone plots of the typical symmetric cells, in comparison with the previously reported porous carbons as summarized in **Table 5-2**. The supercapacitor can deliver a high energy density of 38.7 Wh kg<sup>-1</sup> and the power density is up to 45.3 kW kg<sup>-1</sup> based on the active materials, which is among the highest values as compared with the reported porous carbons.

The outstanding supercapacitor performance in terms of high capacitance, good cycling stability and superior rate capacity obtained in this work are ascribed to the very high surface area, heteroatom doping and hierarchical micro-meso-macro-pore structure. The very high SSA of the porous carbon offers a large number of active sites for ion absorption/desorption. The heteroatom doping with N and O elements provides additional pseudo-capacitance to the overall capacitance and enhances the wettability of the electrode materials to facilitate the easy accesses of the electrolyte ions.

The hierarchical pore structure with interconnected micro-meso or even macropores can not only accommodate high accessibility of electrons and ions but also provide a path for the fast ion diffusion into the interior micropores. These characteristics of the porous carbon play cooperative effects on enhancing the electrochemical performance. Importantly, the heteroatom-doped porous carbon with well-developed hierarchical pore structure can be facilely prepared by an efficient exothermic pyrolysis process with subsequent high-temperature carbonization and washing treatment by using the sustainable carbon source of biomass cellulose.

**Table 5-2. Comparison of capacitance and power density of different carbon materials.**

| <b>Ref</b> | <b>Carbon source</b>                    | <b>Sample preparation method</b>  | <b>Specific surface area (m<sup>2</sup> g<sup>-1</sup>)</b> | <b>Specific capacitance (F g<sup>-1</sup>)</b>                            | <b>Maximum Energy density (W h kg<sup>-1</sup>)</b> | <b>Maximum Power density (k W kg<sup>-1</sup>)</b> |
|------------|---|---|---|---|---|--|
| 16         | Graphene                                | Electrochemical exfoliation   | 2100  | 59<br>(in 6M KOH at 5 mV s <sup>-1</sup> )                                | 6.5   | 65   |
| 17         | 1,6-hexanediamine                       | Hydrothermal carbonization + KOH activation   | 1867  | 370<br>(in 6 M KOH at 0.5 A g <sup>-1</sup> )                             | 18.5  | 0.3  |
| 18         | Sodium lignosulfonate                   | Direct pyrolysis  | 1328  | 247<br>(in 7 M KOH at 0.05 A g <sup>-1</sup> )                            | 8.6   | 5.7  |
| 19         | Natural flake graphite                  | Hummer's method (addition of KM <sub>n</sub> O <sub>4</sub> , NaNO <sub>3</sub> , H <sub>2</sub> SO <sub>4</sub> ) + KOH activation | 2252  | 262<br>(in 6 M KOH at 0.5 A g <sup>-1</sup> )                             | 7.4   | 9  |
| 20         | Gelatin                                 | Boric acid template   | 416   | 225<br>(in 6 M KOH at 0.1 A g <sup>-1</sup> )                             | 8   | 6  |
| 21         | Biomass waste, batata leaves and stalks | Thermal treatment + KOH activation  | 3115  | 350<br>(in 6 M KOH at 1 A g <sup>-1</sup> )                               | 6.3   | 10.7   |
| 22         | Bagasse                                 | Hydrothermal carbonization + KOH activation   | 2296  | 320<br>(in 1 M Na <sub>2</sub> SO <sub>4</sub> at 0.5 A g <sup>-1</sup> ) | 6.7   | 10   |
| 23         | Bamboo                                  | K <sub>2</sub> FeO <sub>4</sub> activation  | 1732  | 222<br>(in 6 M KOH at 0.5 A g <sup>-1</sup> )                             | 3.4   | 2.25   |

|           |                          |                                       |      |   |      |      |
|-----------|--------------------------|---------------------------------------|------|---|------|------|
| 24        | Moringa oleifera stems   | Direct pyrolysis                      | 2250 | 283<br>(in 6 M KOH at 0.5A g <sup>-1</sup> )  | 24.5 | 12.9 |
| 25        | Disposable cashmere      | Thermal treatment<br>+ KOH activation | 1358 | 363<br>(in 6 M KOH at 0.5 A g <sup>-1</sup> ) | 25.8 | 12.5 |
| This work | Biomass cellulose cotton | Promoted pyrolysis +<br>Template      | 2400 | 279<br>(in 6 M KOH at 1 A g <sup>-1</sup> )   | 28.7 | 45.3 |

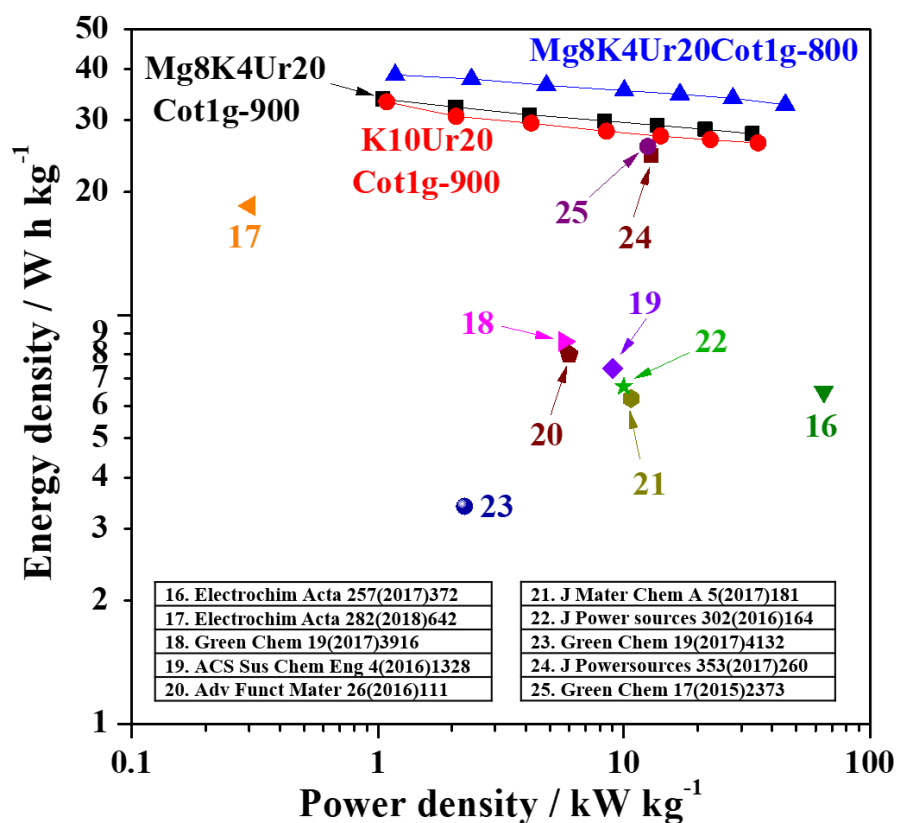


Figure 5-10. The Ragone plots showing energy and power densities of Mg8K4Ur20Cot1g-900, K10Ur20Cot1g-900, and Mg8K4Ur20Cot1g-800 in 6 M KOH electrolytes in comparison with previously reported data.

#### 5-4. Conclusions

The obtained NHPCs presented good capacitive performance as the electrodes in supercapacitors, due to their advantageous characteristics including high surface area, hierarchical pore structure, and

heteroatom doping. In the two-electrode symmetric measurement, the heteroatom-doped hierarchical porous carbons showed high specific capacitance of  $279 \text{ F g}^{-1}$  at  $1 \text{ A g}^{-1}$  in a  $6 \text{ M KOH}$  electrolyte, excellent cycling stability ( $> 89\%$  capacitance retention after 10,000 cycles at  $2 \text{ A g}^{-1}$ ) and good rate capability ( $235 \text{ F g}^{-1}$  at even  $30 \text{ A g}^{-1}$ ). The facile production and outstanding electrochemical performance of the heteroatom doped hierarchical porous carbons reinforced their promising application in supercapacitors, which may also find potential applications in the fields of gas storage, catalysis and pollutant absorbent.

## 5-5. Reference

- [1] I.L. Tsai, J. Cao, L. Le Fevre, B. Wang, R. Todd, R.A.W. Dryfe, A.J. Forsyth, Graphene-enhanced electrodes for scalable supercapacitors, *Electrochim. Acta* 257 (2017) 372-379.
- [2] W. Zhang, C. Yu, L. Chang, W. Zhong, W. Yang, Three-dimensional nitrogen-doped hierarchical porous carbon derived from cross-linked lignin derivatives for high performance supercapacitors, *Electrochim. Acta* 282 (2018) 642-652.
- [3] J. Pang, W. Zhang, J. Zhang, G. Cao, M. Han, Y. Yang, Facile and sustainable synthesis of sodium lignosulfonate derived hierarchical porous carbons for supercapacitors with high volumetric energy densities, *Green Chem.* 19 (2017) 3916-3926.
- [4] H. Fan, W. Shen, Gelatin-Based Microporous Carbon Nanosheets as High-Performance Supercapacitor Electrodes, *ACS Sustainable Chem. Eng.* 4 (2016) 1328-1337.
- [5] Y. Gong, D. Li, C. Luo, Q. Fu, C. Pan, Highly porous graphitic biomass carbon as advanced electrode materials for supercapacitors, *Green Chem.* 19 (2017) 4132-4140.
- [6] Y. Cai, Y. Luo, H. Dong, X. Zhao, Y. Xiao, Y. Liang, H. Hu, Y. Liu, M. Zheng, Hierarchically porous carbon nanosheets derived from *Moringa oleifera* stems as electrode material for high-performance electric double-layer capacitors, *J. Power Sources* 353 (2017) 260-269.
- [7] L. Zhou, H. Cao, S. Zhu, L. Hou, C. Yuan, Hierarchical micro-/mesoporous N- and O-enriched carbon derived from disposable cashmere: a competitive cost-effective material for high-performance electrochemical capacitors, *Green Chem.* 17 (2015) 2373-2382.
- [8] Z. Ling, Z. Wang, M. Zhang, C. Yu, G. Wang, Y. Dong, S. Liu, Y. Wang, J. Qiu, Sustainable Synthesis and Assembly of Biomass-Derived B/N Co-Doped Carbon Nanosheets with Ultrahigh Aspect Ratio for High-Performance Supercapacitors, *Adv. Funct. Mater.* 26 (2016) 111-119.
- [9] X. Wei, Y. Li, S. Gao, Biomass-derived interconnected carbon nanoring electrochemical capacitors with high performance in both strongly acidic and alkaline electrolytes, *J. Mater. Chem. A* 5 (2017) 181-188.
- [10] H. Feng, H. Hu, H. Dong, Y. Xiao, Y. Cai, B. Lei, Y. Liu, M. Zheng, Hierarchical structured carbon derived from bagasse wastes: A simple and efficient synthesis route and its improved electrochemical properties for high-performance supercapacitors, *J. Power Sources* 302 (2016)

164-173.

[11] Z. Liu, Y. Zeng, Q. Tang, A. Hu, K. Xiao, S. Zhang, W. Deng, B. Fan, Y. Zhu, X. Chen, Potassium vapor assisted preparation of highly graphitized hierarchical porous carbon for high rate performance supercapacitors, *J. Power Sources* 361 (2017) 70-79.

[12] S. Zhang, K. Tian, B.-H. Cheng, H. Jiang, Preparation of N-Doped Supercapacitor Materials by Integrated Salt Templating and Silicon Hard Templating by Pyrolysis of Biomass Wastes, *ACS Sustainable Chem. Eng.* 5 (2017) 6682-6691.

[13] Z. Song, L. Li, D. Zhu, L. Miao, H. Duan, Z. Wang, W. Xiong, Y. Lv, M. Liu, L. Gan, Synergistic design of a N, O co-doped honeycomb carbon electrode and an ionogel electrolyte enabling all-solid-state supercapacitors with an ultrahigh energy density, *J. Mater. Chem. A* 7 (2019) 816-826.

[14] A. Di Fabio, A. Giorgi, M. Mastragostino, F. Soavi Carbon-Poly(3-methylthiophene) Hybrid Supercapacitors, *J. Electrochem. Soc.* 148 (2001) A845-A850.

[15] S.K. Jana, B. Saha, B. Satpati, S. Banerjee, Structural and electrochemical analysis of a novel co-electrodeposited  $Mn_2O_3$ -Au nanocomposite thin film, *Dalton Trans.* 44 (2015) 9158-9169.

[16] I. L. Tsai, J. Cao, L. Le Fevre, B. Wang, R. Todd, R. A. W. Dryfe, A. J. Forsyth, Graphene-enhanced electrodes for scalable supercapacitors, *Electrochim. Acta.* 257 (2017) 372-379.

[17] W. Zhang, C. Yu, L. Chang, W. Zhong, W. Yang, Three-dimensional nitrogen-doped hierarchical porous carbon derived from cross-linked lignin derivatives for high performance supercapacitors, *Electrochim. Acta.* 282 (2018)

642-652.

[18] J. Pang, W. Zhang, J. Zhang, G. Cao, M. Han, Y. Yang, Facile and sustainable synthesis of sodium lignosulfonate derived hierarchical porous carbons for supercapacitors with high volumetric energy densities, *Green Chem.* 19 (2017) 3916-3926.

[19] H. Fan, W. Shen, Gelatin-Based Microporous Carbon Nanosheets as High Performance Supercapacitor Electrodes, *ACS Sustain. Chem. Eng.* 4 (2016) 1328-1337.

[20] Z. Ling, Z. Wang, M. Zhang, C. Yu, G. Wang, Y. Dong, S. Liu, Y. Wang, J. Qiu, Sustainable Synthesis and Assembly of Biomass-Derived B/N Co-Doped Carbon Nanosheets with Ultrahigh Aspect Ratio for High-Performance Supercapacitors, *Adv. Funct. Mater.* 26 (2016) 111-119.

[21] X. Wei, Y. Li, S. Gao, Biomass-derived interconnected carbon nanoring electrochemical capacitors with high performance in both strongly acidic and alkaline electrolytes, *J. Mater. Chem. A.* 5 (2017) 181-188.

[22] H. Feng, H. Hu, H. Dong, Y. Xiao, Y. Cai, B. Lei, Y. Liu, M. Zheng, Hierarchical structured carbon derived from bagasse wastes: A simple and efficient synthesis route and its improved electrochemical properties for high-performance supercapacitors, *J. Power Sources.* 302 (2016) 164-173.

[23] Y. Gong, D. Li, C. Luo, Q. Fu, C. Pan, Highly porous graphitic biomass carbon as advanced electrode materials for supercapacitors, *Green Chem.* 19 (2017) 4132-4140.

[24] Y. Cai, Y. Luo, H. Dong, X. Zhao, Y. Xiao, Y. Liang, H. Hu, Y. Liu, M. Zheng, Hierarchically porous carbon nanosheets derived from *Moringa oleifera* stems as electrode material for high-

performance electric double-layer capacitors, *J. Power Sources*. 353 (2017) 260–269.

[25] L. Zhou, H. Cao, S. Zhu, L. Hou, C. Yuan, Hierarchical micro-/mesoporous N- and O-

enriched carbon derived from disposable cashmere: A competitive cost-effective material for high-performance electrochemical capacitors, *Green Chem.* 17 (2015) 2373–2382.

## Chapter 6.

### General conclusion

In this thesis, a facile and efficient strategy to produce NHPCs is introduced for electrochemical ORR and EDLC applications. The production involves a redox exothermic reaction of metal nitrate-carbohydrates using biomass cellulose and urea as raw materials. The incorporation of magnesium nitrate-urea-cellulose or magnesium/potassium nitrate-urea-cellulose endows the doping with nitrogen, exfoliates the cellulose fibers to fine 3D porous powders, and creates a large number of pores at various scales simultaneously. The results obtained in this thesis are summarized as follows.

**In Chapter 1**, the background of various carbon materials and commercial preparation methods of carbon materials for electrochemical energy conversion and storage are briefly described. Then, the importance of N-doped hierarchically porous carbon materials (NHPCs) for electrochemical energy devices and the objective of this thesis are described.

**In Chapter 2**, the NHPCs are prepared by nitrate-induced exothermic reaction and template method. Cellulose fiber is used as carbon source and fuel for the exothermic reaction. Magnesium nitrate are used as an oxidant for the exothermic reaction and the MgO template. Urea is used as N source. Magnesium nitrate and urea are absorbed in the cellulose fibers and upon heating a vigorous exothermic reaction occurred, which exfoliated cellulose fibers with high porous structure. After the exothermic pre-pyrolysis, the precursors are further carbonized at 700-1100°C and washed with an H<sub>2</sub>SO<sub>4</sub> solution to obtain the NHPCs. To optimize the preparation condition, four preparation parameters are comprehensively investigated, including magnesium salt species, carbonization temperature, urea amount, and magnesium salt amount (MgO template amount). (1) The magnesium nitrate introduced the exothermic reaction, which could promote the pyrolysis at a low temperature and quickly exfoliate the cellulose fibers to a highly porous architecture. However, the magnesium acetate-induced reaction was endothermic and the corresponding pyrolyzed samples still had the bulky fiber shape, which was less porous with low specific surface area and pore volume. (2) Although specific surface area is similar with different carbonization temperature, but greatly influencing the N contents, the doping species of N, and the graphitization degree of carbon. (3) The urea is important to offer the N doping source and promote the complete exfoliation of cellulose fibers. However, excess addition of urea would decrease the specific surface area of the NHPCs. (4) MgO template is important for the creation of micro- and mesopores. However, an excess amount of MgO template could decrease the specific surface area of the NHPCs.

**In Chapter 3**, the ORR activities of NHPCs are investigated in 6M KOH electrolyte. The NHPCs obtained from magnesium nitrate precursor show the greatly high ORR activity, being comparable to a

commercial Pt/C catalyst, due to high specific surface area and N doping. The N-free hierarchically porous carbon also exhibits relatively high activity, although the electron transfer number is lower than NHPCs. Thus, N doping has an important role in promoting the electron transfer number, whereas the hierarchical porous structure contributes to enhancing the ORR activity. The NHPCs prepared at 1000°C shows the highest ORR performance, although the N content is lower than those formed at low carbonization temperatures. The increased graphitization degree of carbon at higher temperatures appears also to be an important factor in enhancing the ORR activity. Among the NHPCs prepared in this study, the optimized NHPCs with the highest ORR performance is Mg10Ur20Cot1g-1000, which is comparable to the best reported carbon-based ORR catalysts in alkaline electrolyte, making it a promising substitute for commercial Pt/C.

For obtaining an EDLC electrode with high capacitance, an increased SSA of porous carbon is needed. **In Chapter 4**, the NHPCs with very high SSA of larger than 2700 m<sup>2</sup> g<sup>-1</sup> is produced by controlling the use of magnesium and potassium nitrate in the precursors. The pore size distribution and SSA of the obtained carbons are quite dependent on the magnesium/potassium ratio in the precursors. The addition of potassium nitrate in the raw materials could greatly increase the SSA to larger than 2000 m<sup>2</sup> g<sup>-1</sup>, as compared to the magnesium nitrate added sample with SSA of around 1100 m<sup>2</sup> g<sup>-1</sup>. This is due to the corrosive activation effect of potassium in creating numerous small micro-mesopores (< 4 nm). The addition of magnesium nitrate introduces MgO nanoparticles of several to several tens of nanometers in the carbon matrix, creating numerous meso-macropores (mainly > 4 nm) after removing MgO template; the K-free. Mg10Ur20Cot1g-900 has the continuous and interconnected micro-meso-macro hierarchical pores, but the SSA is the lowest of 1102 m<sup>2</sup> g<sup>-1</sup>. Mg8K4Ur20Cot1g-900 has continuous and interconnected micro-meso-macro hierarchical pores and very high BET SSA of 2600 m<sup>2</sup> g<sup>-1</sup>, whereas Mg-free K10Ur20Cot1g-900 contains mainly, small micro-meso hierarchical nanopores (mainly < 4 nm) and has very high SSA of 2486 m<sup>2</sup> g<sup>-1</sup>.

**In Chapter 5**, the supercapacitor properties of the NHPCs with tunable pore structures are investigated in 6 M KOH electrolyte. The comparison of the above three samples with different pore structure and same carbonization temperature of 900 °C indicated that Mg8K4Ur20Cot1g-900 had the highest specific capacitance and very good cycle stability (after 10,000 cycles at 2 A g<sup>-1</sup>, > 96% capacitance was retained, i.e., ~225 F g<sup>-1</sup>). In addition, the samples Mg8K4Ur20Cot1g prepared under different carbonization temperatures (800, 900 and 1000) were also compared, which had similar SSA but the low temperature carbonized Mg8K4Ur20Cot1g-800 proceeded a high content of nitrogen (4.1 at.%). This sample showed the highest specific capacitance (279 F g<sup>-1</sup> at 1 A g<sup>-1</sup>) due to the nitrogen introduced extra pseudo-capacitance. As compared with previously reported porous carbons, the NHPCs is among the best-reported carbons. The good capacitive performance of the NHPCs obtained in this study is due to their advantageous characteristics including high surface area, hierarchical pore

structure, and heteroatom doping.

Finally, the facile production and outstanding electrochemical performance of the NHPCs could reinforce their promising application in energy storage and conversion devices including metal-air batteries and EDLC.

## Publications

[1] C. Kim, C. Zhu, Y. Aoki, and H. Habazaki, *Electrochim. Acta.* **2019**, 314, 173

Heteroatom-doped porous carbon with tunable pore structure and high specific surface area for high performance supercapacitors

[2] C. Kim, C. Zhu, Y. Aoki, and H. Habazaki, *Ind. Eng. Chem. Res.*, **2019**, 58, 3047

Exothermically efficient exfoliation of biomass cellulose to value-added N-doped hierarchical porous carbon for oxygen reduction electrocatalyst

## Other publications

[1] C. Kim, G. W. Yoo, J. T. Son, *Sci. Adv. Mater.*, **2017**, 9, 771

Synthesis and Electrochemical properties of  $0.5\text{LiFePO}_4\text{-}0.5\text{Li}_2\text{FeSiO}_4$  cathode material for Lithium-ion batteries

[2] C. Zhu, C. Kim, Y. Aoki, and H. Habazaki, *Adv. Mater. Interfaces*, **2017**, 4, 1700583

Nitrogen-doped hierarchical porous carbon architecture incorporated with cobalt nanoparticles and carbon nanotubes as efficient electrocatalyst for oxygen reduction reaction

[3] C. Kim, H. Habazaki, and S. G. Park, *J. Electrochem. Sci. Technol.*, **2016**, 7, 214

Enhancement of Electrolyte Properties for High Energy Density Supercapacitors by using Additive Materials

[4] C. Kim, S. B. Yang, G. W. Yoo, and J. T. Son, *J. Nanosci. Nanotechnol.*, **2016**, 16, 8342

F-Doped  $0.5\text{Li}_2\text{MnO}_3\cdot 0.5\text{LiNi}_{1/3}\text{Co}_{1/3}\text{Mn}_{1/3}\text{O}_2$  High Porous Nanofibers as Cathode Material for Lithium-Ion Battery

[5] C. Kim and S. G. Park, *J. Korean Inst. Surf. Eng.*, **2016**, 49, 357

The Study of Manufacturing the AAO Template and Fabrication of Carbon and Metal Oxide Nanofibers using AAO Template

[6] G. W. Yoo, B. C. Jang, C. Kim and J. T. Son, *Sci. Adv. Mater.*, **2017**, 9, 790

The Effect of Surface Coating on  $\text{LiNi}_{0.6}\text{Co}_{0.1}\text{Mn}_{0.3}\text{O}_2$  Cathode Material for Lithium Secondary Battery by PEDOT-PEG Block Copolymer

[7] S. G. Park, C. Kim and H. Habazaki, *J. Korean Inst. Surf. Eng.*, **2016**, 49, 191

Improved Properties of  $\text{Li}_4\text{Ti}_5\text{O}_{12}$  (LTO) by Surface Modification with Carbon Nanotube (CNT)

## Conference

### 2016

- [1] 金清, J. T. Son, 朴秀吉, 幅崎浩樹, “The effect of surface modification on  $0.5\text{Li}_2\text{MnO}_3\text{-}0.5\text{LiNi}_{1/3}\text{Co}_{1/3}\text{Mn}_{1/3}\text{O}_2$  nanofibers cathode material by conductive polyaniline coating”, ECSJ Spring Meeting 2016, March 29-31, Osaka, Japan
- [2] 金清, 朴秀吉, 幅崎浩樹, 岡田重人, “Enhanced high voltage performance of electrolyte for electrochemical double layer capacitors”, ECSJ Spring Meeting 2016, March 29-31, Osaka, Japan
- [3] C. Kim, S. G. Park, “Synthesized the carbon and metal oxide nanofibers by anodized alumina oxide (AAO) template”, The 3<sup>rd</sup> Korea-Japan Joint Symposium for ARS&ESS, November 25-27, Jeju, Korea

### 2017

- [1] C. Kim, C. Zhu, Y. Aoki, and H. Habazaki, “Preparation of Transition Metal-Nitrogen-Carbon Composites as Bifunctional Electro-Catalysts for Oxygen Reduction and Evolution Reaction”, ECSJ Spring Meeting 2017, March 25-27, Hachioji, Japan
- [2] C. Kim, C. Zhu, Y. Aoki, and H. Habazaki, “Transition Metal-Nitrogen co-doped Porous Carbon for Electrocatalysts”, 第33 回ライラックセミナー ・ 第23 回若手研究者交流会, June 10-11, Otaru, Japan
- [3] C. Kim, C. Zhu, Y. Aoki, and H. Habazaki, “Metallic Co Nanoparticles Embedded in Nitrogen-doped Porous Carbon as Bifunctional Electrocatalysts”, The 5th International Symposium on ALP, November 20-23, Hokkaido University, Sapporo, Japan

### 2018

- [1] C. Kim, C. Zhu, Y. Aoki, and H. Habazaki, “Facile synthesis of N-doped porous carbon as efficient metal-free electrocatalyst for oxygen reduction reaction”, 化学系学協会北海道支部2018年冬季研究発表会, January 6-17, Sapporo, Japan
- [2] C. Kim, C. Zhu, Y. Aoki, and H. Habazaki, “Nitrogen-containing porous carbon electrocatalyst for efficient oxygen reduction reaction”, 22nd Topical Meeting of the International Society of Electrochemistry (ISE), April 15-18, Waseda University, Tokyo, Japan
- [3] 金清, 朱春宇, 青木芳尚, 幅崎浩樹, “Novel exothermic synthesis of N-doped porous carbon as efficient electrocatalyst for oxygen reduction reaction”, 第34回ライラックセミナー・第24回若手研究者交流会, June 16-17, Otaru, Japan
- [4] C. Kim, C. Zhu, Y. Aoki, and H. Habazaki, “Hierarchically porous N-doped carbon for electrocatalysts of Zinc-air batteries”, ECSJ Fall Meeting 2018, September 25-26, Kanazawa University, Kanazawa, Japan

### 2019

- [1] C. Kim, C. Zhu, Y. Aoki, and H. Habazaki, “Hierarchically porous N-doped carbon for electrocatalysts of Zinc-air batteries”, ECSJ Spring Meeting 2019, March 27-29, Kyoto University, Kyoto, Japan

# Acknowledgments

Foremost, I would like to express my sincere gratitude to my supervisors Professor Hiroki Habazaki and Professor Chunyu Zhu for the continuous support of my Ph. D study and research at Hokkaido University, for their patience, motivation, enthusiasm, and immense knowledge. Their guidance helped me in all the time of research and writing of this thesis. I could not have imagined having better advisors and mentors for my Ph. D study.

Besides my advisors, I would like to thank the rest of my thesis committee: Professor Yoshitaka Aoki, Professor Kei Murakoshi, and Professor Shin Mukai, for their encouragement, insightful comments, and hard questions. I am also grateful to Professor Soo-Gil Park and Dr. Ken Ebihara for his constructive criticism and suggestion to improve my research.

This research work could not be completed without a friendly work environment and positive discussion and helping hand of the members of the Laboratory of interfacial electrochemistry. The help of Dr. Damian Kowalski, Ms. Ning Wang, Ms. Laras Fadillah, Mr. Jeong, Mr. Sato, Mr. Takase, Mr. Wada, Mr. Inoue, Ms. Takata, Mr. Yamada, Mr. Kobayashi, Ms. Saito, Mr. Toriumi, Mr. Shen, Mr. Ikeura, Mr. Takano, Mr. Zhu, and Mr. Nishimura, Mrs. Inoue, and Mrs. Iwata.

I am deeply grateful to Graduate school of Chemical Science and Engineering (CSE) and Ministry of Education, Culture, Sports, Science, and Technology (MEXT), Japan for financial support of this research.

Last but not least, I would like to thank my family: my parents for giving birth to me in the first place and supporting me spiritually throughout my life.

Cheong Kim